

<https://doi.org/10.15388/vu.thesis.819>

<https://orcid.org/0009-0001-0121-3310>

VILNIUS UNIVERSITY

CENTER FOR NATURAL SCIENCES AND TECHNOLOGY

Vaida Marčiulionytė

Supercontinuum Generation in Transparent Dielectrics at High Laser Repetition Rates

DOCTORAL DISSERTATION

Natural Sciences

Physics (N 002)

VILNIUS 2025

This dissertation was written between 2021 and 2025 at Vilnius University Laser Research Center. The research was supported by the Research Council of Lithuania.

Academic supervisor:

Prof. Habil. Dr. Audrius Dubietis (Vilnius University, Natural Sciences, Physics, N 002).

Dissertation Defense Panel:

Chairman – Prof. Dr. Mikas Vengris (Vilnius University, Natural Sciences, Physics – N 002)

Members:

Dr. Rokas Danilevičius (Ekspla, Natural Sciences, Physics – N 002),

Dr. Andrejus Michailovas (Center for Physical Sciences and Technology, Natural Sciences, Physics – N 002),

Dr. Audrius Pugžlys (Vienna University of Technology, Austria, Nature Sciences, Physics – N 002),

Dr. Arūnas Varanavičius (Vilnius University, Natural Sciences, Physics – N 002).

The dissertation shall be defended at a public meeting of the Dissertation Defense Panel at 15:00 on 30th of September 2025 in Room 306 at Laser Research Center.

Address: Saulėtekio al. 10, Laser Research Center, Room 306, Vilnius, Lithuania.

Tel. +370 5 236 6005;

The text of this dissertation can be accessed at the library of Vilnius University and on the website of Vilnius University:

www.vu.lt/naujienos/ivykiu-kalendorius

VILNIAUS UNIVERSITETAS
FIZINIŲ IR TECHNOLOGIJOS MOKSLŲ CENTRAS

Vaida Marčiulionytė

Superkontinuumo generacija
skaidriuose dielektrikuose
esant dideliam lazerio
impulsų pasikartojimo dažniui

DAKTARO DISERTACIJA

Gamtos mokslai
Fizika (N 002)

VILNIUS 2025

Disertacija rengta 2021–2025 metais Vilniaus universitete, Lazerinių tyrimų centre. Mokslinius tyrimus rėmė Lietuvos mokslo taryba.

Mokslinis vadovas:

Prof. habil. dr. Audrius Dubietis (Vilniaus universitetas, gamtos mokslai, fizika, N 002).

Gynimo taryba:

Pirmininkas - prof. dr. Mikas Vengris (Vilniaus universitetas, gamtos mokslai, fizika, N 002)

Nariai:

dr. Rokas Danilevičius (Ekspla, gamtos mokslai, fizika – N 002),

dr. Andrejus Michailovas (Fizinių ir technologijos mokslų centras, gamtos mokslai, fizika – N 002),

dr. Audrius Pugžlys (Vienos technologijos universitetas, Austrija, gamtos mokslai, fizika – N 002),

dr. Arūnas Varanavičius (Vilniaus universitetas, gamtos mokslai, fizika – N 002).

Disertacija ginama viešame Gynimo tarybos posėdyje 2025 m. rugsėjo mėn. 30 d. 15:00 Lazerinių tyrimų centro 306 auditorijoje.

Adresas: Saulėtekio al. 10, Lazerinių tyrimų centras, 306 aud., Vilnius, Lietuva.

Tel. +370 5 236 6005;

Disertaciją galima peržiūrėti Vilniaus universiteto bibliotekoje ir VU interneto svetainėje adresu:

www.vu.lt/naujienos/ivykiu-kalendorius

CONTENTS

Acknowledgements	7
List of abbreviations	8
Introduction	10
Approbation	18
1 Physical picture of supercontinuum generation	22
1.1 Fundamental physical effects governing supercontinuum generation	24
1.1.1 Self-focusing	24
1.1.2 Generation and effects of free electron plasma	25
1.1.3 Self-steepening	27
1.1.4 Self-phase modulation	28
1.2 Spatiotemporal scenario of supercontinuum generation	29
1.2.1 ~100 fs pulses	29
1.2.2 Long femtosecond and picosecond pulses	31
1.3 Challenges in high repetition rate femtosecond supercontinuum generation	34
1.4 Supercontinuum spectral width	37
2 Supercontinuum generation in narrow and medium bandgap solid-state materials	40
2.1 Motivation	40
2.2 Materials and experimental details	42
2.3 Filament-induced luminescence	45
2.4 Supercontinuum spectra	48

2.5	Performances at high laser repetition rates, nonlinear losses and bulk heating	53
2.6	Summary and outlook	59
3	Supercontinuum generation at 76 MHz pulse repetition rate	60
3.1	Motivation	60
3.2	Supercontinuum generation with amplified Yb:KGW oscillator pulses	62
3.3	Supercontinuum generation with unamplified Yb:KGW oscillator pulses	68
3.4	Summary and outlook	69
4	All-solid-state post-compression of low-energy pulses at 76 MHz pulse repetition rate	71
4.1	Motivation	71
4.2	Experimental details	73
4.3	Characterization of spectral broadening	75
4.4	Temporal characterization of post-compressed pulses	77
4.5	Evaluation of spatial-spectral homogeneity	81
4.6	Beam quality measurements	82
4.7	Summary and outlook	83
5	Supercontinuum generation with bursts of femtosecond laser pulses	85
5.1	Motivation	85
5.2	Experimental methods and results	86
5.3	Numerical simulations of free electron plasma, STEs and non-linear losses	89
5.4	Numerical simulations of temporal and spectral dynamics . . .	93
5.5	Summary and outlook	98
	Conclusions	102
	Santrauka lietuvių kalba	104
	BIBLIOGRAPHY	117
	Curriculum vitae	131

Acknowledgements

I wish to begin by expressing my sincere gratitude to my supervisor Prof. habil. Dr. A. Dubietis, for his insightful guidance and academic advice, efforts in organizing new scientific equipment for the experiments and for his continuous encouragement throughout the course of this work.

I would also like to thank my co-authors and colleagues, whose support in various forms greatly contributed to the success of this work. Dr. G. Tamošauskas provided significant scientific and technical support for planning, executing experiments, analyzing data, and shared valuable practical insights. Dr. B. Momgaudis and Dr. V. Jukna developed the numerical model and analyzed the data in [A3] and offered expertise on theoretical matters. Doctoral student J. Banys contributed to setting up and performing SHG-FROG measurements, and data analysis in [A2] and [A4], helped design illustrations for experimental setups, and I am especially grateful for his kind support and encouragement, both in work and in life. Dr. R. Grigutis helped with angular spectral measurements and shared template for the Thesis. Student M. Šutovas contributed to setting up the experimental setup in [A4], measurements of spectral dynamics and nonlinear losses, and the corresponding data analysis in [A5]. Doctoral student M. Navickas helped with the experimental automation in [A3]. Dr. J. Vengelis shared valuable practical insights.

I am deeply grateful to my family and friends for their unwavering support and patience. To my dear father, Valentinas: thank you for inspiring my interest in physics.

Vaida Marčiulionytė
June 2025, Vilnius

List of abbreviations

Al ₂ O ₃	Aluminum oxide (sapphire)
AR	Anti-reflection
BaF ₂	Barium Fluoride
BBO	β -barium borate
BGO	Bismuth germanate (Bi ₄ Ge ₃ O ₁₂)
CaF ₂	Calcium fluoride
CARS	Coherent Anti-Stokes Raman Scattering
CCD	Charge-Coupled Device
CMOS	Complementary Metal Oxide Semiconductor
FROG	Frequency-Resolved Optical Gating
FWHM	Full Width at Half Maximum
GDD	Group Delay Dispersion
GGG	Gadolinium Gallium Garnet (Gd ₃ Ga ₅ O ₁₂)
GTI	Gires–Tournois Interferometric
GVD	Group Velocity Dispersion
IR	Infrared
KGW	Potassium Gadolinium Tungstate (KGd(WO ₄) ₂)
LiF	Lithium Fluoride
LSO	Lutetium Oxyorthosilicate (Lu ₂ SiO ₅)
LT	Lithium Tantalate (LiTaO ₃)
LYSO	Lutetium Yttrium Oxyorthosilicate (LuYSiO ₄)
MPA	MultiPhoton Absorption
NA	Numerical Aperture
NIR	Near-Infrared
OPA	Optical Parametric Amplification
OPCPA	Optical Parametric Chirped-pulse Amplification

PCF	Photonic Crystal Fiber
PCMA	Pre-Chirp Managed Amplification
SC	Supercontinuum
SHG	Second-Harmonic Generation
SPM	Self-phase modulation
STE	Self-Trapped Exciton
SWIR	Short-Wave Infrared
TL	Transform-Limited
UV	Ultraviolet
VIS	Visible
YAG	Yttrium Aluminum Garnet ($\text{Y}_3\text{Al}_5\text{O}_{12}$)
Yb	Ytterbium
YSO	Yttrium orthosilicate (Y_2SiO_5)
YVO_4	Yttrium Vanadate
ZnS	Zinc Sulfide

Introduction

Thanks to tremendous progress of ultrafast solid-state laser sources, since its discovery in 1970 [1, 2], supercontinuum (SC) generation in bulk solid-state materials, became a well-established and widely used technique for production of broadband, more than octave-spanning radiation in various parts of the optical spectrum, with spatial and temporal coherence properties equivalent to a white-light laser [3, 4]. SC generation in transparent bulk materials stems from a specific regime of nonlinear propagation, termed femtosecond filamentation [5, 6]. Formation of a light filament, i.e. a very narrow light beam carrying a broadband spectrum, is explained by a dynamic balance between self-focusing due to Kerr effect, diffraction, and defocusing due to free electron plasma created via multiphoton absorption and impact ionization, while its temporal behavior in a normally dispersive medium is governed by the pulse splitting at the nonlinear focus of the beam and subsequent self-steeping of the sub-pulses resulting in an explosive spectral broadening [7, 8].

The attainable spectral extent of SC radiation is of major importance for practical applications, and depends on the driving wavelength and relevant material properties, such as linear and nonlinear indexes of refraction and energy bandgap. These parameters define the critical power for self-focusing (which has to be exceeded for a light filament to form) and clamping intensity of a light filament (which is proportional to the order of multiphoton absorption), and explain the experimental data for a wide range of materials [9, 10], see also [11] for the summary of most recent results. In particular, the experimental results suggest that the blue-shift of the SC spectrum scales with $U_g/\hbar\omega_0$, where U_g stands for the material energy bandgap and $\hbar\omega_0$ denotes the incident photon energy. By contrast, the attainable red-shift of the SC spectrum is not so strictly defined and strongly depends on the focusing condition (the numerical aperture) of the pump beam even in the same nonlinear material. The experiments

backed up with the numerical simulations showed that loose focusing of the pump beam favors spectral broadening toward the long-wavelength side, thus allowing optimization of the red-shifted content of the SC spectrum [12, 13].

The most straightforward and long-standing application of femtosecond SC refers to seeding the ultrafast optical parametric amplifiers (OPAs), where both the blue-shifted and red-shifted portions of the SC spectrum are in use: the visible (blue-shifted) part serves as a seed in second and third laser harmonics-pumped OPAs, while the near and short-wave infrared (red-shifted) part is employed in fundamental harmonic-pumped OPAs [14]. The techniques of femtosecond SC generation in bulk materials were developed to perfection with Ti:sapphire lasers using sapphire and YAG crystals as the most efficient and reliable nonlinear materials for SC generation [12], and recently were transferred to Yb-doped lasers, which despite longer attainable pulse duration, by far outperform Ti:sapphire lasers in terms of pulse repetition rate and average output power. To this end, bulk SC-seeded OPAs pumped by the state-of-the-art ultrafast Yb-doped lasers currently operate at MHz repetition rates and offer wavelength-tunable few optical cycle pulses at various parts of the optical spectrum, ranging from the near ultraviolet to the mid-infrared [15–22]. Optical parametric chirped pulse amplification (OPCPA) at MHz repetition rate with bulk-generated SC as a front-end was also demonstrated [23, 24]. Moreover, supercontinuum generation at MHz pulse repetition rates in bulk materials appears as an appealing alternative to spectral broadening in photonic crystal fibers, finding a wide range of applications in diverse areas of ultrafast science: pulse post-compression down to a few optical cycles [25], time-resolved pump-probe spectroscopy [26], high-speed coherent anti-Stokes Raman scattering (CARS) and imaging [27, 28], and nonlinear microscopy [29], to mention a few.

The diversity of applications calls for improvement and optimization of relevant performance characteristics of bulk-generated SC, such as beam quality [30], polarization properties [31], spatio-temporal and spatio-spectral coherence [32], wavelength stability and timing jitter [33], and carrier envelope phase noise [34]. Over a past decade, extensive studies were carried out in searching for new and efficient nonlinear materials for SC generation with near-infrared pumping, i.e. using fundamental harmonics of Ti:sapphire and Yb-doped lasers [35–44], and more recently, using mid-infrared femtosecond lasers based on novel lasing materials, such as Cr:ZnSe [45, 46]. A significant

effort was dedicated to production of SC with high spectral energy densities within desired wavelength ranges by either modifying pumping condition by employing several beams [47, 48] or by using nonlinear materials with specifically fabricated structure: waveguides embedded in the bulk [38, 49], single crystal fibers [50], liquid jets [51], tailored material composition [52], and polycrystalline ceramics [53, 54].

On the other hand, the emerging device applications demand robust and optical damage-free SC generation performances at high (100s of kHz and higher) pulse repetition rates, provided by state-of-the-art Yb laser systems. In such operating conditions, residual effects due to multiple pulse exposure (e.g. creation of transient defects and heat accumulation) come into play and may cause gradual modification of the optical properties of nonlinear material, leading to its optical degradation, followed by extinction of the SC radiation and eventually, to catastrophic optical damage. However, this topic is still poorly investigated [55, 56] and besides the fundamental interest, poses challenges for what concerns spectral broadening, post-compression and SC generation in bulk materials with regard to intriguing abilities of Yb-lasers to operate in the burst mode with intraburst repetition rates varying from multi MHz to a few GHz, and to amplify femtosecond pulses in rod-type Yb fiber amplifiers at the oscillator repetition rates, see e.g. [57, 58].

The objective of the Thesis

The Thesis is devoted to experimental investigation of high repetition rate supercontinuum generation in bulk narrow and medium bandgap solid-state materials, and aims at identifying the most suitable nonlinear materials that provide low supercontinuum generation threshold, efficient spectral broadening and robust long-term performance with the state-of-the-art high average power ultrafast Yb:KGW lasers.

The main tasks of the Thesis

- Extensive experimental study of filamentation and SC generation (the dynamics of spectral broadening, filament-induced luminescence, nonlinear losses and associated bulk heating) in undoped narrow (KGW, YVO₄, BGO, LT) and medium (GGG, YSO, LSO, LYSO) bandgap dielectric

crystals pumped by amplified Yb:KGW laser pulses with a repetition rate variable up to 2 MHz and comparison of their performances with conventional nonlinear materials: sapphire and YAG under identical operating conditions.

- Investigation of high repetition rate (76 MHz) SC generation in bulk nonlinear materials pumped by sub-100 nJ femtosecond pulses from an Yb:KGW oscillator.
- Post-compression of low-energy (210 nJ), high-repetition-rate (76 MHz) pulses from an amplified Yb:KGW oscillator using sequential spectral broadening in highly nonlinear bulk materials (ZnS, KGW and YAG) and chirp removal with Gires-Tournois interferometric (GTI) mirrors.
- Experimental and numerical investigation of burst-mode filamentation and supercontinuum generation in sapphire crystal, using bursts consisting of two 190 fs, 1030 nm pulses with time delays between adjacent pulses of 16 ns and 400 ps, corresponding to intra-burst repetition rates of 62.5 MHz and 2.5 GHz, respectively.

Scientific novelty

In this work, a number of narrow and medium bandgap materials were investigated and relevant physical phenomena that emerge during high repetition rate femtosecond filamentation and supercontinuum generation in transparent dielectric materials were unveiled:

- It is shown that nonlinear materials with narrow and medium bandgaps have high nonlinearity and, consequently, very low thresholds of filamentation and SC generation, which, in turn, ensures lower absolute energy deposition during filamentation and a decrease in volumetric heating, which partly explains their reliable long-term operation at high pulse repetition rates.
- Generation of stable, octave-spanning low-threshold SC in homogeneous bulk nonlinear material (undoped KGW crystal) pumped directly by 76 MHz Kerr-lens mode-locked Yb:KGW oscillator was demonstrated for the first time.

- It is demonstrated that spectral broadening of femtosecond laser pulses in highly nonlinear bulk materials could be a potentially attractive alternative to fiber-based spectral broadening, offering a virtually alignment-insensitive, low-complexity and low-cost all-solid-state arrangement for post-compression of low-energy (~ 200 nJ) pulses at high laser pulse repetition rates.
- Burst-mode femtosecond SC generation in bulk solid-state material (sapphire) with time delays between adjacent pulses of 16 ns and 400 ps, corresponding to high (62.5 MHz and 2.5 GHz) intra-burst repetition rates was studied for the first time. The measured spectral dynamics of burst-mode filamentation in sapphire demonstrated an increase of SC generation threshold for the second (and every subsequent) pulse in the burst, which further increases with the decrease of pulse separation in time (increase of intra-burst repetition rate), setting a practical limitation to burst-mode SC generation in solid-state materials.

Practical value

This work identified new efficient nonlinear bulk materials and uncovered practical aspects, relevant for optimization of high repetition rate supercontinuum generation and pulse post-compression schemes, which could be readily implemented as front-ends and back-ends, respectively in high average power wavelength-tunable light sources based on optical parametric amplification, as well as used for high speed spectroscopy and imaging:

- Undoped KGW and YVO₄ crystals show stable and durable damage-free performance, negligible bulk heating with pulse repetition rates up to 2 MHz (GGG and BGO up to 200 kHz) and produce more than octave-wide SC spectra with remarkably large spectral red-shifts, which in combination with low filamentation and SC generation thresholds offer very suitable energy trade-off between the seed production and amplification channels for development of high average power ultrafast optical parametric amplifiers operating in the near- and mid-infrared spectral range.

- It is demonstrated that with pumping by relatively long femtosecond pulses (~ 200 fs), the maximum blue-shifted and red-shifted spectral broadenings are achieved with significantly different pump pulse energies, which is relevant for optimization of high repetition rate SC generation schemes.
- High average power, low threshold, stable octave-spanning SC generation in undoped KGW crystal, pumped with a total average power of 6.4 W from a commercial Yb:KGW oscillator with pulse repetition rate of 76 MHz was demonstrated, which could readily serve as an attractive alternative to structured bulk materials and alignment-sensitive SC generation materials with guided wave geometries, offering simplified design for seed generation in high repetition rate and high average power ultrafast light sources based on optical parametric amplification.
- A proof of principle of all-solid-state post-compression for low-energy (210 nJ), high-repetition-rate (76 MHz) pulses from an amplified Yb:KGW oscillator using sequential spectral broadening in ZnS and YAG and the compression of spectrally broadened pulses using Gires-Tournois interferometric (GTI) mirrors is demonstrated.
- The measured spectral dynamics of burst-mode filamentation in sapphire demonstrated an increase of SC generation threshold for the second (and every subsequent) pulse in the burst, which further increases with the increase of intra-burst repetition rate, setting practical limitation to burst-mode supercontinuum generation in solid-state materials.
- The spectral measurements of filament-induced luminescence suggest that scintillating properties of materials could be readily studied using femtosecond near-infrared light source via multiphoton excitation in the filamentation regime, which allows easy separation of excitation and emission wavelengths and low risk of optical damage.

Statements to be defended

- Owing to high nonlinear index of refraction, low filamentation and supercontinuum generation thresholds, and low absolute values of deposited energy via nonlinear absorption, narrow and medium bandgap dielectric

materials are the materials of choice for high repetition rate supercontinuum generation with the state-of-the art ultrafast Yb lasers.

- Undoped KGW crystal is a durable homogeneous bulk nonlinear material for stable octave-spanning SC generation with 76 MHz Yb:KGW oscillator pulses.
- Sequential spectral broadening in highly nonlinear bulk materials produces uniform spectral distribution across the beam profile, offering a simple and alignment-insensitive all-solid-state arrangement for post-compression of low energy (~ 200 nJ) pulses at high laser repetition rates.
- Residual material excitations (free electron plasma and self-trapped excitons) temporarily modify the material properties, altering the nonlinear dynamics and spectral broadening of subsequent pulses in the burst-mode SC generation regime.

Layout of the dissertation

The material presented in this work is organized as follows. Chapter 1 gives an overview of relevant nonlinear phenomena, governing physical effects and relevant scenarios behind femtosecond filamentation and supercontinuum generation in transparent bulk solid-state materials, and briefly introduces challenges related to SC generation schemes at high laser pulse repetition rates. Chapters 2-5 are devoted to presentation of original results. Chapter 2 presents extensive experimental study of filamentation and SC generation (the dynamics of spectral broadening, filament-induced luminescence, nonlinear losses and associated bulk heating) in undoped narrow (KGW, YVO₄, BGO, LT) and medium (GGG, YSO, LSO and LYSO) bandgap dielectric crystals pumped by amplified Yb:KGW laser pulses with a repetition rate variable up to 2 MHz and comparison of their performances with conventional wide bandgap nonlinear materials: sapphire and YAG under identical operating conditions. Chapter 3 presents the results of SC generation and SHG-FROG characterization of SC pulses in bulk nonlinear materials pumped by low energy unamplified and preamplified pulses of 76 MHz Yb:KGW oscillator. Chapter 4 reports on post-compression for low-energy (210 nJ), high-repetition-rate (76 MHz) pulses from an amplified Yb:KGW oscillator using sequential spectral broadening in ZnS and YAG and the compression of spectrally broadened pulses using Gires-Tournois interferometric (GTI) mirrors. Finally, the experimental and numerical investigation of burst-mode filamentation and supercontinuum generation in sapphire crystal, using bursts consisting of two 190 fs, 1030 nm pulses with time delays between adjacent pulses of 16 ns and 400 ps, corresponding to 62.5 MHz and 2.5 GHz intra-burst repetition rates, is presented in Chapter 5.

Contribution of the author

All the experiments described in this Thesis were performed in Vilnius University, Laser Research Center during the period 2021-2025. Most of the experiments and data analysis were carried out by the author of this Thesis. She also prepared the initial manuscripts for [A1], [A2], [A4], and [A5] publications.

Approbation

List of publications on the dissertation topic

- [A1] **V. Marčiulionytė**, K. Reggui, G. Tamošauskas, A. Dubietis, KGW and YVO₄: two excellent nonlinear materials for high repetition rate infrared supercontinuum generation, *Opt. Express* **31**, 20377-20386 (2023).
- [A2] **V. Marčiulionytė**, J. Banys, J. Vengelis, R. Grigutis, G. Tamošauskas, A. Dubietis, Low-threshold supercontinuum generation in a homogeneous bulk material at 76 MHz pulse repetition rate, *Opt. Lett.* **48**, 4609-4612 (2023).
- [A3] B. Momgaudis, **V. Marčiulionytė**, V. Jukna, G. Tamošauskas, M. Barkauskas, A. Dubietis, Supercontinuum generation in bulk solid-state material with bursts of femtosecond laser pulses, *Sci. Rep.* **14**, 7055 (2024).
- [A4] **V. Marčiulionytė**, J. Banys, J. Vengelis, G. Tamošauskas, A. Dubietis, All-Solid-State Post-Compression of Low-Energy Pulses at High Repetition Rate, *Photonics* **11**, 386 (2024).
- [A5] **V. Marčiulionytė**, G. Tamošauskas, M. Šutovas, A. Dubietis, Supercontinuum generation in scintillator crystals, *Sci. Rep.* **15**, 748 (2025).

Other publications

- [B1] E. Trusova, A. Vaitkevičius, Y. Tratsiak, M. Korjik, P. Mengucci, D. Rinaldi, L. Montalto, **V. Marčiulionyte**, G. Tamulaitis, Barium and lithium silicate glass ceramics doped with rare earth ions for white LEDs, *Opt. Mater.* **84**, 459-465, (2018).
- [B2] **V. Marčiulionytė**, V. Jukna, G. Tamošauskas, A. Dubietis, High repetition rate green-pumped supercontinuum generation in calcium fluoride, *Sci. Rep.* **11**, 15019 (2021).

Conference presentations

Presented by the author

- [C1] **V. Marčiulionytė**, J. Banys, J. Vengelis, R. Grigutis, G. Tamošauskas, A. Dubietis, High repetition rate supercontinuum generation in undoped KGW and YVO4 crystals, SPIE Optics + Photonics 2023, August 20-24, 2023, San Diego, USA, **ORAL** presentation.
- [C2] **V. Marčiulionytė**, J. Banys, J. Vengelis, G. Tamošauskas, A. Dubietis, Spectral broadening and post-compression of amplified Yb:KGW oscillator pulses at 76 MHz repetition rate, SPIE Optics + Photonics 2024, August 18-22, 2024, San Diego, USA, **ORAL** presentation.
- [C3] **V. Marčiulionytė**, V. Jukna, G. Tamošauskas, A. Matijošius, S. Butkus, M. Barkauskas, A. Dubietis, Burst-mode filamentation and supercontinuum generation in transparent solids, 14th European Conference on Atoms Molecules and Photons (ECAMP14), June 27-July 1, 2022, Vilnius, Lithuania, **POSTER** presentation.
- [C4] **V. Marčiulionytė**, V. Jukna, G. Tamošauskas, A. Matijošius, S. Butkus, M. Barkauskas, A. Dubietis, Filamentation and supercontinuum generation in solids with burst trains of femtosecond pulses, International Conference on Laser Filamentation (COFIL 2022), Chania, Greece, July 11-15, 2022, **POSTER** presentation.
- [C5] **V. Marčiulionytė**, K. Reggui, G. Tamošauskas, A. Dubietis, Comparative study of high repetition rate supercontinuum generation in undoped

sapphire, YAG and KGW crystals, SPIE Optics + Optoelectronics 2023, April 24-27, 2023, Prague, Czech Republic, **POSTER** presentation.

- [C6] **V. Marčiulionytė**, G. Tamošauskas, M. Šutovas, A. Dubietis, A comparative study of supercontinuum generation in scintillator crystals pumped by near-infrared femtosecond laser pulses, SPIE Optics + Photonics 2024, August 18-22, 2024, San Diego, USA, **POSTER** presentation.
- [C7] **V. Marčiulionytė**, V. Jukna, G. Tamošauskas, A. Dubietis, High repetition rate green-pumped supercontinuum generation and multipulse optical damage in CaF₂ and BaF₂, 44-oji Lietuvos Nacionalinė Fizikos Konferencija (LNFK-44), October 6-8, 2021, Vilnius, Lithuania, **POSTER** presentation.
- [C8] **V. Marčiulionytė**, V. Jukna, G. Tamošauskas, A. Dubietis, Supercontinuum generation with bursts of femtosecond laser pulses, 65th international conference for students of physics and natural sciences (Open Readings 2021, virtual), March 15-18, 2022, **POSTER** presentation (online).

Other presentations

- [D1] **V. Marčiulionytė**, G. Tamošauskas, M. Šutovas, A. Dubietis, J. Banys, A comparative study of supercontinuum generation in undoped scintillator crystals, Advanced Solid State Lasers Conference 2024, October 20-24, 2024, Osaka, Japan. **POSTER** presentation.
- [D2] R. Grigutis, **V. Marčiulionytė**, G. Tamošauskas, N. Garejev, V. Jukna, A. Dubietis, Supercontinuum generation and optical damage in sapphire and YAG at high repetition rates, 25th Congress of the International Commission for Optics (ICO) and 16th International Conference on Optics Within Life Sciences (OWLS), September 5-9, 2022, Dresden, Germany, **ORAL** presentation.
- [D3] K. Reggui, **V. Marčiulionytė**, G. Tamošauskas, A. Dubietis, Supercontinuum generation in KGW crystal at high repetition rate, 66th international conference for students of physics and natural sciences (Open Readings 2023), April 18-21, 2023, Vilnius, Lithuania, **ORAL** presentation.

- [D4] B. Momgaudis, **V. Marčiulionytė**, V. Jukna, G. Tamošauskas, M. Barkauskas, A. Dubietis, Superkontinuumo generacija safyre naudojant femtosekundinių lazerinių impulsų voras, 45-oji Lietuvos Nacionalinė Fizikos Konferencija (LNFK-45), October 25-27, 2023, Vilnius, Lithuania, **ORAL** presentation.
- [D5] M. Šutovas, **V. Marčiulionytė**, J. Banys, J. Vengelis, G. Tamošauskas, A. Dubietis, Spectral broadening and post-compression of femtosecond pulses in ZnS and KGW crystals at 76 MHz repetition rate, 67th international conference for students of physics and natural sciences (Open Readings 2024), April 23-26, 2024, Vilnius, Lithuania, **ORAL** presentation.
- [D6] T. Tamošauskas, **V. Marčiulionytė**, J. Banys, G. Tamošauskas, J. Vengelis, A. Dubietis, Spectral broadening and post-compression of femtosecond Yb:KGW oscillator pulses, 67th international conference for students of physics and natural sciences (Open Readings 2024), April 23-26, 2024, Vilnius, Lithuania, **POSTER** presentation.

Chapter 1

Physical picture of supercontinuum generation

Femtosecond filamentation is a universal phenomenon arising from a specific regime of nonlinear propagation of ultrashort laser pulses in transparent materials. A narrow (in the order of a few micrometers in diameter) light beam is formed, called a light filament, producing an extremely broadband spectrum termed supercontinuum (SC), which emerges from the complex interplay between linear and nonlinear effects. SC generation can be realized in almost any transparent medium and is considered an appealing method for producing broadband radiation. This is primarily due to its excellent spatial and temporal coherence, which enables good beam focusability and pulse compressibility, respectively, as well as its relatively simple practical implementation, particularly in solid-state materials. A general scheme of SC generation requires a lens to focus the ultrashort-pulsed input beam into a sample, in this case a bulk crystal, as illustrated in Fig. 1.1 (a). A photo of a laboratory view of SC generation in YAG crystal is presented in Figure 1.1 (b), which combines image of the crystal with a track of filament-induced luminescence and axial SC as a bright white spot in the center, surrounded by colored conical emission as projected onto the paper screen. Conical emission is a distinctive feature of beam filamentation and SC generation, viewed as off-axis broadband radiation that is emitted at different angles with respect to the beam propagation axis.

In what follows, Chapter 1 provides an overview of the fundamental linear and nonlinear physical effects that govern filamentation and SC generation in condensed media, with pump pulses ranging from femtoseconds to picoseconds.

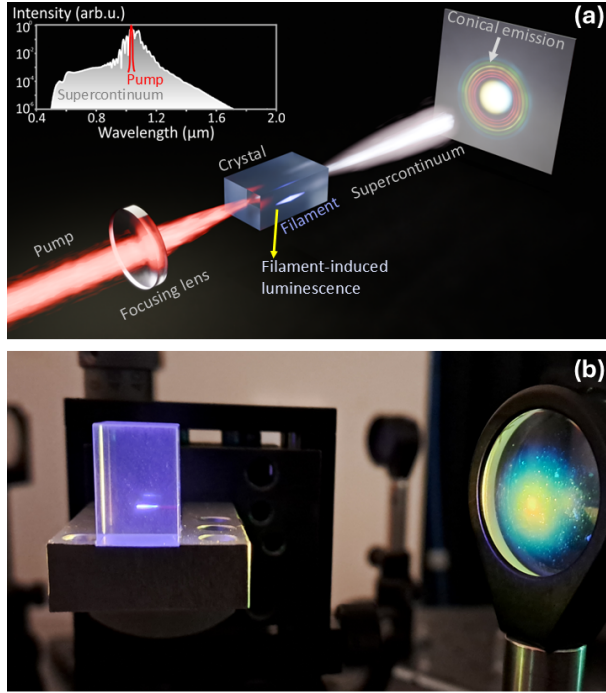


Fig. 1.1 (a) Schematic representation of supercontinuum generation, with the inset illustrating the typical shapes of pump and supercontinuum spectra. (b) Laboratory image of supercontinuum generation in YAG crystal pumped by 1030 nm femtosecond pulses. The laser beam propagates from left to right.

The main physical effects responsible for filamentation and SC generation include self-focusing, free electron plasma generation via multiphoton absorption, self-steepening, self-phase modulation, dispersion, and diffraction. Additional processes, such as four-wave mixing, formation of X-waves, and self-phase modulation in the plasma, play less significant roles in typical SC generation scenarios. While self-focusing and self-phase modulation are well-known phenomena [59], this thesis focuses on their particular aspects that are relevant to nonlinear propagation and filamentation of femtosecond pulses in bulk materials.

1.1 Fundamental physical effects governing supercontinuum generation

1.1.1 Self-focusing

Self-focusing of laser beams is a nonlinear effect that occurs during the initial stage of filamentation. Self-focusing takes place in the spatial domain and manifests as shrinking of the laser beam diameter as it propagates through a transparent material (gas, liquid, or solid). Unlike linear focusing with a lens, self-focusing is a cumulative effect - an increase of the beam intensity further strengthens the self-focusing, thereby reinforcing the process in a runaway manner. This phenomenon results from the optical Kerr effect, which implies the increase of refractive index of the material with increasing intensity. The spatial modulation of intensity of a laser beam induces a proportional local change in the refractive index of a material, expressed as $n = n_0 + n_2 I$. Linear and nonlinear refractive indexes are expressed as $n_0 = \sqrt{\chi^{(1)}}$ and $n_2 = 3\chi^{(3)}/(4\epsilon_0 c n_0^2)$, respectively, where $\chi^{(1)}$ is the linear optical susceptibility, $\chi^{(3)}$ is the third-order nonlinear optical susceptibility, ϵ_0 is the vacuum permittivity and c is the speed of light in a vacuum [4, 5].

Self-focusing initially is overcome by diffraction until the peak power P of the pulse reaches a threshold power, called the critical power for self-focusing P_{cr} , at which self-focusing compensates for beam diffraction and this power is expressed as:

$$P_{\text{cr}} = \frac{0.15\lambda^2}{n_0 n_2}, \quad (1.1)$$

where λ is the laser wavelength. In condensed media, the critical power for self-focusing is typically on the order of a few megawatts, which is easily accessed with modern amplified ultrafast lasers. When the power of input beam exceeds P_{cr} the beam self-focuses at a particular distance z_{sf} along the propagation path at which the beam diameter reaches minimum and its intensity reaches maximum values, called a nonlinear focus. The position of nonlinear focus is expressed by Marburger's law [60]:

$$z_{\text{sf}} = \frac{0.367z_R}{\sqrt{[(P/P_{\text{cr}})^{1/2} - 0.852]^2 - 0.0219}}, \quad (1.2)$$

where $z_R = \pi n_0 w_0^2 / \lambda$ is the Rayleigh length of the incident Gaussian beam of radius w_0 . Equation 1.2 provides a reasonably accurate evaluation of the nonlinear focus position of pulsed laser beams, regardless of pulse duration [5]. Beyond this point, further beam contraction is arrested due to free electron plasma generation and material dispersion.

1.1.2 Generation and effects of free electron plasma

The intensity of a beam undergoing self-focusing increases to a level high enough to initiate nonlinear light-matter interaction, which takes place in the volume of the nonlinear focus. Initially, high-intensity ultrashort laser pulse ionizes the dielectric medium by transitioning valence electrons to conduction band through multiphoton absorption (MPA) [5]. The required number of photons is defined by the order of MPA:

$$K = \langle U_g / \hbar \omega_0 \rangle + 1, \quad (1.3)$$

where U_g is the material bandgap, and $\hbar \omega_0$ is the photon energy and brackets denote the integer part of the ratio. The density of free electrons ρ is defined by the rate equation:

$$\frac{\partial \rho}{\partial t} = \frac{\beta_K}{K \hbar \omega_0} I^K, \quad (1.4)$$

where β_K is the MPA coefficient of the material. Since the MPA is a highly nonlinear process, the resulting free electron plasma density is largest at the beam center, where the intensity is highest, and decreases toward the periphery.

In such a way, the incident laser beam experiences nonlinear energy losses (a decrease in transmittance) due to free electron plasma generation via MPA and free electron absorption processes, both of which are strongly dependent on laser intensity. Nonlinear absorption acts on the most intense part of the pulsed beam in the spatiotemporal domain, where a certain fraction of the input pulse energy is expended to ionize the material. MPA depletes the laser beam by flattening the intensity profile [61] and is followed by the inverse Bremsstrahlung effect - free electron absorption, where electrons in the conduction band generated through MPA are further accelerated by the intense laser field (Fig. 1.2) [5]. As a result, these free electrons acquire sufficient kinetic energy to initiate impact ionization, producing additional free electrons. Eventually, avalanche ionization

can occur, leading to the formation of avalanche-induced free electron plasma and a further increase in the plasma density within the nonlinear focus. The density of free electron plasma increases rapidly due to repeated free electron absorption and material excitation processes, which should be given particular attention when considering longer femtosecond and picosecond laser pulses [4].

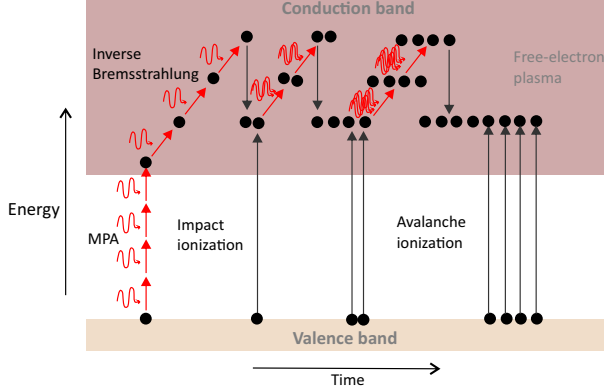


Fig. 1.2 Simplified scenario of nonlinear material excitation begins with MPA and further energy increase of conduction electrons via inverse Bremsstrahlung, followed by impact ionization and avalanche ionization (redesigned from [62]).

Furthermore, the free electron plasma modifies the permittivity of the medium, locally inducing a negative contribution to the refractive index, equivalent to a nonlinear term with $n_2 < 0$ in the center of the beam:

$$n = n_0 - \frac{\rho}{2n_0\rho_c}, \quad (1.5)$$

where $\rho_c = \epsilon_0 m_e \omega_0 / e^2$ is the critical plasma density above which the free electron plasma no longer transmits laser radiation and becomes opaque, where m_e and e are the electron mass and charge, respectively.

This free electron plasma induces defocusing effect, which counteracts self-focusing and effectively prevents further collapse of the laser beam within the material. On top of that, intensity clamping effect takes place in the vicinity of the nonlinear focus where both absorption and defocusing of the beam due to the generation of free electron plasma limit the maximum achievable beam intensity. This clamping level is mainly defined by the intrinsic properties of the material, particularly by the order of MPA:

$$I_{cl} = \left(\frac{2n_0 n_2 \rho_c K \hbar \omega_0}{\beta_k t_p} \right)^{1/(K-1)}, \quad (1.6)$$

where t_p is the top-hat pulse duration. In solid-state media, the peak intensity is clamped to a certain value, which is in the order of several tens of TW/cm² [63].

1.1.3 Self-steepening

Self-steepening of the pulse is the nonlinear effect that occurs in the time domain alongside self-focusing at the onset of filamentation [64]. The pulse propagation velocity is related to the refractive index and group index $n^{(g)} = n_0^{(g)} + n_2^{(g)}$, which in turn depends on the intensity level. As the pulse propagates through a Kerr medium, its central portion, characterized by higher intensity, experiences an increased refractive index and group index. Consequently, it propagates more slowly than the leading and trailing edges of the pulse, which have lower intensity and thus experience lower refractive and group indices. This increase in velocity moving away from the center of the pulse results in the deformation of the on-axis temporal intensity profile with pronounced intensity gradients: long flat rise of the front part of the pulse, steepening of the trailing edge of the pulse (back of the pulse catches up with the center) and overall shorter pulse duration compared to the input pulse (Fig. 1.3). Finally, the most intense part of the pulse shifts from the center toward the back of the pulse.

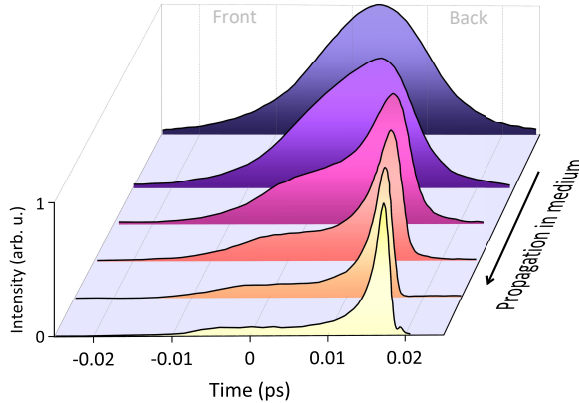


Fig. 1.3 Numerically simulated temporal dynamics of a laser pulse propagating in a medium with normal dispersion due to self-steepening (redesigned from [64]). The arrow indicates the propagation direction of the laser beam.

1.1.4 Self-phase modulation

In addition to the effects discussed above, ultrashort pulses propagating in a transparent medium also undergo self-induced spectral broadening due to the optical Kerr effect in the time domain, called the self-phase modulation (SPM) [4]. The temporal modulation of pulse intensity induces a time-dependent change of the refractive index $\Delta n(t) = n_2 I(t)$. The phase component of the electric field for a pulse propagating along the z -axis is $\phi(t, z) = \omega_0 t - k_0 z = \omega_0 t - z\omega_0 n/c$, where ω_0 is the angular carrier frequency, c the speed of light in vacuum. A change in the pulse phase leads to the generation of instantaneous frequency, which is expressed as the time-derivative of the phase term:

$$\omega_{inst}(t, z) = \omega_0 - \frac{\omega_0}{c} n_2 \frac{\partial I(t, z)}{\partial t} z. \quad (1.7)$$

The magnitude of temporal modulation in the pulse intensity drives spectral broadening by defining the maximum new frequency generated. The attained nonlinear phase and frequency shift are determined by the n_2 of the material, peak intensity of the input pulse $I_0 = I(t = 0, z = 0)$, which could be formally expressed via B-integral [65]:

$$B = \frac{\omega_0}{c} \int_0^L n_2(z) I(z) dz = \frac{2\pi}{\lambda} n_2 I_0 L_{\text{eff}}, \quad (1.8)$$

where L_{eff} denotes the effective nonlinear interaction length

$$L_{\text{eff}} = \frac{\omega_0}{L} n_2(z)/n_2 \cdot I(z)/I_0 dz. \quad (1.9)$$

In contrast to self-focusing, there is no power threshold for the onset of SPM.

In the simplified explanation, the input pulse shape is considered to be a symmetrical Gaussian pulse along the propagation path, as illustrated in Fig. 1.4 (a). In such case, SPM generates new frequency components in the output pulse symmetrically: a negative frequency shift ($\omega/\omega_0 < 1$) occurs at the front of the pulse, producing low-frequency components, while a positive frequency shift ($\omega/\omega_0 > 1$) arises at the back of the pulse, resulting in high-frequency components. The resulting output pulse spectrum exhibits a characteristic symmetrical shape.

However, SPM-induced spectral broadening is influenced and enhanced by self-steepening. The asymmetric temporal intensity profile of the input pulse,

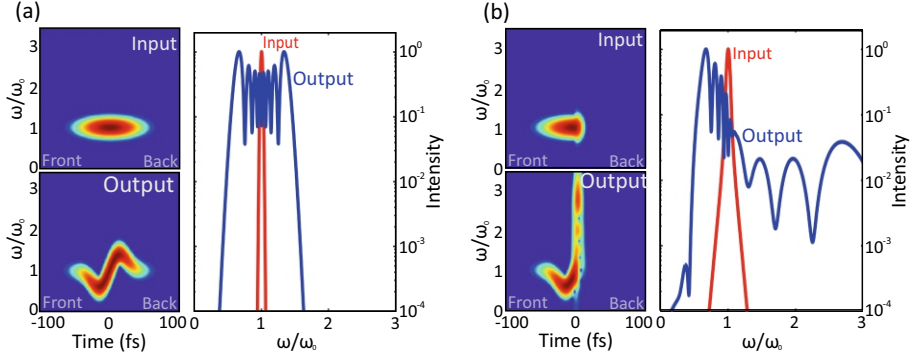


Fig. 1.4 Spectrograms and spectrum of (a) symmetric and (b) asymmetric, self-steepened input pulse and a pulse undergoing self-phase modulation (redesigned from [4]).

exhibiting a flat rise of the leading front and a steep back front of the pulse [Fig. 1.4 (b)], produces asymmetric spectral broadening of different magnitudes. This results in the strong SPM-induced spectrum broadening extending far into the high-frequency side compared to the moderate spectrum broadening toward the lower frequencies.

The output pulse alongside new frequency components generated through SPM contains well-behaved spectral phase and the SPM effect itself does not introduce energy losses. As a result, the spectrally broadened pulse can subsequently be compressed down to transform-limit leading to a substantial increase in peak power, using the simplest single-pass SPM broadening setup [65]. From a practical standpoint, the SPM effect is appealing, as it can be driven by virtually any ultrafast laser system, with or without external focusing of the beam into various solids, liquids, and gases.

1.2 Spatiotemporal scenario of supercontinuum generation

1.2.1 ~ 100 fs pulses

Most in-depth studies on femtosecond filamentation, including both experimental and numerical investigations, have been conducted using Ti:sapphire laser systems emitting pulses with a duration of ~ 100 fs and a carrier wavelength of 800 nm at a repetition rate of 1 kHz. Under these operating conditions, a well-established understanding of the underlying mechanisms of ~ 100 fs

and shorter pulse filamentation dynamics was developed, where typically the pulse undergoes a dramatic spatiotemporal transformation, resulting in extreme broadening of the pulse spectrum (SC generation), which in this work, will be considered as a general scenario that is applicable to most solid-state materials with normal GVD.

First, if the input power is above P_{cr} (Eq. 1.1) the pulse self-focuses at the nonlinear focus z_{sf} (Eq. 1.2). Next, the splitting of the pulse into two sub-pulses with shifted carrier frequencies takes place. This is a purely spatiotemporal effect around the nonlinear focus of the beam in the range of normal GVD that has been proven multiple times numerically and experimentally [66]. The onset of pulse splitting takes place just before the pulse approaches the nonlinear focus and first is driven by the MPA and later by the material GVD. The first sub-pulse (faster leading pulse) has a red-shifted (long-wavelength) carrier frequency, while the second sub-pulse (slower trailing pulse) has a blue-shifted (short-wavelength) carrier frequency. Both sub-pulses propagate away from the center of the pulse in the frame of the input pulse and away from each other due to material GVD [Fig. 1.5 and Fig. 1.6 (a)]. Simultaneously, while the pulse is splitting, a significant portion of pulse energy is displaced off-axis, and the pulse is reshaped into a ring-like structure, which later on rebuilds the axial portion of the pulse, see Fig. 1.5.

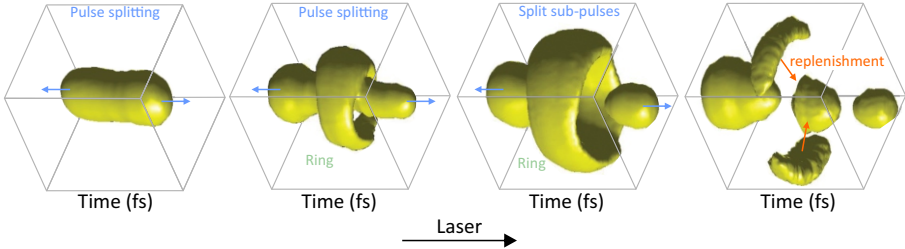


Fig. 1.5 Measured spatiotemporal profiles of a filament vs propagation in water pumped with 100 fs pulses (redesigned from [66]).

The two sub-pulses experience different rates of self-steepening, which defines a broadened spectral shape. The emergent distinctively steep intensity gradient of the trailing front of the second sub-pulse is related to pronounced blue-shifted spectral broadening. Whereas a less steep front of the first sub-pulse emerged, resulting in only moderate spectral red-shift [Fig 1.6 (b)].

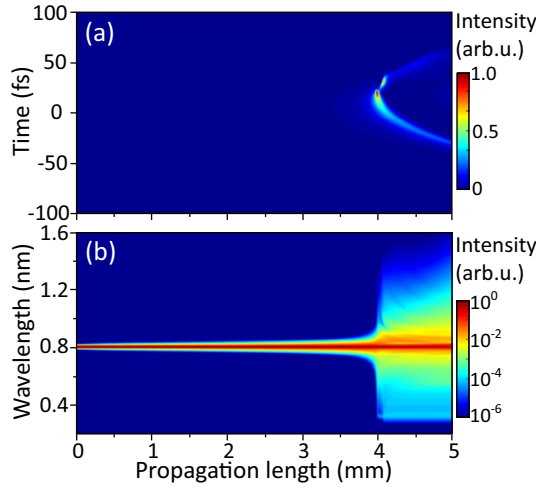


Fig. 1.6 Numerically simulated (a) temporal and corresponding (b) spectral dynamics of 100 fs input pulse propagating in sapphire in normal GVD regime during filamentation and SC generation (redesigned from [3]).

The above description was limited to a single self-focusing event characterised by the smooth SC spectrum and smooth far-field pattern of the SC emission, also accompanied by a gradually decaying filament-induced luminescence track with a single intensity peak attributed to the nonlinear focus [4]. If the power of the replenished pulse is above the P_{cr} , filament refocusing process takes place. Replenished pulse (beyond the first nonlinear focus) propagates through the material, experiences self-focusing, self-steepening and MPA, which results in production of another portion of the SC radiation due to yet another pulse-splitting at the second nonlinear focus, see Fig. 1.7 (a, b). Filament refocusing process is indicated by the periodic modulations visible in the SC spectrum, far-field pattern of conical emission, and secondary peak in the filament-induced luminescence track [4]. However, this SC generation regime should be avoided in practical applications, since the entire SC spectrum develops strong periodic modulation [Fig. 1.7 (b)] due to interference between SC spectra generated by primary and secondary split sub-pulses [Fig. 1.7 (a)].

1.2.2 Long femtosecond and picosecond pulses

The physical picture of SC generation in the range of normal GVD with picosecond pulses is notably different from that with 100 fs and shorter laser pulses. While similar SC spectral shapes can be produced using both femtosecond and

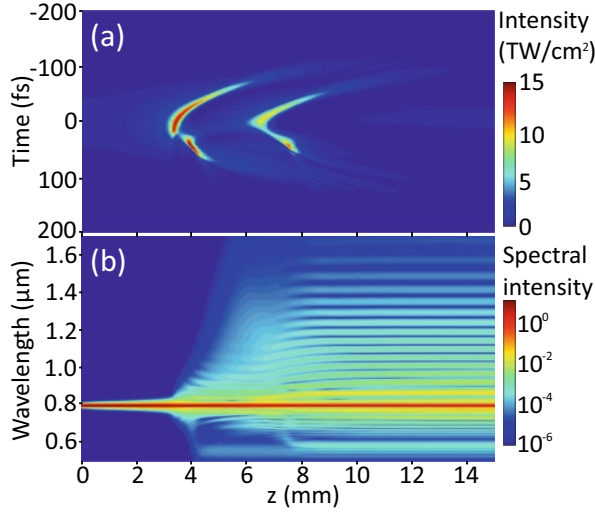


Fig. 1.7 Numerically simulated (a) temporal and corresponding (b) spectral dynamics of filament refocusing in sapphire in normal GVD regime during SC generation (re-designed from [13]).

picosecond pulses, SC generation with sub-picosecond and picosecond pulses is a challenging task due to the increased risk of optical damage, since longer pulses tend to efficiently produce large amounts of free-electron plasma. The leading part of the picosecond pulse initiates free electron generation through MPA, while the trailing part of the pulse significantly contributes to further free electron plasma buildup via the inverse Bremsstrahlung effect, impact ionization, and avalanche ionization (Fig. 1.2). These effects can ultimately result in catastrophic optical damage to the material in the vicinity of the nonlinear focus.

Filamentation and SC generation dynamics of picosecond pulses are strongly influenced by nonlinear absorption and free electron plasma defocusing that are reshaping the input pulsed laser beam (wave packet). At the first nonlinear focus, the trailing part of the pulse is absorbed and the intensity peak shifts toward the front of the pulse. A significant fraction of the rest of the pulse is defocused by the plasma, redirecting energy away from the propagation axis. The displaced energy forms a ring-shaped intensity distribution in the pulse tail [67]. At the first nonlinear focus, the pulse produces only moderate spectral broadening [Fig. 1.8 (c)] with no pulse splitting occurring [Fig. 1.8 (b)], contrary to the short femtosecond pulse case. As the pulse propagates further into the material, the free electron plasma density decreases [Fig. 1.8 (a)]. Previ-

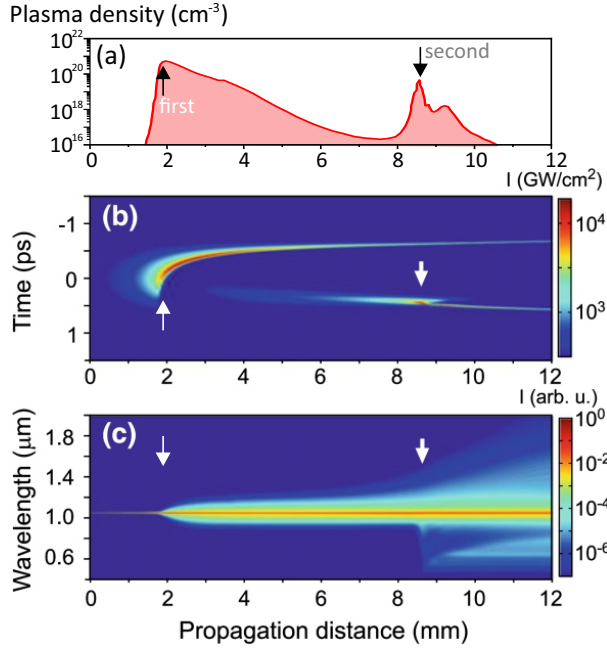


Fig. 1.8 Numerically simulated (a) free electron plasma density (b) temporal and (c) spectral dynamics of 1.3 ps input pulse propagating in a YAG crystal (redesigned from [4]).

ously defocused energy now flows towards the propagation axis and replenishes the axial pulse through a dynamic spatial replenishment [68]. The off-axis portion of the pulse replenishes a shorter on-axis pulse compared to the original input. Self-shortening of the input pulse is characteristic of filamentation of picosecond pulses [67]. This short replenished pulse retains only a fraction of the incident pulse energy, yet sufficient power (higher than P_{cr}) to self-focus at the secondary nonlinear focus. Refocusing of the replenished pulse forms a secondary intensity peak where another round of free electron plasma generation can take place, which was confirmed numerically [67] and indicated as a secondary free electron plasma density peak, as illustrated in Fig. 1.8 (a). Finally, an explosive spectral broadening (SC) is produced at the refocusing position, at the so-called secondary nonlinear focus, where the splitting of the replenished pulse occurs, see Fig. 1.8 (b) and (c).

It should be noted that filamentation and SC generation dynamics of relatively long (from a few hundred fs to sub-picosecond) femtosecond laser pulses in the range of normal GVD exhibit multiple shared features with those of picosecond pulses undergoing filamentation, both being influenced by the

free electron plasma-induced effects, such as plasma absorption and an overall higher free electron density level due to avalanche ionization, including the formation of the first and secondary nonlinear foci as well. This leads to a rather specific case of spatiotemporal pulse reshaping (propagation dynamics in spatial and temporal domains) and spectral broadening dynamics. This includes reshaping of the wave packet due to free electron plasma effects, followed by on-axis pulse replenishment of the on-axis pulse and subsequent splitting of the replenished pulse [63]. However, filamentation dynamics have primarily been investigated at low repetition rates (e.g., 1 kHz), and a significantly different physical behavior can be expected as the laser pulse repetition rate increases.

1.3 Challenges in high repetition rate femtosecond supercontinuum generation

Although the first demonstrations of high repetition rate SC generation date back to the invention of amplified femtosecond Ti:sapphire lasers [69, 70], the interest in SC generation at high pulse repetition rates has been renewed with the advent of Yb-based laser systems producing relatively long-femtosecond pulses centered at around 1 μm with repetition rates of several hundreds kHz to a few MHz.

A number of issues arise related to optical degradation of the material induced by prolonged irradiation by repetitive laser pulses. This effect is enhanced in the filamentation regime. Multipulse optical damage can develop after irradiation by a very large number of successive pulses, whose formation mechanism is different from that of single-pulse damage and has a generally lower threshold, see e.g. [71]. Recent work by Grigutis et.al. demonstrated that conical third harmonic generation can serve as a reliable early indicator of the onset of in-bulk optical damage, such as permanent structural modifications, including nanograting formation, with laser repetition rates up to 200 kHz [55].

The multipulse damage threshold depends on the accumulation of residual effects produced by the previous pulse, a process that is most likely influenced by the pulse repetition rate. Some of the key residual effects include the generation of free electron plasma, self-trapped excitons, formation of various defects, permanent modification of the refractive index, heat accumulation, and material excitations due to stimulated Raman scattering. The formation of point

defects (e.g. F centers) and long-living color centers eventually results in the in-bulk catastrophic multipulse optical damage. A few solutions based on the optimization of SC generation conditions can improve long-term operation in such adverse conditions.

Firstly, to avoid local damage and minimize the impact of irreversible defects, such as long-lived color centers, and to maintain stable SC generation, halide crystals like CaF_2 , BaF_2 and LiF must be continuously translated or rotated with respect to the incident laser beam even at repetition rates as low as ~ 1 kHz [72]. That said, since rotating the CaF_2 plate has been reported to cause depolarization, translating the material is preferred in some cases [73]. The widely used sapphire crystal typically performs well in a static setup when pumped with femtosecond pulses at low 1 kHz repetition rate. Additionally, the sample translation has been successfully applied for SC generation with pump pulses at a 2 MHz repetition rate in a sapphire crystal plate [15, 16]. However, in this work, a stationary SC generation setup is preferred, as it minimizes system complexity and maintenance while potentially avoiding additional spectral fluctuations in the SC introduced by micrometer-scale variations in surface roughness.

Secondly, the pump beam focusing geometry can play an important role in enhancing the durability of damage-free operation of the material. A recent study suggests that loose focusing (numerical aperture NA of 0.004) into an untranslated, relatively long CaF_2 crystal initially results in nearly half the free electron density at the nonlinear focus compared to tight focusing. As a result, the formation and accumulation of long-lived color centers occur on a significantly slower timescale [74].

Moreover, the investigation and testing of new materials with suitable characteristics is essential for achieving robust SC generation at high pulse repetition rates. A particular attention has been paid to laser host materials with high crystalline quality, good thermal properties and high damage thresholds. Another key factor influencing stable operation at high repetition rates is the relaxation time of transient excited states and defects. If the interval between pump pulses is shorter than the relaxation time of these excitations, significant defect accumulation can occur, making stable SC generation impossible.

The topic of thermally-induced effects on filamentation in solid-state materials has received little attention so far, with only a few recent studies conducted in sapphire [56]. Thermal accumulation is related to material properties. Heat is

transferred from a local hot spot, which in this case is the filamentation region, resulting in bulk heating, as illustrated in Fig. 1.9. Duration for heat dissipation processes is related to thermal conductivity and heat diffusion time of the medium [75]. If this time is shorter than the time interval between successive pulses, the thermal load (thermal effect build-up) increases generally through thermal accumulation and can lead to permanent damage of the material.

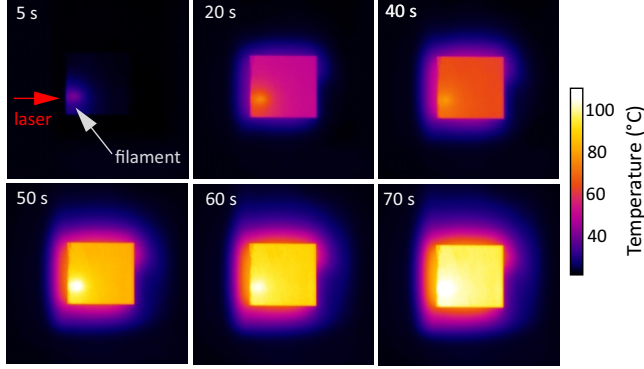


Fig. 1.9 Measured temporal dynamics of the temperature gradient during filamentation in a sapphire crystal pumped with 190 fs pulses at 1030 nm, using an average power of 15 W with burst of 10 pulses (MHz intraburst repetition rate) at 1 MHz repetition rate.

One of thermal-induced phenomena is thermal lensing, where temperature gradient induces refractive index change in the presence of local heat accumulation. Thermal lens can diverge (thermal defocusing) or focus (thermal focusing) the beam, depending on the thermo-optic coefficient. With positive thermo-optic coefficient the refractive index is increased (positive change in refractive index) when higher temperature, which is generally true for transparent solid-state materials, for example, for sapphire and YAG. On the other hand, saturation of thermal defocusing effect (refractive index is reduced with higher temperature) during filamentation at high repetition rates was observed in fluoride glass and ethanol that exhibiting negative thermo-optic coefficients [75].

Studies have been performed in liquids up to 20 kHz repetition rate [75]. However, filamentation in liquids does not cause permanent material modifications, unlike in solids, where it can lead to catastrophic optical damage or even material melting can be expected. Nevertheless, some of the previously mentioned studies on sub-picosecond filamentation in condensed matter reported relevant observations on thermal effects, which may be significant for interpreting femtosecond filamentation and SC generation in solid-state dielectric

crystals at high repetition rates, as this is relevant to the work presented in this thesis.

However, more in-depth experimental studies are needed on filamentation and SC generation dynamics with relatively long femtosecond pulses, especially regarding effects on filamentation over the entire available pulse repetition range, which remains largely unexplored. Simultaneously, the development of more sophisticated numerical models is required to better understand the underlying effects of filamentation in transparent solid-state materials and identify potential practical issues arising from residual material excitations. Alongside standard parameters taken into models based on single-pulse filamentation scenario, it should include the processes with slow build-up and relaxation times, such as local heating, heat diffusion, pressure wave propagation and eventually, formation of point defects, which all become relevant on a long time scale considering irradiation of the material by laser pulses at high repetition rates. In that regard, the lifetimes of transient excitations and carrier dynamics are of utmost importance regarding robust and durable operation of the material in such adverse pumping conditions. However, the essential properties of most relatively new materials operating at high repetition rates are either not well known or are not reported in the literature. Developing numerical models that incorporate a wide range of material characteristics becomes extremely complex and often requires long computation times.

1.4 Supercontinuum spectral width

A key property that determines the usefulness of SC radiation as a broadband light source is the width of its spectrum. There is a limit to the spectral broadening that can be achieved through SC generation in a medium, and the factors governing the short-wavelength cut-off and the long-wavelength cut-off of the SC spectrum differ significantly.

The magnitude of the spectral blue-shift depends on the intrinsic properties of the material, n_2 , bandgap and its dispersive properties, in particular. A well-known universal trend is that the blue-shift of the SC spectrum scales with the ratio of the material bandgap to the incident photon energy $U_g/\hbar\omega_0$, which in turn is related to the value of clamped intensity [9, 10]. For a particular input pulse carrier wavelength, it was demonstrated that in addition to intensity clamping, the chromatic dispersion of the material is the dominant factor in

determining the short-wavelength cut-off of the SC spectrum [76]. This was achieved by introducing a three-wave mixing model and imposing the requirement for fulfillment of the phase-matching condition. Thus, it was revealed that materials with low chromatic dispersion (e.g. halide crystals) exhibit greater blue-shifted SC spectral broadening towards the short-wavelength spectral region. It is also worth noting that the short-wavelength cut-off remains almost consistent regardless of the pumping wavelength.

By contrast, the attainable red-shift of the SC spectrum strongly depends on the focusing condition (the numerical aperture, NA) of the pump beam, and less on the material properties. The experiments backed up with the numerical simulations showed that loose focusing of the pump beam favours spectral broadening toward the long-wavelength side. In this case, a longer filament is produced, thus increasing propagation of the first sub-pulse to achieve a steeper leading front [13]. This allows for partial optimization of the red-shifted portion of the SC spectrum within a given material. The spectral broadening on the long-wavelength side shows an apparently gradual increase with increasing energy of input pulses under fixed focusing conditions. This slower character is attributed to different self-steepening rates of leading and trailing sub-pulses, emerging from the pulse splitting at the nonlinear focus, that are responsible for the red-shifted and blue-shifted spectral broadenings, respectively. In contrast, variations in focusing conditions have a negligible effect on the blue-shifted side of the SC spectrum.

So far, wide bandgap dielectrics have been the most exploited nonlinear materials for SC generation with near-IR pump wavelengths. On the other hand, there is a wide variety of nonlinear materials that have either never been used or have received little attention in the field of nonlinear optics. Given the wide variety of available materials, it is necessary to narrow down the selection to a few promising candidates that are worth investigating for low-threshold and stable SC generation at high laser pulse repetition rates. As a preliminary selection parameter, a high linear refractive index, which is readily available in the literature for a wide range of dielectric and semiconductor materials, see e.g. [77], can serve as an indicator of their promise of large nonlinear refractive index (n_2) either, as illustrated in Fig. 1.10. In that regard, dielectric crystals with energy bandgaps of ~ 6 eV and lower, indicated by bold dots in Fig. 1.10, are of most interest, as they tend to exhibit higher values of n_2 , and thus emerge as strong candidates for low-threshold SC generation. For the sake of clarity, in

what follows, we consider energy bandgaps of 5-6 eV as medium and energy bandgaps smaller than 5 eV as narrow.

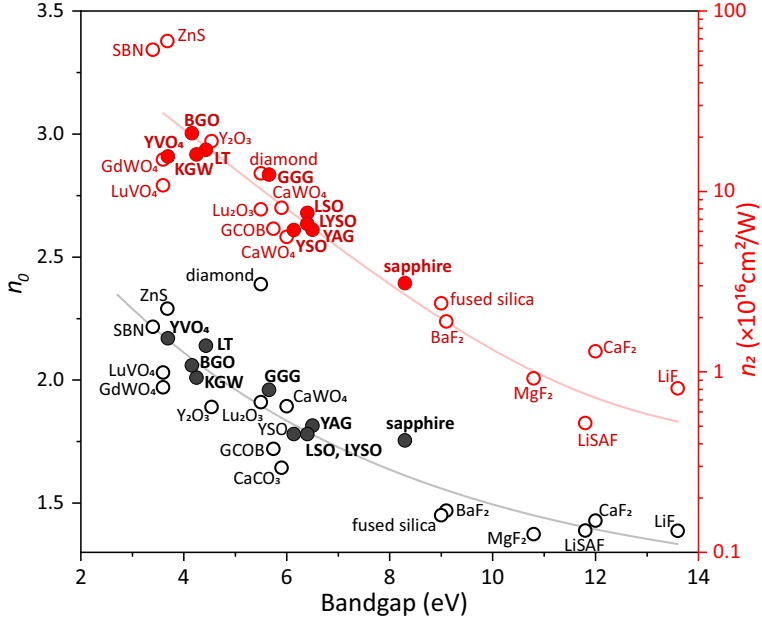


Fig. 1.10 Linear (grey) and nonlinear (red) indexes of refraction versus the energy bandgap U_g for various solid-state materials at 1030 μm . The nonlinear materials investigated in the present study are indicated by bold circles. The solid curves serve as guide to the eye.

Therefore, this Thesis is devoted to experimental investigation of high repetition rate supercontinuum generation in bulk narrow and medium bandgap solid-state materials, and aims at identifying the most suitable nonlinear materials that provide low supercontinuum generation threshold, efficient spectral broadening and robust long-term performance with the state-of-the-art high average power ultrafast Yb:KGW lasers.

Chapter 2

Supercontinuum generation in narrow and medium bandgap solid-state materials

Material related to this chapter was published in [A1] and [A5]

2.1 Motivation

Bulk-generated SC generation serves as an important asset to device applications, such as ultrafast OPAs [14] and OPCPAs [78], and finds a wide range of applications in diverse areas of ultrafast science, including pulse post-compression [79], see also [65] for a review, wave-form synthesis [80], time-resolved spectroscopy [81, 82], CARS [27, 83], and nonlinear microscopy [29]. The advent of ultrafast high repetition rate solid-state lasers based on Yb-doped lasing media prompted the development of SC-seeded OPAs operating at repetition rates from hundreds of kHz to a few MHz, as well as inception of high-speed spectroscopic and imaging systems, offering significant improvement of signal-to-noise ratio and rapid data acquisition [84]. So far, the vast majority of SC generation setups employ sapphire (Al_2O_3) or yttrium aluminium garnet ($\text{Y}_3\text{Al}_5\text{O}_{12}$, YAG) crystals, which are the most reliable nonlinear materials for this purpose [12], exhibiting robust and damage-free performance at high laser pulse repetition rates, even with relatively tightly focused pump beams [55].

However, the energy trade-off between SC generation and pump/excitation cannels becomes very important for MHz repetition rate Yb-laser systems,

which deliver femtosecond pulse with high average power, but relatively low energy per single pulse, therefore calling for search of nonlinear materials with lower SC generation thresholds than conventional materials such as sapphire and YAG currently offer. To this end, narrow and medium bandgap dielectric crystals, owing to their high nonlinear index of refraction and thus low filamentation and SC generation thresholds, emerge as attractive candidates for high repetition rate SC generation with the state-of-the art ultrafast Yb-lasers.

To this end, the most recent results demonstrate that several medium bandgap materials, such as diamond, calcium tungstate (CaWO_4), as well as narrow bandgap materials like potassium gadolinium tungstate ($\text{KGd}(\text{WO}_4)_2$, KGW) and yttrium vanadate (YVO_4), can produce SC spectra with remarkable red shifts, despite only moderate spectral broadenings toward the short-wavelength side. These materials also show potential for optical damage-free performance at 1 MHz pulse repetition rate [43]. Moreover, there is a wide range of other interesting materials, such as narrow bandgap crystals like bismuth germanate ($\text{Bi}_4\text{Ge}_3\text{O}_{12}$, BGO) and lithium tantalate (LiTaO_3 , LT), as well as medium bandgap materials including gadolinium gallium garnet ($\text{Gd}_3\text{Ga}_5\text{O}_{12}$, GGG), yttrium orthosilicate (Y_2SiO_5 , YSO), lutetium oxyorthosilicate (Lu_2SiO_5 , LSO), lutetium yttrium oxyorthosilicate (LuYSiO_4 , LYSO), whose nonlinear optical properties and potential to serve as nonlinear materials for SC generation are poorly explored. BGO, GGG, YSO, LSO and LYSO are primarily identified as efficient scintillators [85] and occasionally serve as laser hosts [86]. LT possesses large second-order nonlinearity and is widely used as efficient nonlinear material for three-wave interactions, such as second harmonic generation and optical parametric amplification. Out of these, to date only GGG, LT [37, 39] and YSO [38] were briefly investigated for SC generation with Ti:sapphire laser pumping, however, none of the above materials were examined with Yb-laser pumping, especially for what concerns their performance at high (tens to hundreds of kHz) pulse repetition rates.

This Chapter presents an extensive experimental study of filamentation and SC generation: the dynamics of spectral broadening, filament-induced luminescence, nonlinear losses and associated bulk heating, in undoped narrow (KGW, YVO_4 , BGO, LT) and medium (GGG, YSO, LSO, LYSO) bandgap dielectric crystals pumped by amplified Yb:KGW laser pulses with a repetition rate variable up to 2 MHz and comparison of their performances with conven-

tional wide bandgap nonlinear materials: sapphire and YAG under identical operating conditions.

2.2 Materials and experimental details

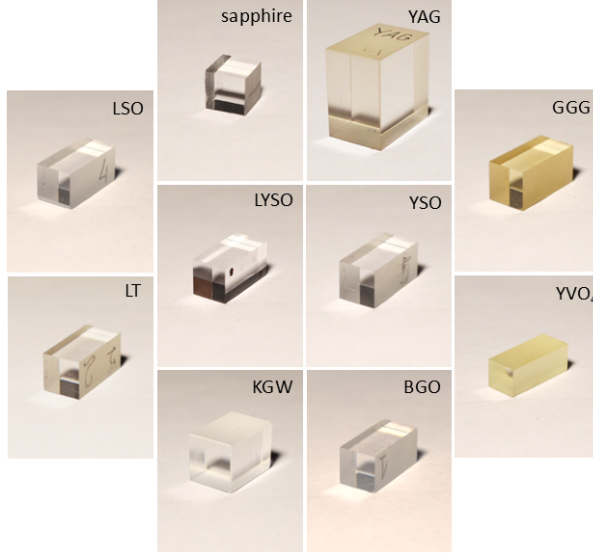


Fig. 2.1 Pictures of all the studied crystals in this work.

The comparative study of SC generation was carried out in uncoated and undoped samples of BGO, GGG, YSO, LSO, LYSO, LT, KGW, YVO₄, YAG, and sapphire, which are illustrated in Fig. 2.1. BGO, GGG, and YAG crystals are of cubic symmetry, so their optical properties are independent of crystal orientation. LT and sapphire were cut along the optical axis (c-cut), while KGW and YVO₄ samples were (b-cut) and (a-cut), respectively. YSO, LYSO, and LSO are biaxial crystals, but their orientation was not provided by the supplier. All crystal samples were provided by EKSMA Optics, with the exception of the YVO₄ crystal, which was supplied by Optogama. All samples had equal lengths of 10 mm, except for the sapphire sample, whose available length was 6 mm. Having identical sample lengths allowed for a straightforward comparison of the SC generation performances. The relevant optical parameters: energy bandgaps, linear and nonlinear indexes of refraction and estimated critical powers for self-focusing of the investigated materials are listed in Table 2.1.

Table 2.1 Relevant optical properties of tested materials: crystal name, chemical formula and abbreviation (Abbr.), U_g is the energy bandgap, n_0 is the linear index of refraction at 1030 nm, as calculated from Sellmeier equations, n_2 is the nonlinear index of refraction, and P_{cr} is the critical power for self-focusing.

Crystal name	Chemical formula, Abbr.	U_g , eV	n_0	n_2 , $10^{-16}\text{cm}^2/\text{W}$	P_{cr} , MW
Sapphire	Al_2O_3	9	1.76 [89]	2.75 [90]	3.25
Yttrium Aluminium Garnet	$\text{Y}_3\text{Al}_5\text{O}_{12}$, YAG	6.5 [91]	1.82 [77]	6.13 [92]	1.42
Lutetium Oxyorthosilicate	Lu_2SiO_5 , LSO	6.4 [93]	1.78 [94]	4.0*, 7.6**	2.24*, 1.18**
Lutetium Yttrium Oxyorthosilicate	LuYSiO_4 , LYSO	6.4 [88]	1.78 [88]	4.0*, 6.6**	2.24*, 1.36**
Yttrium Orthosilicate	Y_2SiO_5 , YSO	6.14 [95]	1.78 [89]	6.1 [96]	1.47
Gadolinium Gallium Garnet	$\text{Gd}_3\text{Ga}_5\text{O}_{12}$, GGG	5.66 [97]	1.96 [98]	12.4 [77]	0.65
Lithium Tantalate	LiTaO_3 , LT	4.43 [37]	2.14 [99]	17 [100]	0.43
Potassium Gadolinium Tungstate	$\text{KGd}(\text{WO}_4)_2$, KGW	4.25 [101]	2.01 [101]	16 [102]	0.49
Bismuth Germanate	$\text{Bi}_4\text{Ge}_3\text{O}_{12}$, BGO	4.16 [103]	2.06 [104]	21*	0.37
Yttrium Vanadate	YVO_4	3.69 [101]	2.17 [101]	15 [101]	0.48

*Calculated using two parabolic band model [87].

**estimated from the experimentally measured threshold energies for SC generation, this work.

The parameters of the BGO, LSO, and LYSO samples were estimated with limited accuracy. Since no experimentally measured n_2 values of LSO and BGO were available, these values were calculated using two parabolic band model [87]. There is no available literature reporting the parameters of the LYSO crystal. Therefore, the parameters were assumed to be equivalent to those of the LSO crystal, as suggested by comparative measurements of optical absorption, radioluminescence, etc., which were reported to be similar in both materials [88].

The simplified experimental setup is depicted in Fig. 2.2. In the first experiment, an amplified Yb:KGW laser (Pharos, Light Conversion Ltd.) was used, providing 180 fs pulses, with a central wavelength of 1030 nm and operating at up to 200 kHz repetition rate. The laser beam with a diameter of 5.14 mm (at the $1/e^2$ intensity level) was loosely focused onto the front face of the sample (S) with a fused silica lens L ($f = +150$ mm), which is equivalent to the numerical aperture (NA) of 0.017. The estimated spot size at the beam focus was 41 μm , with an account of the beam quality factor $M^2 = 1.07$, as specified by the laser manufacturer. This focusing geometry was considered optimal, as

focusing the pump beam inside the sample can slightly reduce the threshold energy for SC generation, but it also increases the risk of multipulse damage due to higher intensity inside the material. In contrast, focusing a diverging pump beam results in a higher SC generation threshold.

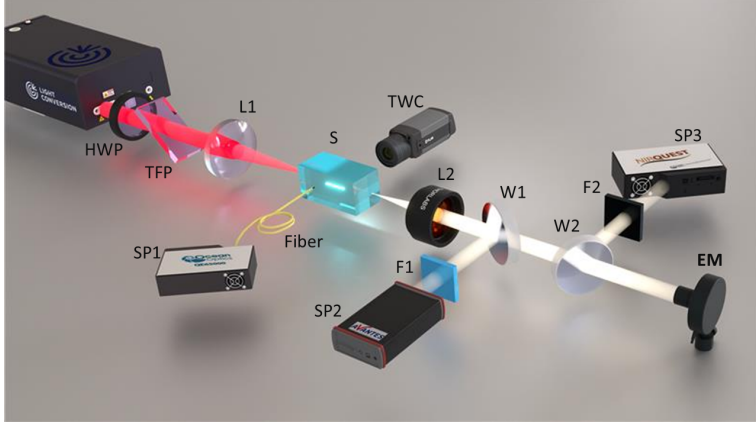


Fig. 2.2 Experimental setup: HWP, half-wave plate; TFP, thin-film polarizer; L1, focusing lens; L2, collimating lens; W1, W2, fused silica wedges; F1, short-pass filter; F2, long-pass filter; SP1 and SP2, ultraviolet-near infrared (UV-NIR) spectrometer; SP3, near infrared-shortwave infrared (NIR-SWIR) spectrometer; EM, energy meter, TVC, thermal vision camera.

For SC generation at MHz pulse repetition rate, an amplified Yb:KGW laser (Carbide, Light Conversion Ltd.) was used, which provided pulses of similar duration (210 fs) with a central wavelength of 1030 nm at pulse repetition rate that could be tuned up to 2 MHz. The laser beam with a diameter of 4.3 mm (at the $1/e^2$ intensity level) was focused onto the front face of the crystal sample (S) with a fused silica lens L1 ($f = +150$ mm), which is equivalent to the NA of 0.014. A rather similar beam spot size of ~ 49 μm was estimated at the focus, accounting for the beam quality factor $M^2 = 1.07$ as provided by the laser manufacturer.

The spectral measurements were performed with three spectrometers. Spectrometer SP1 (Ocean Optics QE65000, the detection range 200 – 900 nm) was used to measure filament-induced crystal luminescence, whose signal was captured from the polished side of the sample. The measurements of SC spectra were performed as follows. The axial portion of the SC radiation was collimated by an achromatic lens L2 ($f = +75$ mm) and, taking the reflections from fused silica wedges W1 and W2, was directed to UV-NIR (AvaSpec-3648, with a

detection range of 200 – 1100 nm, SP2) and NIR-SWIR (NIRQuest-512, with a detection range of 900 – 2100 nm, SP3) spectrometers to measure the short-wavelength and long-wavelength portions of the SC spectrum, respectively. Both spectrometers were operated simultaneously. In order to increase the dynamic range of spectral measurements, the most intense part of the SC radiation around the pump wavelength was attenuated using appropriate calibrated short-pass (F1) and long-pass (F2) filters placed in front of the UV-NIR and NIR-SWIR spectrometers, respectively. The actual spectra were reconstructed by correcting the measured spectra with an account for the filter transmission functions and for the sensitivity functions of the spectrometers at the data post-processing stage.

The spectral dynamics in each sample were measured by fine-tuning the pump pulse energy, using either a computer-controlled attenuator integrated into Pharos laser system, or, in the case of the Carbide laser, an attenuator consisting of a half-wave plate (HWP) and a thin-film polarizer (TFP). For a more detailed study of sample performance, along with spectral measurements, measurements of nonlinear transmission and bulk heating of the tested samples were performed. The sample transmittance as a function of the input pulse energy was measured after the removal of wedges W1 and W2 and using a thermal energy meter (Ophir 3A-PF-12), which was thereafter used to calculate the spectral energy density of the SC radiation. The crystal temperature was monitored with a thermal vision camera (FLIR, A600-Series, TVC), which imaged the side wall of the sample, as illustrated in Fig. 2.2. All measurements were performed with the sample kept in a stationary position. Each sample was placed on a metal holder, except as noted in the bulk heating experiments.

2.3 Filament-induced luminescence

Figure 2.3 presents the views of investigated nonlinear crystals (except LT), and their respective SC emission patterns projected onto the paper screen, while the insets show the filament-induced luminescence spectra in these materials, as captured from polished side with a fiber spectrometer. Most of crystals (except KGW and LT) exhibit remarkably strong filament-induced luminescence, which is easily perceived by the naked eye. In general, in dielectric materials, filament-induced luminescence originates from the relaxation of electrons in the conduction band, which are produced by the multiphoton absorption, and is

associated with the relaxation of various transient excited states, such as self-trapped excitons (STEs), F centers, impurities, as well as with the emissions due to charge transfer and lattice defects [105].

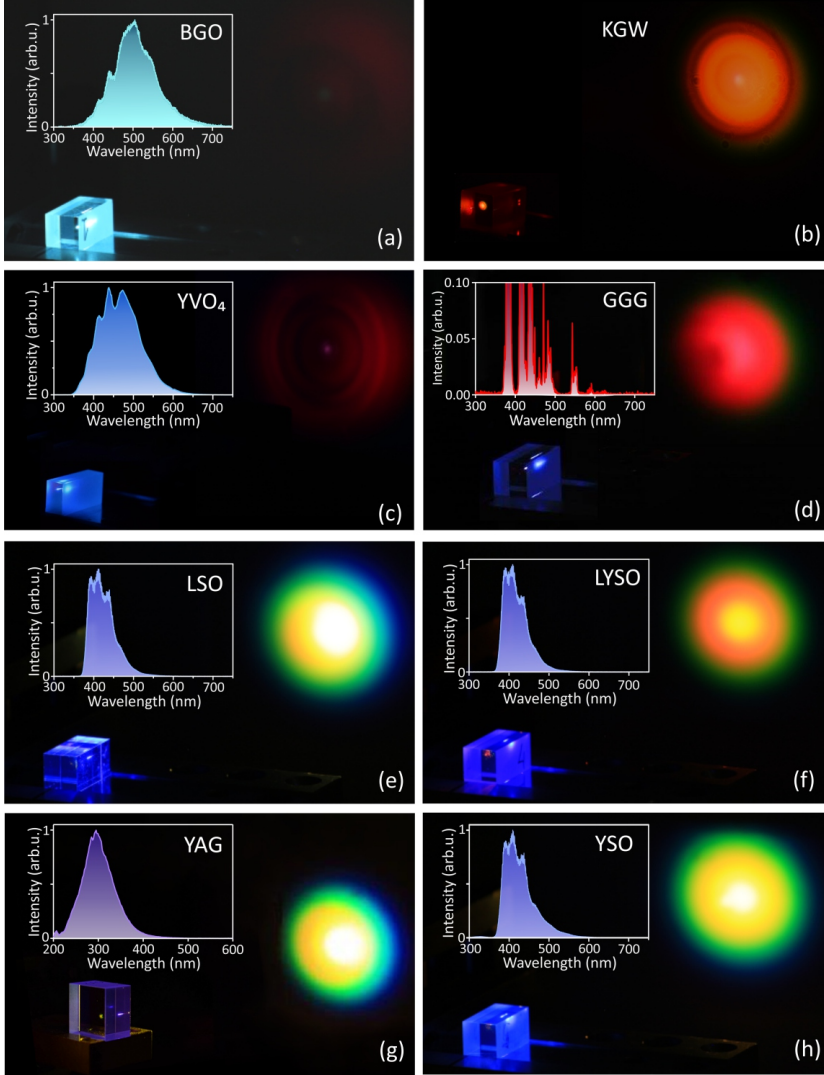


Fig. 2.3 Photos of the SC emission patterns produced in the investigated crystals. Crystal views are seen at the bottom left corner of the images. The insets show spectra of filament-induced luminescence.

BGO crystal produces an exceptionally broadband filament-induced luminescence [Fig. 2.3 (a)], which spans the entire visible range, with the peak intensity at ~ 500 nm, and which is associated with the decay of STEs [106]. Filament-induced luminescence spectra in LYSO, LSO, and YSO are similar

to each other and cover the 360 – 550 nm range, with central peaks located at around 410 nm [Figs. 2.3 (e), (f) and (h)]. GGG also produces strong luminescence in the UV and VIS range [Fig. 2.3 (d)] with the most prominent spectral peaks at 383 nm, 418 nm, 436 nm, and 470 nm. The first two peaks could be associated with luminescence of pure material [107], while the remaining peaks could be attributed to the luminescence of unidentified dopants, although the supplier specified the sample as undoped. The strong UV luminescence of YAG crystal [Fig 2.3 (g)] has a maximum intensity at 300 nm and is attributed to combined STE and antisite defect-related emissions [108]. YVO_4 produces strong broadband emission centered at ~ 450 nm [Fig. 2.3 (c)] that is attributed to transitions within the vanadate (VO_4^{3-}) group [109]. Finally and interestingly no luminescence in the UV, visible and near-IR was observed in KGW and LT (not shown) crystals, at least within the detection range of fiber spectrometer (200 – 900 nm).

Notably, the recorded filament-induced luminescence spectra in the investigated materials are identical to their photoluminescence and radioluminescence spectra, which are produced via direct absorption of high-energy photons in the UV spectral region and by irradiation of the samples with alpha particles, protons, X-rays and gamma rays, respectively, see e.g. [85, 88, 110–113]. These are the main approaches to study scintillating properties of the materials, which however have certain limitations for what concerns the penetration depth and risk to modify or damage a relatively large area of the sample. To this end, filament-induced luminescence could be viewed as experimentally simple and cost-effective method for investigating the luminescence properties, such as spectra and decay times (by performing time-resolved measurements) of undoped as well as doped scintillator crystals. First of all, since the filament-induced luminescence originates from simultaneous absorption of several photons, whose total energy exceeds the bandgap energy of material, it offers easy separation of excitation and emission wavelengths and provides strong signal despite being emitted over the entire solid angle. The position of the filament track inside the crystal can be easily adjusted in a desired way by varying the pump pulse energy, whereas the intensity clamping in a light filament greatly reduces the risk of optical damage. These features can be helpful for obtaining additional information about crystal homogeneity and reveal the presence and distribution of different dopants in the sample.

2.4 Supercontinuum spectra

The screenshots of supercontinua in KGW, LSO, LYSO, YAG and YSO crystals [Figs. 2.3 (b), (e-h)] show bright central spots, surrounded by colored rings (conical emission), whose wavelengths decrease from the center to the periphery and reveal broadband nature of SC radiation in these materials. By contrast, only red axial SC and conical emission is produced in YVO_4 and GGG, while BGO produces only faint deep-red conical emission that could barely be distinguished [Fig. 2.3 (a)].

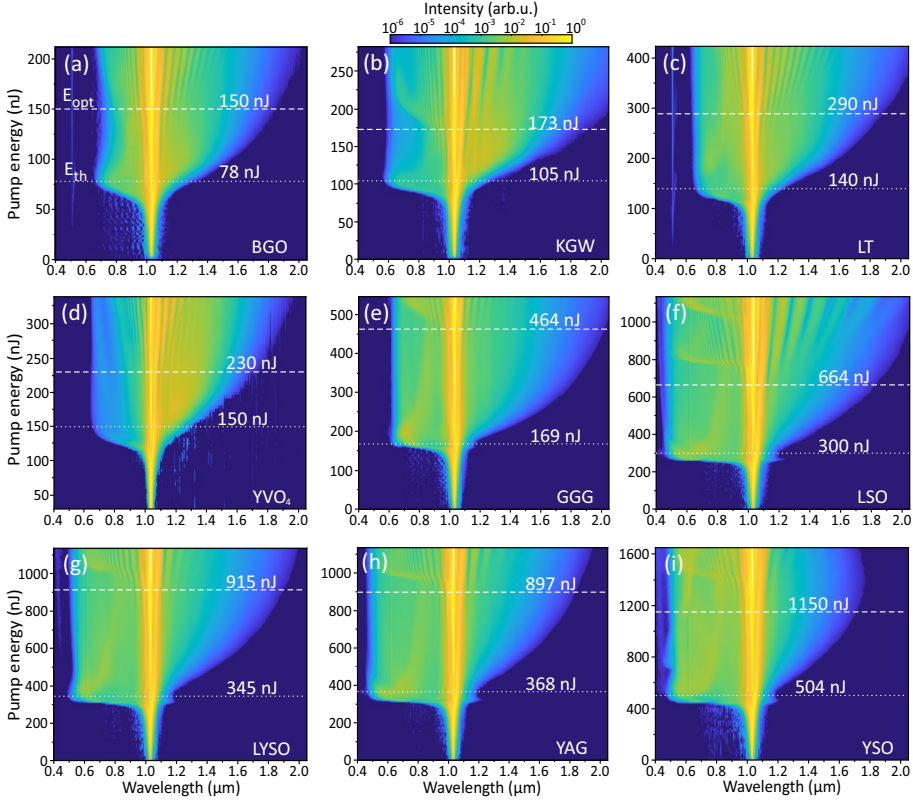


Fig. 2.4 The dynamics of spectral broadening versus the pump pulse energy measured in (a) BGO, (b) KGW, (c) LT, (d) YVO_4 , (e) GGG, (f) LSO, (g) LYSO, (h) YAG and (i) YSO crystals pumped with 180 fs, 1030 nm pulses at 10 kHz repetition rate. White lines mark threshold (dots) and optimal (dash) energies for SC generation.

Figure 2.4 presents the dynamics of spectral broadening in BGO, KGW, LT, YVO_4 , GGG, LSO, LYSO, YAG and YSO crystal samples versus the pump pulse energy. The laser repetition rate was set at 10 kHz, at which no spectral changes were observed in any of these crystals. The measured spectral dynamics

share relevant common features: an explosive blue-shifted spectral broadening occurs after reaching a certain pump pulse energy level, while a much slower red-shifted spectral broadening continues more or less throughout the entire investigated energy range. Additionally, after reaching a certain pump pulse energy distinct periodic modulations appear on both sides of the SC spectrum, well distinguishable on the blue-shifted side of SC spectra in [Figs. 2.4 (b), (e–i)]. A weak (at the 10^{-5} intensity level), but distinctive signal at 515 nm that accompanies SC generation in LT [Fig. 2.4 (c)] is attributed to phase-mismatched second harmonic generation due to second-order nonlinearity of the crystal. The second harmonic signal is also generated in BGO sample [Fig. 2.4 (a)], however, this observation is unexpected, since BGO crystal is optically isotropic due to its cubic lattice symmetry and does not possess any second-order nonlinearity.

The threshold energy for SC generation E_{th} was defined as the pump pulse energy, where the blue-shifted spectral broadening quickly settles to a certain cut-off wavelength that remains almost constant even with further increase of the pump pulse energy. The optimum energy E_{opt} , was defined as the pump pulse energy, which produces the largest red-shifted spectral broadening before the onset of periodic modulation in the SC spectrum due to filament refocusing. Both energies are marked by the dashed lines and their values are labeled in the plots. To overview, the experimentally evaluated threshold energy for SC generation, after being converted to peak power for Gaussian pulses, was compared with the calculated critical power of self-focusing, depending on the product of refractive indices $n_0 n_2$ of all the investigated materials in this work and plotted in Fig. 2.5.

The experimentally established SC generation threshold energies and respective peak powers in LSO ($E_{th} = 300$ nJ, $P_{th} = 1.67$ MW) and LYSO ($E_{th} = 345$ nJ, $P_{th} = 1.92$ MW) were significantly below the calculated value of critical power for self-focusing in these materials ($E_{cr} = 2.24$ MW that converts to $E_{cr} = 403$ nJ in both materials, see Table 2.1 and Fig. 2.5). This result implies that two parabolic band model provides underestimated n_2 values of LSO and LYSO. To solve this issue, the n_2 values of LSO and LYSO were calculated by comparing the experimentally established threshold energies for SC generation in these materials with that of YAG, bearing in mind an identical beam focusing condition, equal sample lengths, comparable energy bandgaps and an apparent similarity of SC generation performances in LSO [Fig. 2.4 (f)],

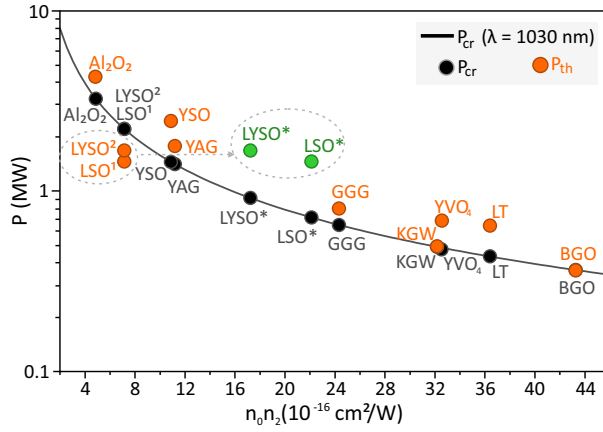


Fig. 2.5 Calculated critical power for self-focusing P_{cr} (black curve and circles) and experimentally determined threshold power P_{th} for supercontinuum generation (orange circles, taking into account Fresnel reflection) for 180 fs 1030 nm pulses. ¹Calculated using two parabolic band model [87], ²estimated according to [88], *evaluated in this work (see text).

LYSO [Fig. 2.4 (g)] and YAG [Fig. 2.4 (h)]. More specifically, this was done by taking the ratio between the corrected (after subtracting Fresnel reflection from an uncoated input face) threshold energies for SC generation measured in LSO and LYSO (labeled in the respective plots) and so the corrected threshold energy in YAG, whose n_2 value is reliably established experimentally, see Table 2.1. Such rough estimation gives the nonlinear refractive index values of $7.6 \times 10^{-16} \text{ cm}^2/\text{W}$ and $6.6 \times 10^{-16} \text{ cm}^2/\text{W}$ of LSO and LYSO, respectively. These revised n_2 values yield the respective critical powers for self-focusing of 1.18 MW and 1.36 MW in LSO and LYSO, which appear reasonable estimates and are included in Table 2.1 and in Fig. 2.5.

The characteristics of the SC spectra generated in all tested materials are summarized in Fig. 2.6. Figure 2.6 (a) compares the blue-shifted portions of SC spectra in the VIS and near-IR range, recorded at threshold energies of SC generation. With 1030 nm pumping, YAG, LSO, LYSO and YSO produce the largest spectral blue-shifts, with the blue cut-off wavelengths (estimated at the 10^{-6} intensity level) below 500 nm: LSO at 450 nm, YAG and sapphire at 460 nm, LYSO at 490 nm and YSO at 465 nm. Modest spectral blue-shifts were measured in KGW (567 nm) and GGG (610 nm), while no SC was produced in the VIS range in YVO₄, LT and BGO, with cut-off wavelengths at 650 nm (LT and YVO₄) and 664 nm (BGO), respectively. Figure 2.6 (b) compares the red-

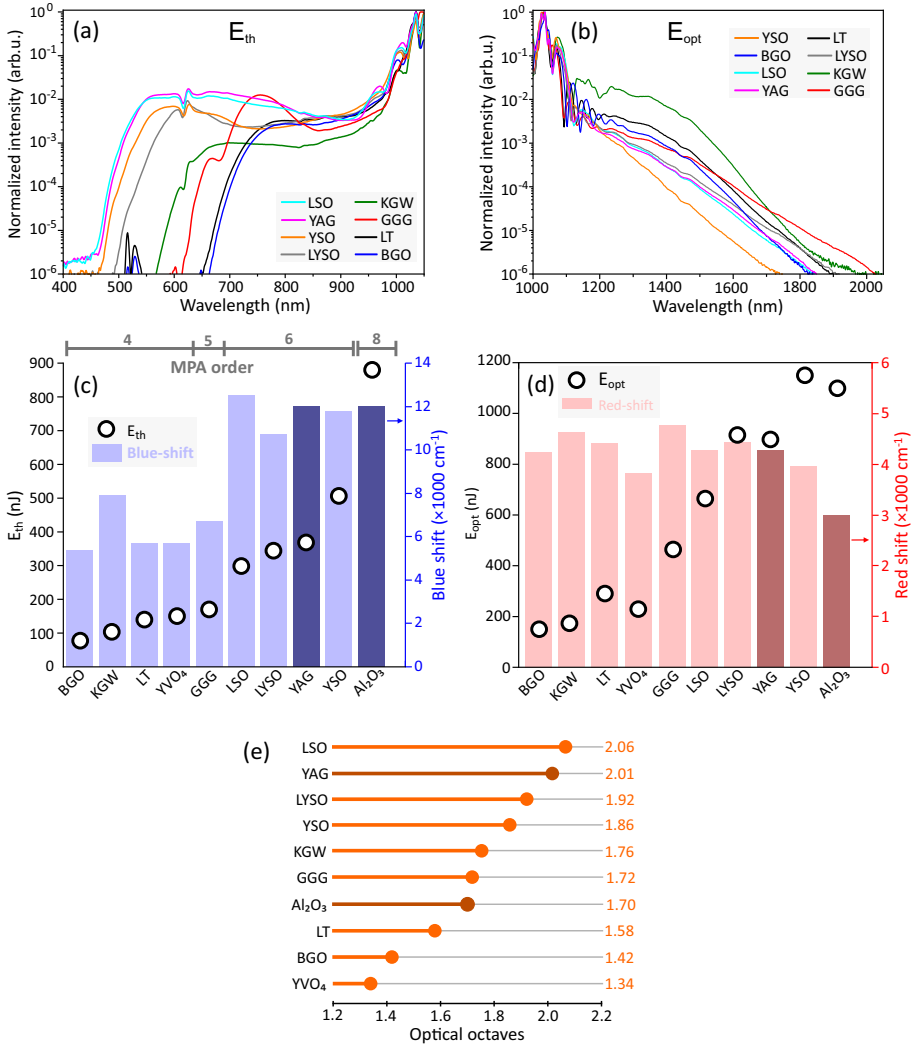


Fig. 2.6 (a) The short-wavelength parts of SC spectra measured at threshold energies E_{th} of SC generation. (b) The long-wavelength parts of SC spectra recorded at optimal pump pulse energies E_{opt} . (c) Threshold energies and corresponding spectral blue-shifts. (d) Optimal pump pulse energies and corresponding spectral red-shifts. Darker shadings in (c) and (d) highlight the results of YAG and Al₂O₃, which served as reference nonlinear materials. (e) Comparison of SC spectral widths expressed in optical octaves at the 10^{-6} intensity level.

shifted portions of SC spectra produced with optimal pump pulse energies. All the tested materials, except sapphire, YVO₄ and YSO, demonstrated reasonably large spectral red-shifts, which exceeded 1800 nm. In that regard, GGG, KGW and LYSO produced the largest spectral red-shifts extending up to 2025 nm,

1965 nm and 1910 nm, respectively (estimated at the 10^{-6} intensity level), exceeding the red-shift produced in YAG (1850 nm). In Fig. 2.6 (c) the spectral blue-shifts are presented in the order of increasing threshold energies, which align well with the calculated values of critical power for self-focusing (see Table 2.1). The top axis of the plot indicates the order of multiphoton absorption K , which was evaluated using Eq. (1.3), where $\hbar\omega_0 = 1.2$ eV. More specifically, the pump pulse experiences four-photon absorption in BGO, KGW, LT and YVO₄, five-photon absorption in GGG, six-photon absorption in LSO, LYSO, YSO and YAG, and eight-photon absorption in sapphire. The spectral data are in line with the SC blue-shift dependence on the material bandgap, and so on the order of MPA [9, 10]. Only KGW crystal drops off this general trend, demonstrating that this nonlinear material, despite its relatively narrow energy bandgap, produces unproportionately large blue-shifted spectral broadening, compared to all the other materials, as seen in Fig. 2.6 (c).

The general increase of optimum pump pulse energy for the optimized red-shifted spectral broadening follows similar trend as the threshold energy, however, there is no bandgap dependence of the spectral red-shift, as demonstrated in Fig. 2.6 (d). The narrow bandgap materials: BGO, LT, KGW and GGG produce reasonably large red-shifted spectral broadenings which are comparable or even larger than those measured in LSO, LYSO and YAG.

Finally, the spectral bandwidth of SC spectra was compared in terms of the optical octaves $N_{oct} = \ln(\lambda_{long}/\lambda_{short})/\ln 2$, where λ_{long} and λ_{short} are the long-wave and short-wave cut-off wavelengths, respectively. The optical octaves were evaluated at an intensity level of 10^{-6} for all the crystals studied and illustrated in Figure 2.6 (e). LSO crystal sample produced the broadest spectrum (2.06 octave-wide), almost identical to the spectrum produced in YAG (~ 2 octaves), but with a 26% lower pump pulse energy. Spectra produced in LYSO and YSO were slightly narrower (~ 1.9 octaves). The narrowest spectra were produced in BGO and YVO₄, spanning less than 1.5 octaves.

The red-shifted part of the SC is of practical importance, especially for what concerns the performance of broadly tunable OPAs pumped by the fundamental harmonics of Yb lasers. The lack of seed photons in the long-wavelength region of the SC spectrum limits the amplification efficiency and results in pulse-to-pulse energy fluctuations around the degeneracy region of the OPA. This aspect is quantified in Fig. 2.7 by plotting the SC spectra in terms of spectral energy density, which was estimated by measuring the energy of the axial part of SC

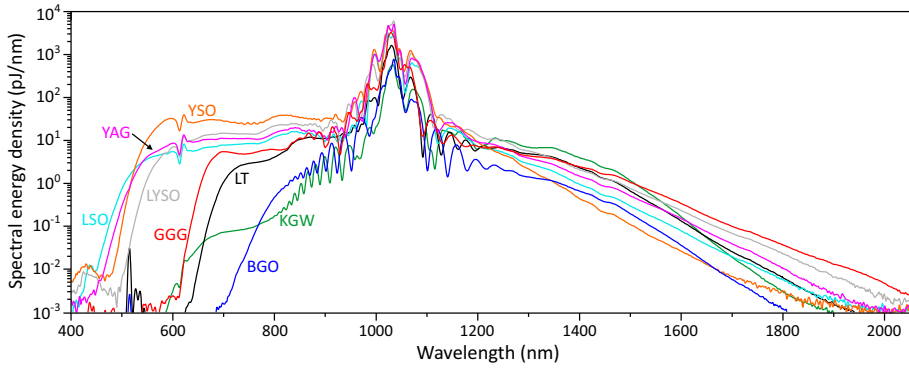


Fig. 2.7 Comparison of spectral energy densities of supercontinua produced in the conditions of optimal pumping in the investigated materials.

radiation (which is the only practically useful part of SC emission). KGW crystal produces the highest spectral energy density in the 1200 – 1450 nm range. The red-shifted part of the SC spectrum in BGO has the lowest spectral energy density, which is 1 – 2 orders of magnitude lower than in the rest of the materials. However, low (< 100 nJ) energy threshold of SC generation, as well as low (< 200 nJ) optimal pump energy in BGO, should be pointed out. The estimated spectral energy densities produced in LSO and LYSO are quite similar to YAG throughout the major part of the SC spectrum. One of the key finding is SC spectrum broadening in GGG crystal, which, despite moderate blue-shifted spectral broadening, produces the largest spectral red-shift and the highest spectral energy density in the 1600 – 2000 nm range, which is almost an order of magnitude higher than that produced in YAG.

2.5 Performances at high laser repetition rates, non-linear losses and bulk heating

The long-term performance of SC generation in crystal samples under optimal pumping conditions at higher laser repetition rates was investigated. The long-term performance tests in LSO, LYSO and YSO revealed gradual narrowing of the SC spectra on the long-wavelength side that occurred after a certain exposure time and could be attributed to the optical degradation of these materials and, eventually, complete extinction of the SC spectrum. For instance, in LSO, the onset of spectral narrowing was observed after ~ 20 min at a laser repetition rate of 10 kHz, while at a laser repetition rate of 20 kHz, stable SC generation

performance was observed just for approximately 2 min. An example of such behavior is shown in Fig. 2.8 (a). The character of spectral changes is highlighted in Fig. 2.8 (d), which shows how the SC spectrum on the long-wavelength side narrows considerably, from 1800 nm to 1450 nm, just after 8 min of exposure time in a stationary sample. Rather similar performance with a gradual narrowing of SC spectrum at long-wavelength region was observed in LYSO Figs. 2.8 (b, e). In contrast, the YSO crystal exhibited an even faster narrowing of the SC spectrum, the long-wavelength broadening completely disappearing after just 6 minutes of operation [Figs. 2.8 (c, f)].

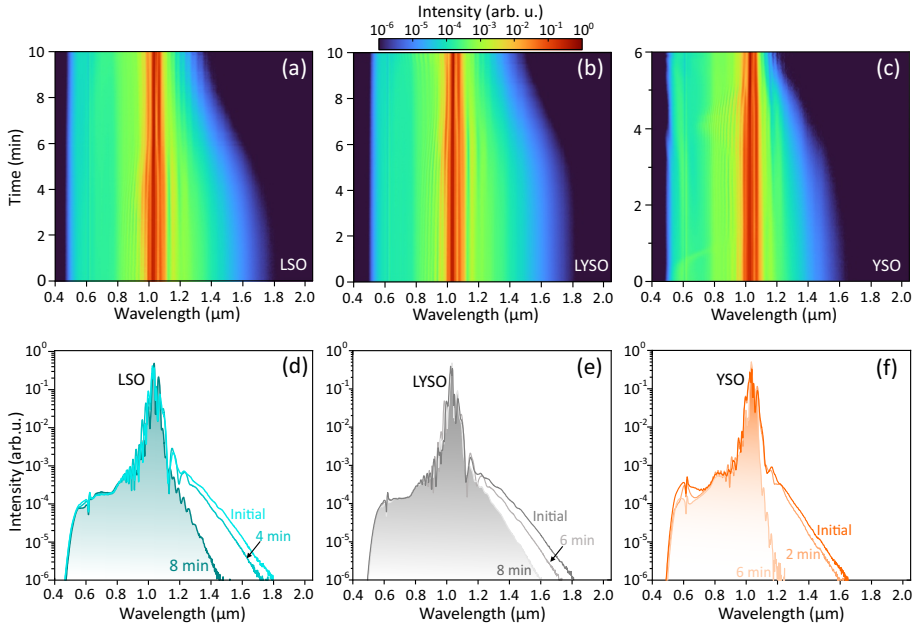


Fig. 2.8 Long-term dynamics of the SC spectra generated with optimum pumping conditions at 20 kHz repetition rate in (a, d) LSO, (b, e) LYSO and (c, f) YSO.

LT crystal demonstrated somewhat better long-term performance, however, rapid narrowing of the SC spectrum in LT crystal was observed after the first few minutes of operation when the pulse repetition rate was set at 200 kHz [Figs. 2.9 (a, d)]. In contrast to LSO, LYSO, YSO and LT crystal samples, BGO and GGG demonstrated excellent SC generation performances without any spectral changes at pulse repetition rate of 200 kHz, as shown in Fig. 2.9 (b) and (c), respectively. For detailed illustration, Figure 2.9 (e) and (f) demonstrate identical shapes of SC spectra at the beginning and at the end of 1 hour-operation in both BGO and GGG materials, pumped by optimal energy pulses.

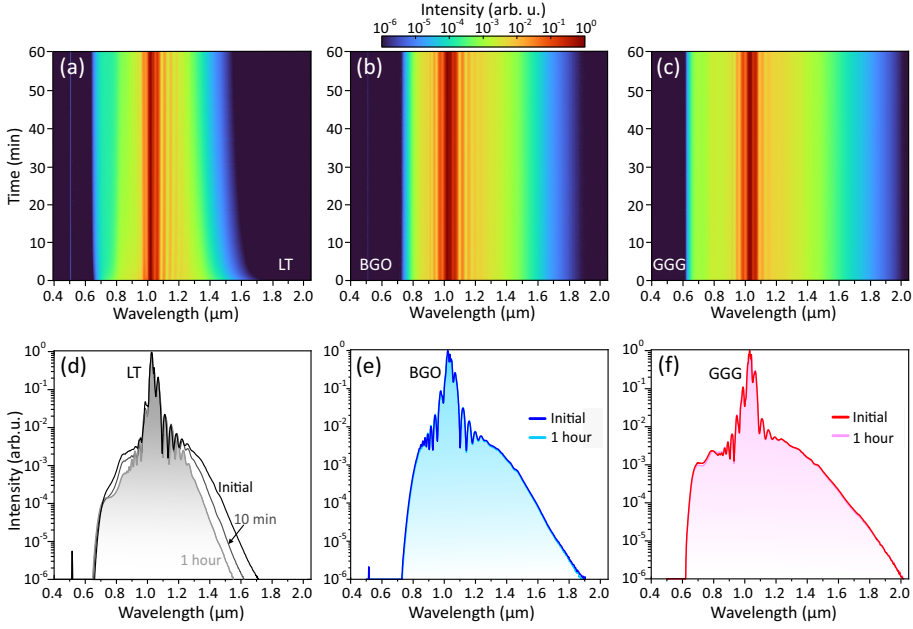


Fig. 2.9 Long-term dynamics of the SC spectra generated at optimum pumping conditions at 200 kHz repetition rate in (a, d) LT, (b, e) BGO and (c, f) GGG.

Energy deposition to the transparent material via multiphoton absorption and free electron plasma absorption due to the inverse Bremsstrahlung effect, which are among the key players in the filamentation process, lead to heat accumulation at high repetition rates, such as 25 MHz [114]. This may result in gradual structural modification, or, in other words, optical degradation of the material, which in turn causes shrinking and eventually the extinction of the SC spectrum with time. Therefore, to gain further insight into the crystal performance from the perspective of long-term operation, nonlinear transmission and bulk heating were measured for each material as a function of input pulse energy.

The measured transmissions of all the studied samples as functions of the input pulse energy after subtracting Fresnel reflections from crystal input and exit faces, are presented in Fig. 2.10. The onset of nonlinear losses (the drop in transmission) is associated with an increase of the beam intensity due to self-focusing, and eventually, formation of a light filament.

The estimated nonlinear losses in the operating conditions at the optimal input pulse energies yielded absorbed energy values, which were then converted to absorbed powers, as presented in Fig. 2.11. KGW and BGO crystals exhibited

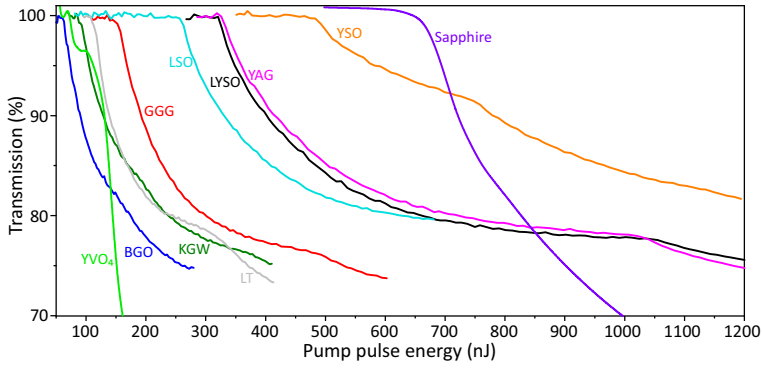


Fig. 2.10 Measured total energy transmittance of various studied crystal samples versus the energy of pump pulses.

the lowest nonlinear losses, both under 20%, and correspondingly the lowest absorbed energies of ~ 24 nJ. These values are approximately 7 and 14 times lower than those observed in YAG and sapphire, respectively. YVO₄ exhibited an absorbed energy of 86 nJ, with relatively high nonlinear losses of 43%, which is comparable to GGG, showing 97 nJ of absorbed energy and nonlinear losses of 24%.

The effect of absorbed power on bulk heating was investigated by mounting the samples on a Teflon base and performing the surface temperature measurements after 10 minutes of continuous exposure, when sample temperature has fully settled reaching a certain equilibrium value. Although the heat accumulation is apparently proportional to the absolute amount of absorbed energy and power, on the other hand, the measured surface temperatures are related also to sample dimensions and thermal conductivity of the material, so this measurement gives just a raw approximation of thermal regime, which nevertheless is important to know from a practical point of view.

Figures 2.12 (a) show the thermal vision camera images of KGW (the sample dimensions $7 \times 7 \times 10$ mm³) and YVO₄ (the sample dimensions $3 \times 5 \times 10$ mm³) crystals operated at 2 MHz repetition rate and optimal input pulse energies of 180 nJ and 230 nJ, respectively. The measured surface temperatures of KGW and YVO₄ samples were 31 °C and 41 °C, respectively, which are well below that of e.g., sapphire sample (the sample dimensions $5 \times 5 \times 6$ mm³), which heated up to 92 °C at its optimal input pulse energy of 1.1 μ J due to the largest absolute amount of absorbed power (750 mW), see Fig. 2.11. In practice, the bulk heating could be efficiently mitigated by using an appropriate heat sink.

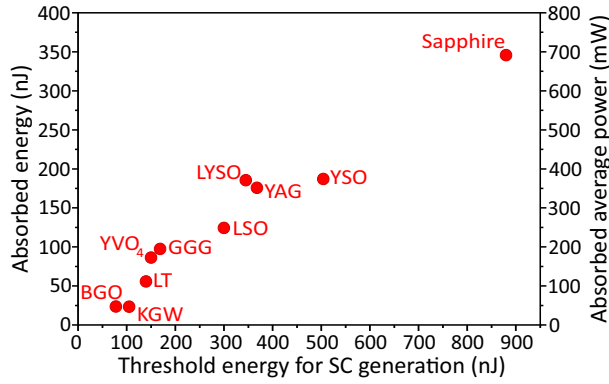


Fig. 2.11 Comparison of absolute absorbed energy into different sample crystals pumped with E_{opt} energy pulses for SC generation. Average power calculated at 2 MHz repetition rate.

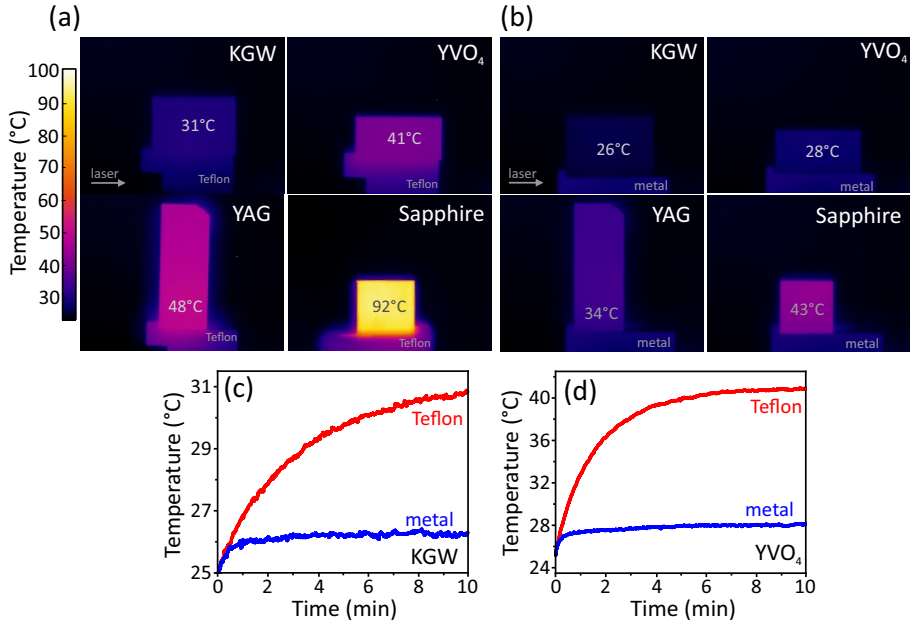


Fig. 2.12 Thermal vision camera images of KGW, YVO₄, YAG and sapphire samples mounted on (a) Teflon base and (b) aluminium heat sink recorded after 10 min of operation at 2 MHz repetition rate with the optimal input pulse energies, respectively. Comparison of thermal dynamics of surface temperature of (c) KGW and (d) YVO₄.

Mounting KGW, YVO₄, YAG and sapphire samples on an aluminium heat sink resulted in a reduction of sample temperatures to 26 °C, 28 °C, 34 °C and 43 °C, respectively [Fig. 2.12 (b)].

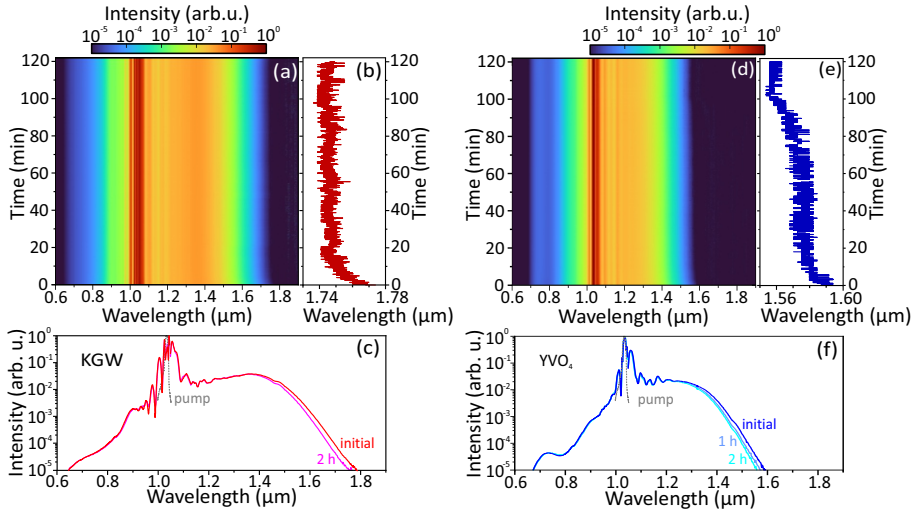


Fig. 2.13 (a, d) Long-term dynamics of SC spectra, (b, e) long-wavelength side dynamics of SC spectra at 10^{-5} intensity level and (c, f) comparison of the initial SC spectrum shape and after 2 hours of operation pumped with optimal energy pulses in KGW and YVO₄, respectively.

Finally, the long-term performance of SC generation in KGW and YVO₄ crystals was investigated. In the current experiment, the crystal samples were mounted on a metal heat sink and kept in a stationary position with respect to the pump beam. KGW crystal exhibited slight spectral narrowing during the first ~ 15 minutes of operation Fig. 2.13 (a, b), which correlate well with the time required for the crystal to reach thermal equilibrium [Fig. 2.12 (c)]. This was followed by stable performance with no further changes in the SC spectrum over the subsequent 2 hours of operation, attesting no optical degradation of the material, as illustrated in Fig. 2.13 (c). Even when mounted on a Teflon base, the crystal exhibited the same long-term dynamics of SC spectra. YVO₄ crystal also demonstrated an apparently stable performance, see Fig. 2.13 (d), however, closer inspection of the spectral dynamics in time revealed a slight but gradual narrowing of the SC spectrum on the long-wavelength side by ~ 25 nm over 2 hours of operation Fig. 2.13 (e, f), which is beyond time it takes to reach thermal equilibrium [Fig. 2.12 (d)]. A simple test by translating the sample into an unexposed position showed an entirely recovered SC spectrum, so the observed spectral narrowing is indeed a signature of slow optical degradation of YVO₄ crystal under present operating conditions. On the other hand, since the

material degradation manifests over a relatively long period (tens of minutes), it could be avoided by placing the crystal on the motorized translation stage.

2.6 Summary and outlook

To summarize the results of this Chapter, it was demonstrated that narrow (KGW, YVO₄, BGO, LT) and medium (GGG, YSO, LSO, LYSO) bandgap dielectric crystals are efficient nonlinear materials for broadband SC generation in the near-infrared and short-wave infrared spectral ranges, when pumped by ~200 fs fundamental harmonic pulses from an amplified Yb:KGW laser. YSO, LSO and LYSO produced two octave-spanning SC spectra, which compare to SC spectra produced in YAG. These materials exhibit quite similar performances to YAG also in terms of threshold and optimal pump pulse energies for SC generation. However, YSO, LSO and LYSO show durable operation only at 10 kHz and quickly degrade at 20 kHz. The observed stable and durable damage-free performance of BGO and GGG at 200 kHz pulse repetition rate suggests that these nonlinear materials have a potential for SC generation at even higher, MHz, repetition rates. Owing to its large nonlinearity, BGO exhibited the lowest SC generation threshold (78 nJ) among the investigated materials, which is 25% lower than in KGW and could be considered as excellent nonlinear material for very low-threshold SC generation. It was also shown, that compared to YVO₄, KGW crystal demonstrated a better performance in terms of attainable spectral extent, bulk heating and optical degradation at 2 MHz pulse repetition rate, emerging as a very useful asset for the design of high-speed spectroscopic and imaging systems which employ broadband pulses based on SC generation. The production of more than octave-wide SC spectra with remarkably large spectral red-shifts, which in combination with low filamentation and SC generation thresholds offer suitable energy trade-off between the seed production and amplification channels for high average power ultrafast OPAs operating in the near- to mid-IR spectral range. Finally, it was suggested that filament-induced luminescence could be viewed as experimentally simple and cost-effective method for investigating the luminescence properties, such as spectra and decay times (by performing time-resolved measurements) of scintillator crystals.

Chapter 3

Supercontinuum generation at 76 MHz pulse repetition rate

Material related to this chapter was published in [A2]

3.1 Motivation

Photonic crystal fibers (PCFs) and waveguides are indispensable highly non-linear media for SC generation with ultrashort pulses carrying energies from a few nJ to a few tens of nJ at high (~ 100 MHz) pulse repetition rates provided by modern state-of-the-art ultrafast laser oscillators [115–117]. Solid core PCFs and waveguides enable very large nonlinearities along with the possibility of dispersion engineering, and these unique features are ideally suited for the generation of octave-spanning SC [118–120] and spectral broadening-based pulse post-compression [121, 122]. Compared to guided wave geometries, SC generation in bulk solid-state materials offers several advantages such as of simplicity in experimental implementation, beam alignment insensitivity and high temporal coherence of broadband pulses that is maintained for a broad range of the input pulse widths. However, the critical power for self-focusing in conventional nonlinear materials such as sapphire and YAG in the near-infrared exceeds 1 MW, which is well above the peak power of the state-of-the-art ultrafast laser oscillator pulses, so basically limiting the application of this SC generation technique to amplified laser systems.

So far, the feasibility of low threshold SC generation in structured bulk materials featuring both, quadratic and cubic nonlinearities, and hence encompassing

rather specific regimes of the nonlinear propagation was demonstrated. In that regard, low-threshold SC generation in the visible and near-IR was reported in orientation-patterned gallium phosphide with 100 fs, 32 nJ pulses from an amplified 100 MHz Yb: fiber laser [123] as a result of quasi-phase-matched second harmonic generation and optical parametric amplification of SPM-induced sidebands. Multioctave SC spectrum spanning from the visible to the long-wave infrared in polycrystalline zinc sulphide was generated with 2.4 μm , 3-optical cycle, 15 nJ pulses from Cr:ZnS oscillator, exploiting the interplay between the effects arising from the cubic nonlinearity, random quasi-phase matching due to quadratic nonlinearity, and thermal optical effects [124, 125].

For what concerns low threshold SC generation in homogeneous bulk materials, intracavity SC generation was reported within Ti:sapphire oscillators operating at 100 MHz, where large-scale spectral broadening emerged in the lasing material itself from a combined action of SPM, mode-locking process, laser gain, proper dispersion management, and choice of broadband mirror reflectivity [126–128]. Such intracavity technique is basically applicable to Ti:sapphire oscillators only because of extremely broad gain bandwidth supported by this unique lasing material and is not achievable in Yb oscillators. On the other hand, at the oscillator output, just SPM-induced spectral broadening was demonstrated in diamond with 6.5 fs, 5.6 nJ pulses, which was thereafter exploited for pulse compression [129]. Beam filamentation, conical emission and pulse splitting that underly SC generation were not reported in any of the above cases. An interesting note on the possibility to generate SC in KGW crystal with 7 fs, 16 nJ pulses from 80 MHz Ti:sapphire oscillator was reported, unfortunately, without providing any further details apart from the observation of conical emission, which is a signature of beam filamentation [12]. From a perspective of nonlinear optics, KGW and YVO₄ exhibit large nonlinear indexes of refraction ($n_2 = 1.6 \times 10^{-15} \text{ cm}^2/\text{W}$ and $n_2 = 1.5 \times 10^{-15} \text{ cm}^2/\text{W}$, respectively, see Table 2.1) and subsequently low SC generation threshold. As discussed in Chapter 2, undoped KGW and YVO₄ crystals demonstrate excellent SC generation performance with amplified Yb: fiber and Yb: KGW lasers operating at a few MHz repetition rates [43].

This Chapter is devoted to an experimental study of high average power, low threshold, octave-spanning SC generation in undoped KGW and YVO₄ crystals pumped by ~ 100 fs and sub-100 nJ pulses from amplified and unamplified

Yb:KGW oscillator at 76 MHz pulse repetition rate, which was unambiguously attested by the distinctive features of the SC generation phenomenon.

3.2 Supercontinuum generation with amplified Yb:KGW oscillator pulses

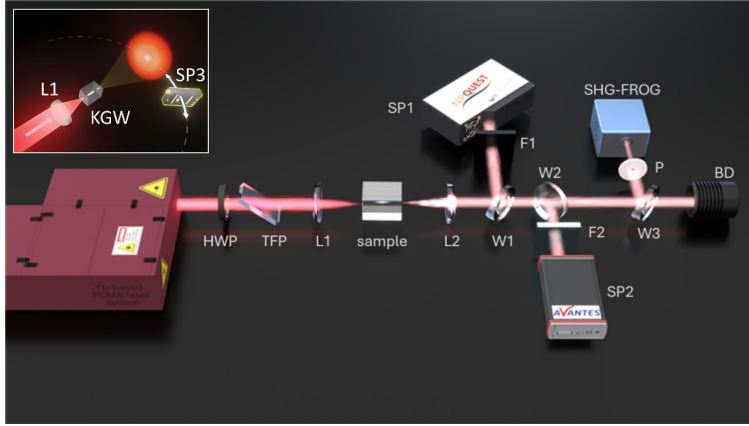


Fig. 3.1 The experimental setup: HWP, half-wave plate; TFP, thin-film polarizer; L1, focusing lens; W1, W2, W3, fused silica wedges; F1, long-pass filter; F2, short-pass filter; SP1, NIR-SWIR spectrometer; SP2, UV-NIR spectrometer; L2, collimating lens; P, pinhole; SHG-FROG, second-harmonic generation-based frequency-resolved optical gating setup; BD, beam dump. The inset shows an arrangement for the measurement of angle-resolved spectrum with a mini-spectrometer, SP3.

The first experiment was performed using a commercial Yb:KGW oscillator (FLINT, Light Conversion Ltd.) with a home-built pre-chirp managed rod-type single pass Yb fiber amplifier (PCMA) stage, which operated at a repetition rate of the oscillator (76 MHz) and provided 75 fs pulses with a central wavelength of 1038 nm, and a maximum average power of up to ~ 20 W [130]. The experimental setup is sketched in Fig. 3.1. The laser beam with a diameter of 2.1 mm at the $1/e^2$ intensity level was focused with an anti-reflection coated lens L1, ($f = +100$ mm), which is equivalent to the NA of 0.011, onto the front face of uncoated and undoped KGW and YVO₄ crystal samples of 10 mm length (Eksma Optics, Optogama), that were placed on a metal holder and kept in a stationary position with respect to the laser beam. The spectra were recorded using the same experimental setup as described in Chapter 2. Pulse energy was

varied with an attenuator consisting of a half-wave plate (HWP) and a thin-film polarizer (TFP).

For what concerns focusing conditions, several focusing geometries were tested. The $NA = 0.011$ operating conditions was found to be optimal in terms of the SC generation threshold, achievable spectral extent and robustness in the long-term operation. The onset of optical damage in the KGW crystal was observed after 7 minutes of operation with tighter focusing ($NA = 0.015$). Finally, loose focusing ($NA = 0.008$) into 30 mm long KGW crystal did not enhance the spectral extension of the output radiation.

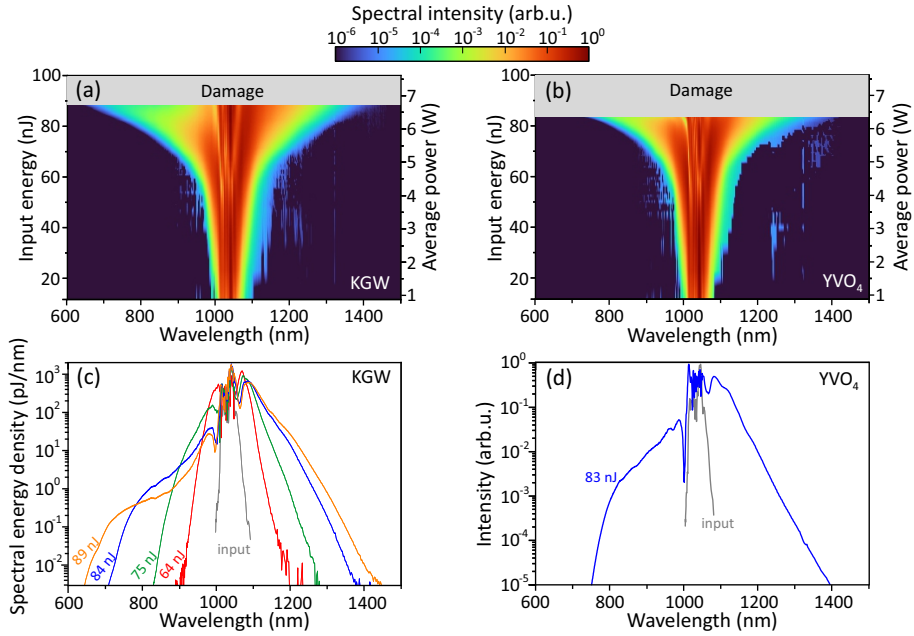


Fig. 3.2 The dynamics of spectral broadening in (a) KGW and in (b) YVO₄ versus the input pulse energy and average power (with an account for Fresnel reflection). Comparison of the SC spectra measured with different pump pulse energies in (c) KGW and (d) YVO₄ crystal samples.

The evolution of the output spectra in KGW and YVO₄ crystals is presented in Fig. 3.2 for average pump power increasing up to 7.6 W, corresponding to a maximum single pulse energy of 100 nJ (with an account for energy losses due to Fresnel reflection). In KGW [Fig. 3.2 (a)], a gradual spectral broadening around the carrier wavelength due to SPM is observed when increasing the average pump power to 4.6 W (the pulse energy 61 nJ). A much faster spectral broadening was observed starting with the pulse energy of 64 nJ, which was

defined as the threshold energy for SC generation that was accompanied by the emergence of conical emission. The SC spectrum continued to broaden until the average power was increased up to 6.84 W (the pulse energy 90 nJ), where immediate damage in the bulk of material occurred, emerging as a momentarily white flash, after which only strong scattering from the damage site was observed.

Figure 3.2 (c) presents the characteristic SC spectra recorded with different pump pulse energies and plotted in terms of spectral energy density which is a crucial parameter for SC-based applications. Evaluated spectral energy densities are in the order of one-hundredth to one-tenth of pJ/nm even in the spectral wings of supercontinuum. An octave-spanning SC spectrum in the 715 – 1400 nm range (evaluated at the 10^{-6} intensity level) with an average power of 4.9 W was produced with the pump pulse energy of 84 nJ (the average pump power of 6.4 W), which is further considered as the optimal energy (power) for SC generation as it is also safely below the multipulse damage threshold. A similar trend of spectral broadening was observed for YVO₄ crystal [Fig. 3.2 (b)]. Rapid spectral broadening with the increase of pump pulse power up to 6.48 W (85 nJ) was observed until the effects of catastrophic optical damage took place. The optimal energy (power) for SC generation in an YVO₄ crystal, producing a spectrum in the 735 – 1400 nm range (evaluated at the 10^{-5} intensity level), was achieved with a slightly lower pump pulse energy of 83 nJ (average power 6.3 W) [Fig. 3.2 (d)].

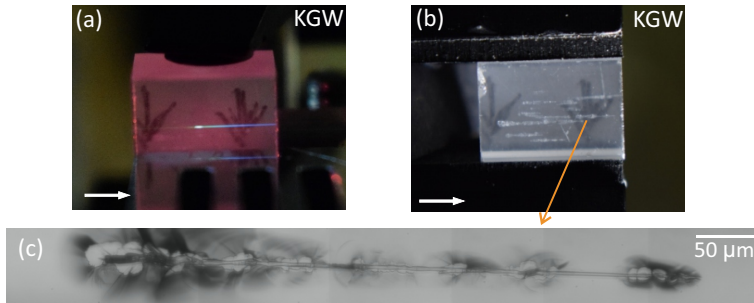


Fig. 3.3 Screenshots of a side view of the KGW crystal (a) during operation and (b) filamentation-induced tracks of catastrophic optical damage. (c) A view of one of the tracks magnified 40 times using an optical microscope. A white arrow marks the propagation direction of the laser pulse.

Figure 3.3 (a) presents a side view of KGW crystal in operation with an optimal pump pulse energy/average power (84 nJ/6.4 W). Figure 3.3 (b) shows

the damage tracks inside the crystal, which developed after irradiation with higher energy (89 nJ) pulses. A 40 \times magnified image of one of the damage tracks is shown in Fig. 3.3 (c), revealing darker areas that indicate laser-induced breakdown, material remelting, and strain surrounding the track of modified refractive index, which had a diameter of approximately 5 μm .

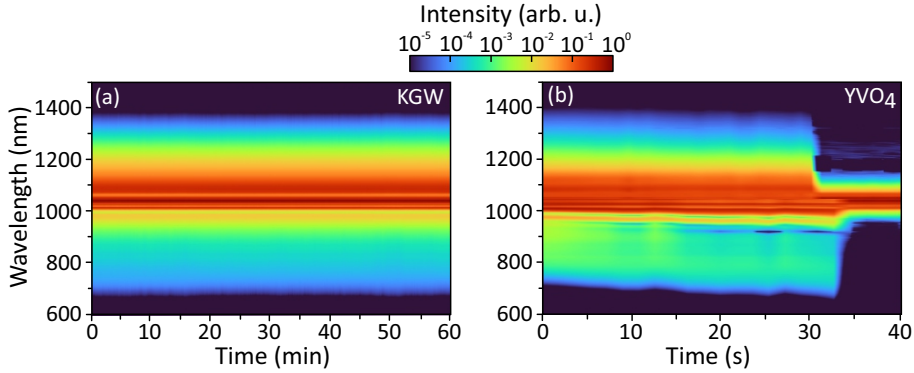


Fig. 3.4 Long-term dynamics of the SC spectra generated with amplified 76 MHz Yb:KGW oscillator pulses with an optimal average pump power of (a) 6.4 W in KGW crystal and (b) 6.3 W in YVO₄ crystal.

Finally, the long-term performance of SC generation was investigated under optimal pumping conditions (average power of 6.4 W and 6.3 W) with amplified Yb:KGW oscillator pulses in both KGW and YVO₄ crystal samples. In KGW crystal, stable performance was justified by excellent reproducibility of the SC spectrum without any translation of the crystal was observed for over 1 hour of operation, attesting no detectable optical degradation of the material, as illustrated in Fig. 3.4 (a). In contrast, a relatively stable operation of the YVO₄ crystal was recorded just for ~30 seconds before the complete extinction of SC occurred due to multipulse optical damage [Fig. 3.4 (b)], which eventually manifested by sample fracture.

The detailed temporal characterization of the SC was performed by means of the well-established second-harmonic generation-based frequency-resolved optical gating (SHG-FROG) technique, using a home-built setup that employed a 50 μm thick beta-barium borate (BBO) crystal. In doing so, the SC beam was reflected from fused silica wedge W3 (with wedges W1 and W2 removed) and sent through a Teflon pinhole with a diameter of 1.2 mm, transmitting only the very central part of the filament and blocking its periphery and conical emission (Fig. 3.1). This was necessary due to the complex spatio-temporal structure of

the light filament since the measurement of a spatially-integrated beam would otherwise yield a long and featureless temporal profile [131].

SHG-FROG measurements of the pump pulses are presented Figs. 3.5 (a-c), where Fig. 3.5 (a) shows the measured and retrieved SHG-FROG traces, Fig. 3.5 (b) shows the measured and retrieved spectra and retrieved spectral phase, and Fig. 3.5 (c) shows the reconstructed pulse profile and phase, yielding a pulse duration of 75 fs, with a root mean square reconstruction error of 0.18%.

The measured and reconstructed (reconstruction error of 1.4%) SHG-FROG traces of the SC pulse obtained with the pump pulse energy of 64 nJ (~ 4.9 W) are shown in Fig. 3.5 (d). Fig. 3.5 (e) compares the measured and retrieved spectra along with retrieved spectral phase. Although the retrieved SC spectrum exhibits a fine structure which is not visible in the measured spectrum due to averaging a high number of shots, there is a nearly perfect match between the measured and retrieved spectra. Figure 3.5 (f) shows the pulse profile and temporal phase. The retrieved temporal profile reveals a double-peaked temporal shape, indicating two characteristic sub-pulses that emerge after pulse splitting at the vicinity of the nonlinear focus in the range of normal GVD, as this is the case for the pump pulse wavelength of 1038 nm in KGW; its zero GVD point is at 2.2 μm , as extrapolated from the refractive index dispersion measured in the 350 – 1500 nm range [132].

Figure 3.5 (g) presents the results of SHG-FROG measurements performed with the optimal (84 nJ, 6.4 W) pump pulse energy, which produces the broadest SC spectrum without the risk of optical damage of the nonlinear material. There is a good agreement between the measured and reconstructed (root mean square reconstruction error of 0.2%) SHG-FROG traces [Fig. 3.5 (g)] and spectral profiles [Fig. 3.5 (h)], while there is a discrepancy in spectral wings below the 10^{-3} intensity level. The estimated BBO phase matching bandwidth is 7000 cm^{-1} (661 – 1415 nm), as calculated with the program SNLO [133] and evaluated at $1/e$ intensity level, suggesting that the difference between the retrieved and experimental spectra is not related to the limited bandwidth of the BBO crystal, but rather could be attributed to imperfections in the retrieval algorithm. The retrieved temporal profile of SC radiation is depicted in Fig. 3.5 (i), showing an emergence of an intense peak in between the split sub-pulses, which is reconstructed from the peripheral part of the filament [66]. Both SHG-FROG measurements presented in Fig. 3.5 (d-i) demonstrate that the retrieved sub-pulses possess well-behaved spectral phases, justified by their

near-parabolic shapes, suggesting that these sub-pulses are compressible close to the transform limit.

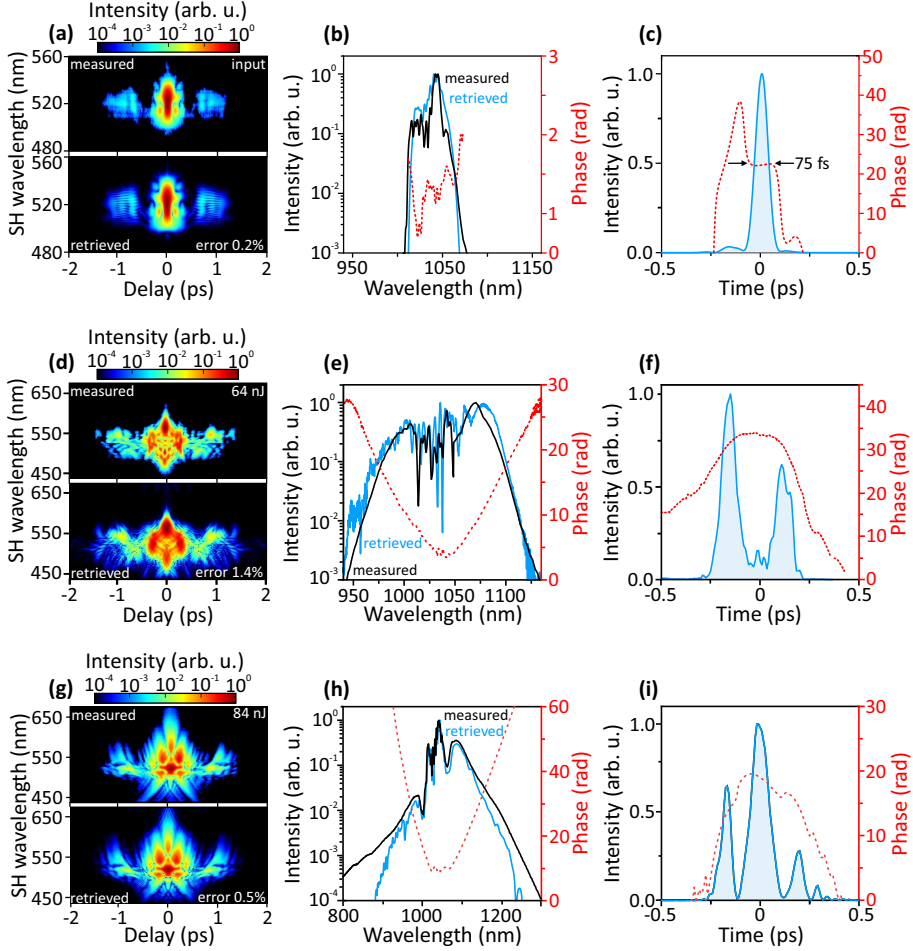


Fig. 3.5 The SHG-FROG measurements of (a-c) input pulse, (d-f) SC generated pumped with 64 nJ energy pulse and (g-i) SC pulse with 84 nJ energy pulse from amplified 76 MHz Yb:KGW oscillator. (a, d, g) The measured and retrieved SHG-FROG traces (SHG-FROG reconstruction errors of 0.2 %, 1.4 %, 0.5 %, respectively), (b, e, h) the retrieved spectral intensities (blue) and phases (red), compared to the independently measured spectra with a spectrometer (black). The retrieved temporal profiles shows (c) input pulse, (f) two sub-pulses resulting in self-phase modulation and filamentation and (i) triple-peaked temporal shape as expected during the SC generation.

3.3 Supercontinuum generation with unamplified Yb:KGW oscillator pulses

The second experiment was performed using an unamplified commercial Yb:KGW oscillator (FLINT, Light Conversion Ltd.), which provided the maximum average power of 6.5 W, operated at 76 MHz repetition rate and provided 110 fs pulses with a central wavelength of 1030 nm. The same KGW crystal was used for SC generation under optimal focusing conditions. In the present experiment, only the blue-shifted part of the SC spectrum was recorded, showing that SC spectrum extends up to ~ 700 nm, evaluated at the 10^{-6} intensity level, under optimal pump pulse power of 6.4 W [Fig. 3.6 (a)]. Stable operation for 4 hours was recorded without any translation of the crystal, as illustrated in Fig. 3.6 (b), which shows the long-term dynamics of the blue-shifted portion of the SC spectrum.

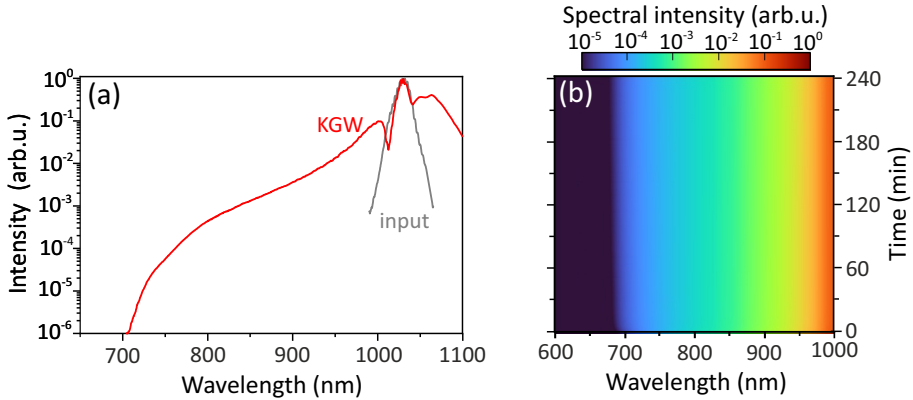


Fig. 3.6 (a) Short-wavelength portion of supercontinuum spectrum in KGW crystal and (b) long-term dynamics of the supercontinuum spectra generated with optimal pump pulse power of 6.4 W 76 MHz Yb:KGW oscillator pulses.

No essential difference in filamentation and SC generation dynamics with 75 fs and 110 fs pulses is expected because of the intensity clamping effect imposed by the multiphoton absorption and plasma defocusing, especially bearing in mind relatively loose focusing (NA 0.01 in the both cases) of the pump beam. Although the difference in the pump pulse widths may result in slightly different position of the nonlinear focus with respect to the input face of the sample, it has no apparent impact on the SC spectrum at the output in the case of relatively long (10 mm) length of the nonlinear material. This could be

easily verified by comparing SC spectra on the short wavelength side produced with 75 fs [Fig. 3.2 (b)] and 110 fs [Fig. 3.6 (a)] pulses, respectively, serving as a proof for the above considerations.

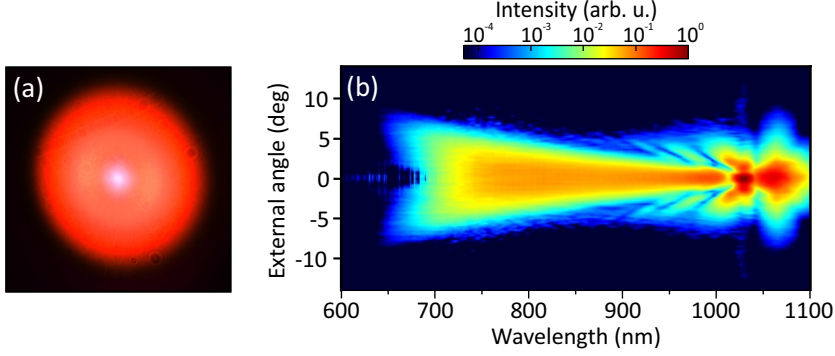


Fig. 3.7 (a) Screenshot of the SC emission pattern produced by optimal input power of 6.4 W unamplified Yb:KGW oscillator pulses. (b) The angle-resolved supercontinuum spectrum.

Figure 3.7 presents the results of additional measurements performed with unamplified pulses, which are attributed to characteristic features of filamentation and SC generation. Figure 3.7 (a) shows the SC emission pattern projected onto the paper screen, which was produced by filamentation of the unamplified oscillator pulses with an energy of 84 nJ, corresponding to an average power of 6.4 W. The SC appears as a bright spot in the center, surrounded by red conical emission distributed over wide angle range, which is a distinctive feature of beam filamentation. Fig. 3.7 (b) displays the angle-resolved SC spectrum, which was measured with a mini-spectrometer (SP3, Qmini VIS-LC, Broadcom Inc., the detection range 293 – 1115 nm) mounted on a motorized rotating arm with an approximate length of 22 cm, see the inset of Fig. 3.1. The wavelength range of angle-resolved SC spectrum was limited by the detection range of the mini-spectrometer. The measurement nicely captures a characteristic angular spread of the blue-shifted spectral components resembling a "fish-tail" that comprises the conical emission.

3.4 Summary and outlook

To conclude the results of this Chapter, high average power, low threshold, octave-spanning SC generation in undoped KGW crystal, pumped by either

amplified or unamplified ~ 100 fs pulses from a commercial Yb:KGW oscillator with pulse repetition rate of 76 MHz is demonstrated. In both cases, robust and damage-free performance was achieved with a total average pump power of 6.4 W, while keeping the sample at a stationary position with respect to the pump beam. The temporal characterization of the SC pulses by SHG-FROG technique captured pulse splitting, which is a universal feature of filamentation and SC generation in the range of normal GVD of the nonlinear material. The retrieved sub-pulses were shown possessing well-behaved spectral phases, suggesting their compressibility close to the transform limit.

From a practical point of view, these results demonstrate a robust and reliable oscillator-driven all-solid-state platform for SC generation, which could readily serve as an attractive alternative to alignment-sensitive SC generation schemes based on guided wave geometries, offering improved designs for high repetition rate and high average power ultrafast light sources based on spectral broadening and optical parametric amplification [134, 135], control of carrier-envelope offset phase [136], as well as for compact oscillator-driven time-resolved pump/supercontinuum probe spectrometers [137], and any other high-speed imaging and spectroscopic systems that employ SC generation.

Chapter 4

All-solid-state post-compression of low-energy pulses at 76 MHz pulse repetition rate

Material related to this chapter was published in [A4]

4.1 Motivation

Extracavity compression, or post-compression, of laser pulses that relies on increasing the spectral bandwidth via SPM in a nonlinear medium and subsequent removal of the frequency modulation by using an appropriate dispersive delay line constitutes a simple and efficient method for the generation of ultrashort pulses whose spectral bandwidths extend well beyond the gain bandwidths supported by the driving laser sources [138, 139]. Among various pulse compression methods developed so far, pulse compression based on SPM-induced spectral broadening in bulk solid-state materials offers the advantages of technical simplicity, low cost, and easy implementation to virtually any existing ultrashort pulse laser system, but requires avoiding or proper managing of nonlinear effects in the spatial domain (i.e., self-focusing) [65].

At present, the all-solid-state pulse post-compression technique is widely attracting a renewed practical interest, inspired by the advent of ultrafast Yb lasers. To date, it has been demonstrated in a variety of setups, unveiling the potential of scalability to high peak [140, 141] and average [142–144] powers, as well as achieving huge (120-fold) compression factors [145]. In particular, all-

solid-state pulse post-compression has emerged as a very attractive and useful technique to compress the relatively long femtosecond and sub-picosecond pulses delivered by various rapidly developing high-average-power Yb-laser sources. Second-order cascading in materials with second-order nonlinearity [146, 147], multi-plate [148–150] and multi-pass [142, 151, 152] techniques, as well as multistage [153] and hybrid [154, 155] approaches, were recently developed to achieve large compression factors and provide few-optical-cycle pulses. In contrast to conventional single- or few-pass schemes, multi-plate and multi-pass geometries rely on spectral broadening in distributed thin plates instead of a single thick piece of bulk nonlinear medium, so ensuring good beam quality and uniform spectral distribution across the beam. The idea of multi-plate/multi-pass spectral broadening technique is that individual thin plates of the nonlinear medium are distributed in space so that the pulse exits each plate with a slightly broadened spectrum, but before the onset of beam self-focusing. Any small-scale spatial distortions of the beam are then washed out by diffraction during free-space propagation, before the beam enters the next plate.

These techniques are perfectly suited to spectrally broaden and compress the ultrashort pulses from high power Yb thin-disc oscillators and pulses from amplified Yb laser systems, with energies ranging from several μJ to several mJ; see, e.g., [156], whereas the SPM-induced spectral broadening of pulses with an energy of several hundreds of nJ is usually performed in highly nonlinear fibers [157–159]. More recently, spectral broadening and soliton compression of low-energy pulses in bulk materials featuring a second-order nonlinearity was demonstrated as an interesting and feasible alternative [160, 161]. However, spectral broadening of such pulses in bulk solid-state materials with pure cubic nonlinearity has received only a little attention so far [129].

In this Chapter, a proof-of-principle of a simple all-solid-state post-compression setup for low-energy (210 nJ), high-repetition-rate (76 MHz) laser pulses is demonstrated, where spectral broadening was performed using a combination of highly nonlinear bulk materials (ZnS, YAG and KGW) in a simple single-pass geometry and subsequent pulse compression was performed using Gires–Tournois interferometric (GTI) mirrors.

4.2 Experimental details

In the experiment, the laser source was a home-built PCMA system, the same as that described in Chapter 3, in the present case delivering 210 nJ, 75 fs pulses at 76 MHz repetition rate with an average power of 15.7 W and a peak power of 2.5 MW. The experimental setup is depicted in Fig. 4.1 (a). The long-term output power stability of the entire laser system was high, with a root mean square (rms) fluctuation of 0.53%, as measured over 24 h of operation. The SPM-induced spectral broadening was performed in a two-stage arrangement that combined sequential propagation in several highly nonlinear materials: ZnS (uncoated, 2 mm thick, $n_0 = 2.29$ [162], $n_2 = 68 \times 10^{-16} \text{ cm}^2/\text{W}$ [163]), KGW (uncoated, 6 mm thick) and YAG (uncoated, 15 mm thick). For the n_2 values of KGW and YAG crystals, refer to Table 2.1.

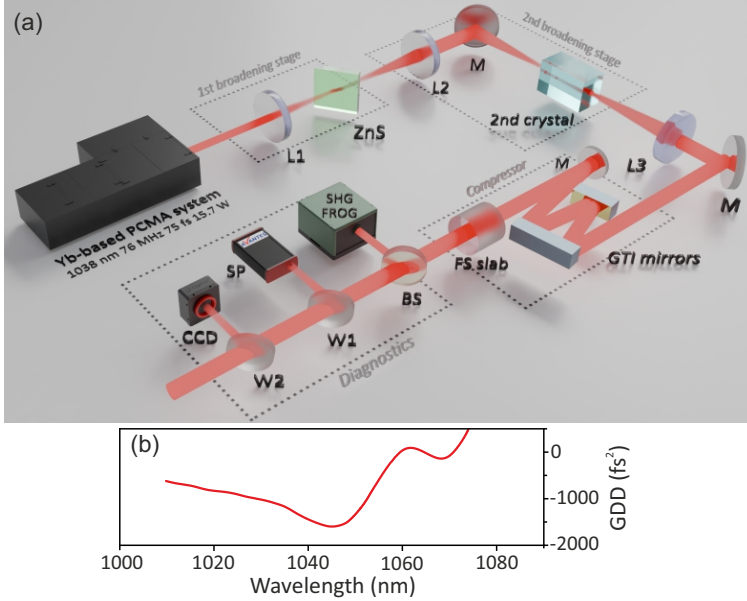


Fig. 4.1 (a) Experimental setup for all-solid-state post-compression of low-energy pulses. L1, L2, focusing lenses; M, beam-steering mirrors; BS, beam splitter; W1, W2, fused silica wedges; L3, collimating lens; GTI mirrors, Gires–Tournois interferometric mirrors for pulse compression; FS slab, fused silica slab for fine dispersion compensation; SHG-FROG, second-harmonic frequency-resolved optical gating for characterization of compressed pulses, SP, spectrometer; CCD, CCD camera. (b) The group delay dispersion (GDD) of the GTI mirror.

In the first stage, the laser beam with a diameter of 1.6 mm (at the $1/e^2$ intensity level) was focused using the anti-reflection (AR)-coated lens L1 with

a focal length of $f = +150$ mm onto a 2 mm thick ZnS crystal. The crystal was tilted at a 50° angle with respect to the beam incidence in a compromise of minimizing the reflection losses (the calculated Brewster's angle was 66°), and at the same time, keeping the ellipticity of the beam, and thus, the peak intensity at an acceptable level to induce spectral broadening of the pulse [164, 165].

In the second stage, the beam was focused with an AR-coated lens L2 ($f = +100$ mm) onto the second nonlinear crystal (2 mm thick ZnS, 6 mm thick KGW or 15 mm thick YAG). Here, the second ZnS crystal was tilted at the same 50° angle with respect to the beam incidence, while the KGW and YAG crystals were placed at normal incidence due to their small transverse dimensions (5×5 mm²). The position of the lens L2 was found experimentally to achieve the desired dimensions of the beam waist and achieve the SPM-induced spectral broadening in a diverging beam, locating the samples ~ 5 mm behind the geometrical focus of the lens. Thereafter, AR-coated lens L3 ($f = +200$ mm) was used to collimate the output beam after the second stage of spectral broadening.

The spectrally broadened pulse was directed to the compression stage, which consisted of a pair of GTI mirrors (OPTOMAN) with 99.5% reflectivity per bounce and a group delay dispersion (GDD) of -1350 fs² at 1038 nm [Fig. 4.1 (b)]. A set of fused silica slabs of different thicknesses was used for the fine adjustment of the dispersion compensation.

A small part of the radiation, which was reflected from the 20% beam splitter BS and fused silica wedges W1 and W2, was sent for diagnostics. The beam profile measurements were performed using a 1600×1200 -pixel resolution CCD camera (Spiricon SP620U, Ophir Optronics). The spectral measurements were performed with a spectrometer (AvaSpec-ULS2048CL-EVO, Avantes), which, for the characterization of the spatial-spectral structure of the beam, was mounted on a motorized translation stage. The temporal characterization of the compressed pulses was performed with the homemade SHG-FROG setup, identical to the one presented in Chapter 3, and the SHG-FROG traces were retrieved using a standard pulse retrieval algorithm. The power measurements were performed with a thermal power sensor (F80(120)A-CM-17, Ophir Optronics, not shown in Fig. 4.1).

4.3 Characterization of spectral broadening

The spectral and spatial characteristics of the pulse after propagation through the first 2 mm thick ZnS crystal are shown in Fig. 4.2. The optimal position of the crystal was found at the geometrical focus of the L1 lens, where only a relatively small spectral broadening was achieved, see Fig. 4.2 (a) without causing any significant distortion of the beam shape compared to the input beam [Fig. 4.2 (b, c)].

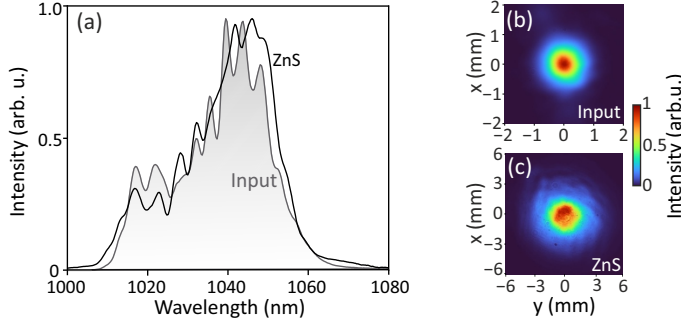


Fig. 4.2 (a) Comparison of the spectra of input pulses and laser pulses after the first stage of spectral broadening. Spatial profiles of the (b) input beam measured before the lens L1 and (c) collimated beam profile after propagation in ZnS.

Although only a relatively small spectral broadening was achieved, the first stage of spectral broadening in the ZnS crystal had a threefold effect. First, the combined action of the SPM and large material dispersion allowed for regularizing the spectral phase of the pulse, since the pulses after the PCMA carried a residual uncompensated (nonlinear) chirp [Fig. 3.5 (a-c) in Chapter 3]. Second, free space propagation between the spectral broadening stages suppressed small-scale irregularities in the beam due to nonlinear spatial effects. Third, the transverse dimensions of the sample $20 \times 20 \text{ mm}^2$ allowed for tilting of the crystal close to the Brewster's angle, thus minimizing the reflection losses. This was important for achieving sufficient intensity in the second stage of spectral broadening and, at the same time, avoiding using a very small diameter for the incident beam, bearing in mind that according to Marburger's law (Eq. 1.2), the beams with a smaller diameter self-focus and collapse at a shorter distance [60]. In what follows, the experimental settings described above were fixed. The measured average power of the output beam

was 14.2 W, suggesting high 90.5% transmission through the first stage of the spectral broadening.

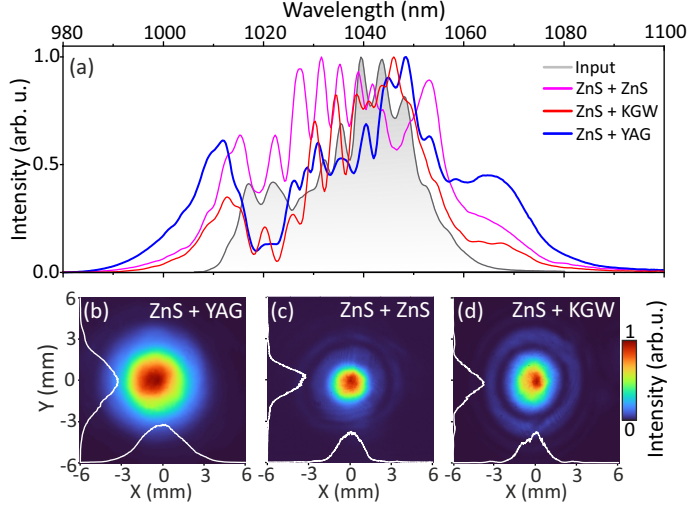


Fig. 4.3 (a) Spectra of the laser pulses after each stage of spectral broadening. The collimated beam profiles after propagation in combinations of (b) ZnS+YAG, (c) ZnS+ZnS and (d) ZnS+KGW.

In the second stage, the SPM-induced spectral broadening was performed in a diverging beam while locating the samples ~ 5 mm behind the geometrical focus of the lens L2. Such a propagation geometry was chosen by taking advantage of the fact that diverging beams are more resistant to self-focusing, thus helping to decouple the nonlinear effects in space and time, or in other words, to achieve spectral broadening, and at the same time, to minimize nonlinear spatial effects. The sample position with respect to the focal plane of the lens was found experimentally by simultaneously monitoring the beam profile and spectrum. The spectra of the laser pulses after each combination of nonlinear materials are presented in Fig. 4.3 (a), for comparison, the input spectrum is also shown by a grey curve. The corresponding collimated beam profiles are shown in Fig. 4.3 (b–d). The broadest pulse spectrum extending from 986 nm to 1100 nm (shown by a blue curve) without any apparent distortion of the beam profile was measured using a combination of 2 mm thick ZnS crystal in the first (fixed) stage and 15 mm thick YAG crystal in the second stage (this configuration is further referred to as ZnS+YAG). Such a spectrum was produced within a smooth, distortion-free Gaussian beam profile, as shown in Fig. 4.3 (b), attesting to no apparent onset of nonlinear spatial effects. Using

only a single YAG stage for single-pass spectral broadening under given experimental conditions was insufficient to achieve an appreciable broadening while maintaining a clean beam.

However, the two remaining configurations of nonlinear materials (ZnS+ZnS and ZnS+KGW) produced appreciable spectral broadenings only at the cost of deterioration of the output beam profile. More specifically, the spectrum extending from 990 nm to 1100 nm was measured after the ZnS+ZnS configuration, as shown by the magenta curve. Here, the second 2 mm thick ZnS crystal produced somewhat larger spectral broadening as a result of a smaller beam diameter (note that L2 has a shorter focal length), and thus, a larger input intensity. Although the spectral broadening was smaller compared with the ZnS+YAG case, the beam profile measurement shown in Fig. 4.3 (c) revealed an already distorted beam with a characteristic low-intensity ring, which is a clear signature self-focusing. The configuration of 2 mm thick ZnS and 6 mm thick KGW crystals (ZnS+KGW) led to similar observations: a slightly narrower spectrum that extended from 994 nm to 1088 nm (red curve) and an output beam with pronounced ring structure, as illustrated in Fig. 4.3 (d).

4.4 Temporal characterization of post-compressed pulses

The temporal characterization of the pulses after the first ZnS crystal was performed using SHG-FROG home-built setup. The measured and reconstructed SHG-FROG traces are shown in Figs. 4.4 (a) and 4.4 (b), respectively, with a rms reconstruction error of 0.19%. The measured and reconstructed spectra are compared in Fig. 4.4 (c) and retrieved temporal profile of the pulse is shown in Fig. 4.4 (d). The retrieved pulse width of 103 fs indicates temporal broadening of the pulse due to large GVD of ZnS ($385 \text{ fs}^2/\text{mm}$ [162]), while its spectrum corresponded to the transform-limited (TL) duration of ~ 50 fs, which was obtained by a zero-phase Fourier transform of the measured spectrum.

The compressibility of spectrally broadened pulses was examined for all combinations, with a particular focus on the ZnS+YAG combination, whose overall performance was analyzed in greater detail. In the ZnS+YAG case, the pulse compression was performed using three reflections from the GTI mirrors with an additional passage through the 18 mm thick fused silica slab for the fine matching of the GDD. The measured SHG-FROG trace and the reconstructed trace with a retrieval rms error of 0.13% are shown in Fig. 4.5 (a). Figure

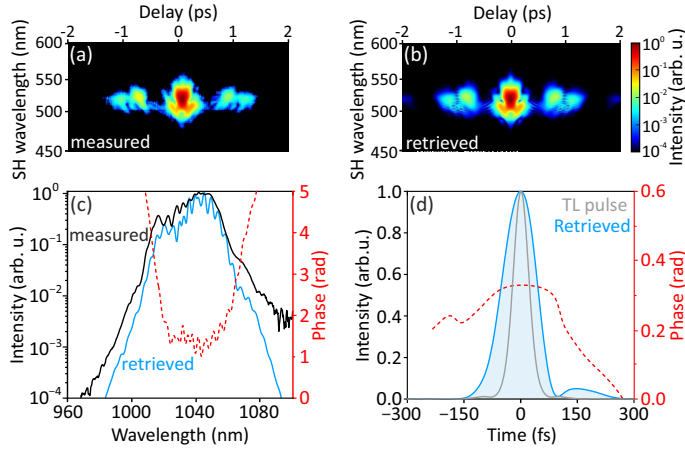


Fig. 4.4 SHG-FROG characterization of the pulse after propagation in the first 2 mm thick ZnS crystal: The (a) measured and (b) retrieved SHG-FROG traces (SHG-FROG reconstruction error of 0.19%), (c) measured (black) and retrieved (blue) spectra, and retrieved spectral phase (red), (d) retrieved temporal profile (blue) and temporal phase (red). The temporal profile of the TL pulse is represented by the grey curve.

4.5 (b) compares the measured and reconstructed spectra, showing an excellent agreement of spectral profiles over four orders of magnitude. The retrieved temporal profile of the compressed pulse is presented in Fig. 4.5 (c), yielding pulse duration of 37 fs, which is close to the TL pulse duration of 32 fs. The satellite post-pulses were likely due to a large GDD imposed by the GTI mirrors, whose operation range did not cover the full bandwidth of the broadened pulse spectrum and residual third-order dispersion [Fig. 4.1 (b)]. Nevertheless, it was estimated that 85% of the pulse energy was contained in the main peak.

The measured average power at the output of the entire setup using ZnS+YAG combination was 11.47 W, indicating an energy throughput of 73%. It is important to notice that the overall 27% energy losses were of solely linear character, as introduced by Fresnel reflections in the uncoated ZnS sample (9.5%) and uncoated YAG sample at normal incidence (16.5%), and 1.5% energy losses after three reflections from the GTI mirrors, suggesting the absence of any detectable nonlinear energy losses in the samples due to multiphoton absorption, ionization, etc. Assuming these energy losses, the estimated peak power of the post-compressed pulses was 3.26 MW.

The performances of the ZnS+ZnS and ZnS+KGW configurations were characterized as well, see Figs. 4.5 (d-f) and Figs. 4.5 (g-i), respectively. The ZnS+ZnS configuration yielded the highest energy throughput of 80% due to the

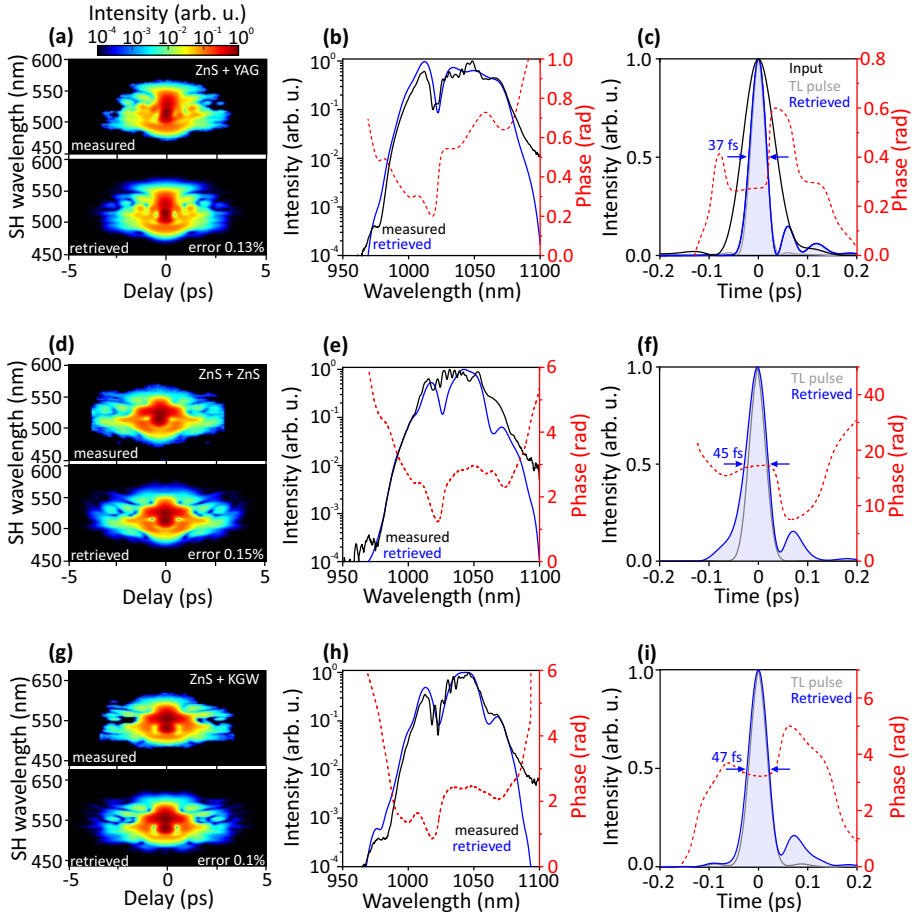


Fig. 4.5 Characterization of the post-compressed pulses of (a-c) ZnS+YAG, (d-f) ZnS+ZnS and (g-i) ZnS+KGW configuration. (a, d, g) The measured and retrieved SHG-FROG traces (SHG-FROG reconstruction errors of 0.13%, 0.15%, 0.1%, respectively), (b, e, h) measured (black) and retrieved (blue) spectral intensities, and retrieved spectral phase (red), (c, f, i) retrieved temporal profile (blue) and temporal phase (red). The temporal profiles of TL and input pulses are shown for comparison by grey and black curves, respectively.

minimized reflection losses, but on the other hand, resulted in the longest 47 fs pulses after compression (three reflections from the GTI mirrors), which was 1.27 times larger compared to the 37 fs long TL pulse, in part due to improper fine dispersion compensation and a non-uniform spatial profile [Fig. 4.5 (f)]. Similar observations were made in the ZnS+KGW configuration, with measured spectrum corresponding to TL pulses of 39 fs and retrieved 45 fs long pulses after compression which was performed using four reflections from the GTI mirrors with additional passage through the 52 mm fused silica slab [Fig. 4.5 (i)],

Table 4.1 Relevant post-compression parameters achieved with the examined combinations of nonlinear materials. P_{out} is the average output power of the post-compressed pulses, T is the energy throughput of the setup, τ_{TL} is the duration of the transform-limited pulse, τ_{exp} is the measured duration of the post-compressed pulse and P_{peak} is the peak power.

Nonlinear material	P_{out} , W	T , %	τ_{TL} , fs	τ_{exp} , fs	P_{peak} , MW
ZnS + ZnS	12.53	80	37	47	2.67
ZnS + KGW	10.70	68	39	45	2.41
ZnS + YAG	11.47	73	32	37	3.26

which also provided the lowest transmission due to the highest reflection losses from the uncoated KGW crystal at normal incidence.

A brief summary and comparison of the relevant post-compression parameters achieved with the examined combinations of nonlinear materials is presented in Table 4.1. In order to explain these results, first, the critical power for self-focusing (Eq. 1.1) $P_{cr} = 0.10$ MW in ZnS, $P_{cr} = 0.72$ MW in KGW and $P_{cr} = 1.42$ MW in YAG was calculated, taking the n_0 and n_2 values of ZnS provided in section 4.2 and the n_0 and n_2 values of KGW and YAG provided in Table 2.1. Next, the peak power of the pulse entering the second stage of the spectral broadening was evaluated by taking into account the measured pulse duration and transmission after the first stage of the spectral broadening (only the 2 mm thick ZnS sample) and the reflection from the front face of the nonlinear material. In the case of YAG, the estimated peak power of the incident pulse was 1.69 MW, which is slightly above the critical power for self-focusing ($1.19 P_{cr}$). In contrast, similar calculations yielded the incident pulse peak powers of $2.28 P_{cr}$ and $17.5 P_{cr}$ entering the KGW and ZnS crystals, respectively, attesting that it was more difficult to avoid the onset of self-focusing in these crystals under the present experimental settings. The best result in YAG is in line with the numerical and experimental findings presented in [148], which demonstrated that the optimal condition for single-pass spectral broadening is when the peak power of the input pulse is only slightly above the critical power for self-focusing in a given material and showed that the focusing geometry in the single-pass scheme does not improve the efficiency of the approach.

4.5 Evaluation of spatial-spectral homogeneity

A more detailed characterization of spectrally broadened pulses was carried out by evaluating the spatial-spectral homogeneity of the beam. This is an important characteristic, as SPM-induced spectral broadening in a simple single-pass geometry typically leads to an inhomogeneous distribution of spectral components across the beam profile, and therefore, to different compression factors at the beam center and periphery [143]. The spatial-spectral structure of the beam was characterized at each stage of the presented broadening setup by scanning the spectra along the x -coordinate with a spectrometer mounted on a motorized translation stage. For a quantitative evaluation, the spectral overlap parameter (V) was calculated, which represents the overlap of each off-axis spectra with the spectrum on the beam axis, as defined in [143]:

$$V = \frac{[\int (I(\lambda) \cdot I_0(\lambda))^{\frac{1}{2}} d\lambda]^2}{[\int I(\lambda) d\lambda \cdot \int I_0(\lambda) d\lambda]}, \quad (4.1)$$

where $I(\lambda)$ is the spectrum at a given x -coordinate, $I_0(\lambda)$ is the spectrum on the beam axis ($x = 0$). The spectral overlap parameter is a measure of spatiotemporal quality, indicating how homogeneous the spectral broadening is across the beam profile, and so how homogeneous the pulse duration will be after compression. Also the effective overlap V_{eff} (effective homogeneity within the $1/e^2$ beam intensity level) was calculated by weighting the spectral overlap V with the intensity across the beam, as defined in [143, 166]:

$$V_{\text{eff}}(\%) = \frac{\int V(x)I(x)xdx}{\int I(x)xdx}, \quad (4.2)$$

where $V(x)$ is the spectral overlap at a given x -coordinate and $I(x)$ is the intensity distribution over the beam profile at a given x -coordinate x .

The measurements confirmed the high ($V > 85\%$ from $1/e^2$ intensity level and $V_{\text{eff}} = 97\%$) homogeneity of the beam after propagation in the first ZnS crystal, which was as expected (given the slight broadening of the spectrum) close to that of the input beam ($V > 90\%$, $V_{\text{eff}} \approx 100\%$). The measured spatial-spectral intensity map of the beam after the ZnS+YAG broadening and the compression stage [Fig. 4.6 (a)] and the spectra along the x -coordinate selected at 10%, 13.5%, 50% and 100% beam intensity levels [Fig. 4.6 (c)] are both showing an almost constant spectral width across the beam profile, which justi-

fies a homogeneous spectral distribution as a function of the coordinate. Figure 4.6 (b) shows the spectral overlap $V > 83\%$ across a major part of the beam, where dotted grey lines indicate the beam intensity level of $1/e^2$. The intensity distribution across the beam (orange curve) was obtained as it was described in section 4.3. The estimated energy contained in the beam $V > 90\%$ was 88.4%, corresponding to 10.14 W of average power. Although these measurements were not repeated by turning the beam 90° , almost identical spatial-spectral couplings along the y -coordinate are expected given the symmetry of the beam profile [Fig. 4.3 (b)].

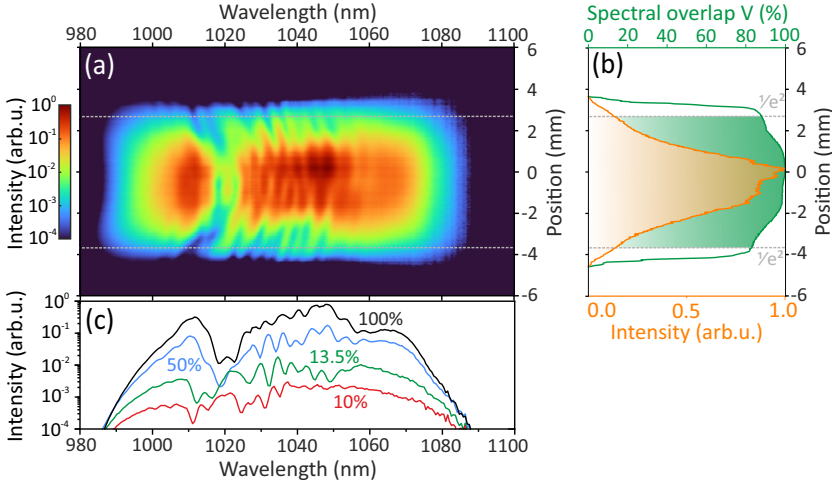


Fig. 4.6 Spatial-spectral characterization of the compressed pulses. (a) Spatial-spectral homogeneity map of the output beam along the x -axis. (b) Spectral overlap parameter V (green curve) and intensity distribution over the beam profile (orange curve). Green shading denotes the area within which the beam intensity is $> 1/e^2$, as indicated by dotted grey lines. (c) Spectra selected at different beam intensity levels.

4.6 Beam quality measurements

Finally, the spatial beam quality of the post-compressed pulses was investigated by the evaluation of beam propagation factor M^2 . In doing so, a focusing lens with $f = +300$ mm was used to focus the collimated beam after the compressor. The beam profile was recorded using a high-resolution (2048×1536 pixel) CMOS camera (SP932U, Ophir Optronics), which was translated along the focal zone. Figure 4.7 shows the results of the beam quality measurement in the x - and y -coordinates. The insets show the beam profiles recorded in the far

fields and at the focal plane (beam waist). The dimensions of the focal spot were $w_x = 94 \mu\text{m}$ and $w_y = 87 \mu\text{m}$, as evaluated at the $1/e^2$ intensity level, and were close to the calculated spot diameter of an ideal (diffraction-limited) Gaussian beam ($w_0 = 78 \mu\text{m}$), whereas a slight ellipticity originated from the incident amplified oscillator beam. The divergence angles of the beam in the x - and y -directions ($\theta_x = 18.0 \text{ mrad}$ and $\theta_y = 17.4 \text{ mrad}$) were evaluated from linear fits of the slopes in the far field. The computed $M_x^2 = 1.28$ and $M_y^2 = 1.14$ attested to the good spatial quality of the post-compressed pulses, which was only slightly worse than that of an amplified input beam with $M_x^2 = 1.18$ and $M_y^2 = 1.11$ [130].

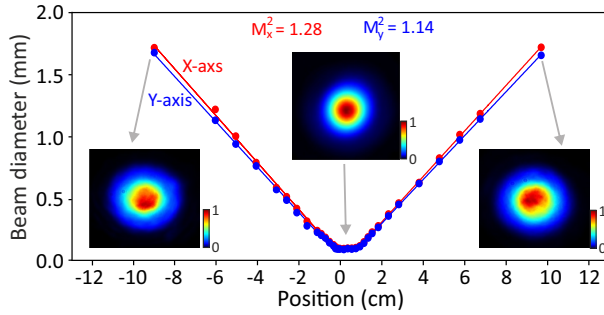


Fig. 4.7 Beam quality measurement. Solid curves represent a linear fit of the slopes in the far field. The inset shows far field beam profiles and the beam profile at the beam waist.

4.7 Summary and outlook

To summarize this Chapter, a proof-of-principle of a simple all-solid-state post-compression setup for low-energy laser pulses was demonstrated. The spectral broadening of 75 fs, 210 nJ pulses from an amplified 76 MHz, 15.7 W Yb:KGW oscillator was performed using several combinations of highly nonlinear bulk materials, namely ZnS, YAG and KGW, in a single-pass geometry. Among the tested configurations, the broadest spectrum without beam deterioration due to the onset of self-focusing was produced by sequential propagation in ZnS and YAG samples of 2 mm and 15 mm thickness, respectively. The spectrally broadened pulses were compressed to 37 fs by means of GTI mirrors, which is close to the estimated Fourier transform limit (32 fs). The spatial-spectral characterization of post-compressed pulses with an average power of 11.47 W

attested to the almost uniform spectral distribution across the beam (the spectral overlap parameter $V > 83\%$) and good beam quality ($M^2 = 1.28 \times 1.14$). It should be noted that the energy throughput of the overall post-compression setup could be improved significantly by minimizing the reflection losses using AR-coated samples of nonlinear materials. On the other hand, larger spectral broadening, as well as larger compression factors, could be achieved using multi-pass geometries [148] or exploiting self-defocusing nonlinearities due to second-order cascading via phase-mismatched second-harmonic generation in materials with $\chi^{(2)}$ nonlinearity [147], where the sign and magnitude of an effective nonlinear index of refraction could be suitably tuned by varying the phase mismatch between the interacting waves.

The results presented in this Chapter are of practical importance, suggesting that spectral broadening in highly nonlinear bulk materials could be an attractive alternative to fiber-based spectral broadening, offering virtually alignment-insensitive, low-complexity and low-cost all-solid-state arrangement for post-compression of low-energy pulses at high laser pulse repetition rates.

Chapter 5

Supercontinuum generation with bursts of femtosecond laser pulses

Material related to this chapter was published in [A3]

5.1 Motivation

Burst trains of femtosecond laser pulses emerge as a powerful tool for laser material processing, offering a variety of technological innovations in micro-machining (ablation, marking, cutting and welding, drilling, polishing, etc.) of metals [167], glasses [48, 168], semiconductors [169], polymers [170] and biomaterials [171]. Burst-mode two-photon polymerization was considered to deliver microstructures with smaller feature size [172], while irradiation of solid targets with femtosecond pulse bursts was demonstrated to significantly increase of the hard X-ray yield [173]. For what concerns laser wavelength conversion processes, generation of second and fourth harmonics with femtosecond pulse bursts was demonstrated [174]. Burst-mode pumping was shown beneficial for increasing the pump-to-idler conversion efficiency in long-picosecond mid-infrared optical parametric oscillator [175]. In the femtosecond regime, burst-mode operation allowed average power scaling of femtosecond optical parametric oscillators [176, 177] and amplifiers [178, 179], as well as OPCPA [180, 181] and spectral broadening-based extracavity post-compression schemes [182, 183], which deliver few optical cycle pulses.

Despite the rapid development and commercial availability of burst-mode laser systems, only a few studies have investigated filamentation phenomena in

transparent materials using femtosecond pulse bursts. Burst-mode filamentation in atmospheric air enabled control and tailoring of filamentation dynamics [184] and production of extended conductive channels via filament stitching [185], which are important for long-distance applications. Time-resolved dynamics of burst-mode filamentation-assisted micromachining of glasses revealed build-up of heat accumulation [186], brighter and longer-lasting filament luminescence tracks [48], demonstrating stronger laser-matter interaction and more prominent morphological changes of the solid-state material compared to a single-pulse exposure.

In contrast to laser material processing-oriented applications, burst-mode SC generation requires robust, durable and modification-free performance of the nonlinear material. However, so far, burst-mode SC generation for seeding an OPA was demonstrated at relatively low (188 kHz) intra-burst repetition rate [178], and to the best of the author's knowledge, burst-mode SC generation in bulk solid-state materials with high (tens of MHz to a few GHz) intra-burst repetition rates was not studied so far.

In this Chapter, an experimental and numerical investigation of burst-mode filamentation and SC generation in sapphire crystal using bursts consisting of two pulses is presented. It is demonstrated that residual material excitations alter the filamentation and SC generation dynamics of subsequent pulses, justified by numerical simulations that revealed free electron plasma and self-trapped excitons (STEs) remaining after the propagation of the preceding pulse.

5.2 Experimental methods and results

The experiments were performed with 190 fs (FWHM), 1030 nm pulses from an amplified 80 W Yb:KGW laser (Carbide, Light Conversion Ltd.). The laser operated at 1 MHz repetition rate in either single-pulse or burst-mode, with a time delay between adjacent pulses of 16 ns and 400 ps, corresponding to intra-burst repetition rates of 62.5 MHz and 2.5 GHz, respectively. The laser enabled operation with an adjustable number of pulses per burst (from 2 to 10) and tunable energy distribution of the pulses within the burst. For the sake of simplicity, two pulses with equal energies per burst were used, which allowed to clearly observe experimentally and reproduce numerically the relevant burst-induced effects on beam filamentation and SC generation. In all other regimes with a higher number of pulses per burst, the pulse energies

varied across the pulse train, setting complicated operating conditions, which were not considered in the present study.

A typical SC generation geometry was used (similar to the one described in Chapter 2), where the input beam with a diameter of 4.6 mm (at the $1/e^2$ intensity level) was focused with a fused silica lens ($f = +100$ mm) onto the front face of uncoated and undoped 5-mm-long sapphire sample (EKSMA Optics). Among the wide range of transparent solid-state materials, sapphire crystal stands out as one of the most extensively studied. Its key properties are well-characterized, particularly with regard to transient excitation lifetimes and carrier dynamics. The spectral measurements were performed by coupling the axial part of the output radiation into a slit of spectrometer (AvaSpec-3648, Avantes) with a detection range from 200 to 1100 nm, measuring the blue-shifted portion of SC spectra.

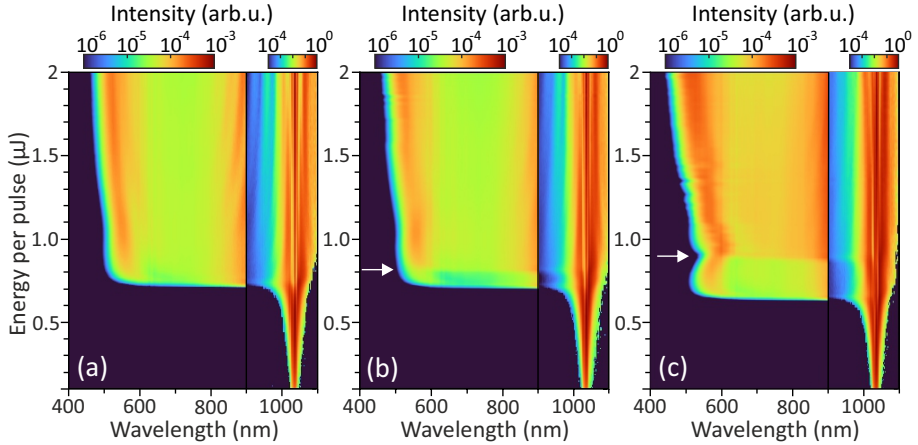


Fig. 5.1 The dynamics of spectral broadening in sapphire versus the pump pulse energy measured in (a) single-pulse mode and in burst-mode containing two identical pulses per burst with the second pulse delayed by (b) 16 ns, (c) 400 ps. Note different intensity scales in the wavelength ranges of 400 - 900 nm and 900 - 1100 nm, which were used for a better visibility of relevant spectral features. The arrows in (b) and (c) mark the threshold energies for the SC generation by the second pulse in the burst.

First of all, the spectral measurements were performed with a single pump pulse at 1 MHz laser repetition rate, which served as a reference for the burst-mode measurements. The measured dynamics of spectral broadening in a single-pulse mode is presented in Fig. 5.1 (a), showing an explosive broadening of the spectrum at the pump pulse energy of 710 nJ ($1.09 P_{cr}$, assuming critical power for self-focusing in sapphire $P_{cr} = 3.25$ MW, see Table 2.1), which

was defined as the threshold energy for SC generation. No significant spectral changes were observed with further increase of the pump pulse energy, showing fairly constant cut-off at ~ 500 nm and smooth spectral shape, thus indicating no filament refocusing and related modulation of the spectrum for a relatively wide range of the pump pulse energies. Figure 5.1 (b) shows the dynamics of spectral broadening measured in the burst-mode, containing two identical pulses per burst with the second pulse delayed by 16 ns. An explosive spectral broadening is observed with the same energy of the pump pulse (here evaluated as an energy per pulse) as in the above case. However, in the present case, the SC is generated only by the first pulse, while a slightly higher energy (800 nJ, $1.2 P_{cr}$) is required to produce SC by both pulses in the burst, as justified by an abrupt twofold increase of the SC spectral intensity and indicated by the arrow in the Fig. 5.1 (b). Even more distinctive picture of step-wise SC generation dynamics was recorded in the burst-mode with the second pulse delayed by 400 ps, as illustrated in Fig. 5.1 (c). Firstly, the measured spectral dynamics revealed a slightly lower (650 nJ, $\sim P_{cr}$) threshold energy for SC generation with the first pulse in the burst, which is attributed to the possible influence of thermal effects due to high (1 MHz) repetition rate of the laser, locally affecting the condition of beam focusing. Secondly, the pump pulse energy has to be increased considerably, up to 900 nJ ($1.38 P_{cr}$), to observe the SC generation by both pulses in the burst, as indicated in Fig. 5.1 (c).

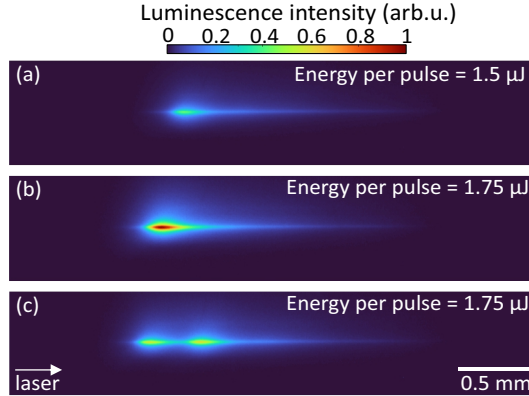


Fig. 5.2 Filament-induced luminescence track in sapphire crystal measured in (a) single-pulse mode with 1 MHz repetition rate and in burst-mode containing two identical pulses per burst with the second pulse delayed by (b) 16 ns, (c) 400 ps. The arrow indicates the beam propagation direction.

Figure 5.2 presents the complementary measurements of filament-induced luminescence traces captured from the polished side of the crystal in the single pulse and burst mode. In the present case, the energy of the pulse in a single-pulse mode was $1.5 \mu\text{J}$, while the energy per pulse in the burst mode was $1.75 \mu\text{J}$, so both pulses in the burst produce SC. These measurements were performed by imaging the area around the nonlinear focus onto the CCD camera (Grasshopper2, Point Grey) with a pixel size of $4.4 \mu\text{m}$ and using an appropriate colour filter transmitting in the UV.

Figure 5.2 (a) shows the filament-induced luminescence trace produced in a single pulse mode (the pulse's energy of $1.5 \mu\text{J}$), where the most intense part of the trace indicates the beginning of the light filament (the position of the nonlinear focus). A twice brighter luminescence trace of a similar shape was recorded with a two-pulse burst with the second pulse delayed by 16 ns , attesting that the nonlinear foci of both pulses overlap, as shown in Fig. 5.2 (b). Note that in this case the energy per pulse was slightly higher ($1.75 \mu\text{J}$), resulting in a slight shift of the luminescence trace position toward the front face of the crystal. Figure 5.2 (c) presents the luminescence trace induced by two-pulse burst with the second pulse delayed by 400 ps , showing two distinct well-separated luminescence peaks. The first (leftmost) peak corresponds to the nonlinear focus of the first pulse, while the second (rightmost) peak corresponds to the nonlinear focus of the second pulse in the burst, suggesting that the second pulse self-focuses at a larger propagation distance (note the arrow indicating the direction of beam propagation). This observation clearly indicates more difficult filamentation conditions for the second pulse, which is delayed by 400 ps , and is in line with spectral measurements.

5.3 Numerical simulations of free electron plasma, STEs and nonlinear losses

In order to explain the experimental observations and to better understand the fundamental processes behind burst-mode filamentation and SC generation, a numerical model which accounted for diffraction, dispersion, optical Kerr effect, and free electron plasma generation, resulting from multiphoton absorption and avalanche ionization, was developed [187]. The model enabled a detailed analysis of light-matter interaction considering the propagation of several con-

secutive laser pulses with an account for material response. The formation of transient states within the band gap, such as self-trapped excitons (STEs) and the residual excitations (free electron plasma and STEs) remaining after the propagation of preceding pulse, was also considered (see Appendix).

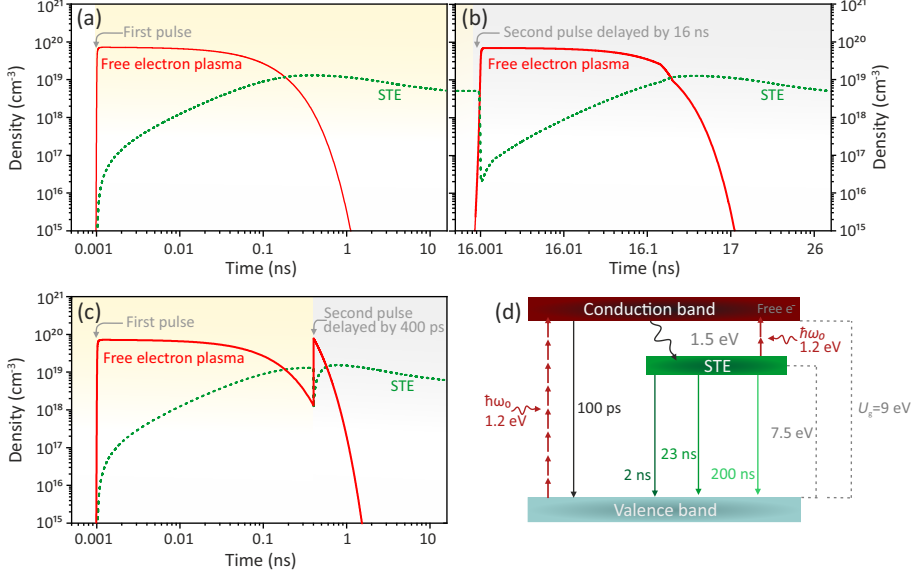


Fig. 5.3 Free electron (e^-) plasma (solid red curves) and STE (dashed green curves) dynamics after passage of (a) first pulse, (b) second pulse delayed by 16 ns, (c) second pulse delayed by 400 ps. The pulse energy in all the cases is 0.83 μJ . (d) simplified diagram of excitation and relaxation pathways in sapphire.

Figure 5.3 presents the simulated dynamics of free electron plasma and STE densities in the beam center at a fixed propagation distance, $z = 2.06$ mm, which corresponds to the position of nonlinear focus of the first pulse, and which slightly varied for the second pulse due to presence of residual free electrons and STEs, which locally induce negative and positive contributions to the refractive index, respectively. Figure 5.3 (a) shows the time evolutions of free electron plasma and STE densities induced by the propagation of the first laser pulse with an energy of 0.83 μJ ($1.26P_{cr}$), that is slightly above the experimentally established threshold energy for SC generation (0.71 μJ).

The free electron plasma due to transitions from valence to conduction band, in this case eight-photon absorption, assuming the bandgap of sapphire $U_g = 9$ eV (Table 2.1) and the photon energy of the incident laser pulse of 1.2 eV (the laser wavelength 1030 nm), rises rapidly within the time interval approximately equal to pulse duration. The free electron plasma reaches the maximum

density of $7.2 \times 10^{-19} \text{ cm}^{-3}$ and then decays via radiative (fluorescence) and nonradiative (excitation of phonons and formation of STEs within the band gap with recombination and binding energies of 7.5 eV and 1.5 eV [188–190]) processes with decay time constant of $\tau_{re} = 100 \text{ ps}$ [191]. The build-up time of STEs was taken equivalent to the relaxation time of electrons in the conduction band. The density of STEs reaches its peak value of $1.1 \times 10^{-19} \text{ cm}^{-3}$ at $\sim 380 \text{ ps}$ after passage of the laser pulse. The STE included three sub-states which decay with characteristic relaxation times of 2 ns, 23 ns and 200 ns [189, 190]. The population of the first STE sub-state was taken $\sim 40\%$ according to [188], while the populations of the remaining two sub-states were not known and in the present model were taken to be equal. Therefore, the resulting STE population distributions within the sub-states corresponding to these decay constants were taken as 2:1:1, respectively. A simplified diagram of excitation and relaxation pathways in sapphire is illustrated in Fig. 5.3 (d).

Figure 5.3 (b) shows the simulated dynamics of free electron plasma and STE densities after passage of the second pulse in the burst, which is delayed by 16 ns (note a different timescale of a graph). In fact, the second pulse finds only a negligible residual concentration of free electrons, but still a notable residual density of STEs ($5.4 \times 10^{-18} \text{ cm}^{-3}$). At the moment of the second pulse arrival, there is an abrupt drop of STE density due to optically-induced dissociation of STEs via two-photon absorption, contributing to a slightly higher density ($8.4 \times 10^{-19} \text{ cm}^{-3}$) of free electron plasma in the wake of the second pulse. Thereafter, the dynamics of STE density follows essentially the same trend as in the case of the first pulse.

Figure 5.3 (c) shows the simulated dynamics of free electron plasma and STE densities after passage of the second pulse in the burst, which is delayed by 400 ps. In this case, the second pulse encounters a material with still appreciable concentrations of both, free electrons and STEs ($1.3 \times 10^{-18} \text{ cm}^{-3}$ and $1.3 \times 10^{-19} \text{ cm}^{-3}$, respectively). The combined effect of residual free electrons that provide initial population for faster onset of avalanche ionization and optically-induced dissociation of residual STEs yields a maximum plasma density of $9.1 \times 10^{-19} \text{ cm}^{-3}$, which is larger by almost 30% than the plasma density produced by the first pulse. Also note an abrupt drop of STEs density due to optically-induced dissociation that is followed by the build-up of STE states as free electron plasma decays, reaching the maximum density of $1.5 \times 10^{-19} \text{ cm}^{-3}$. The free electron plasma and STEs dynamics in the case of pulses with higher

energy, $1.28 \mu\text{J}$ ($\sim 2P_{cr}$), where SC generation by both pulses in the burst regardless of their temporal separation was observed experimentally, are not shown since they follow essentially identical trends, as illustrated in Figs. 5.3 (a-c).

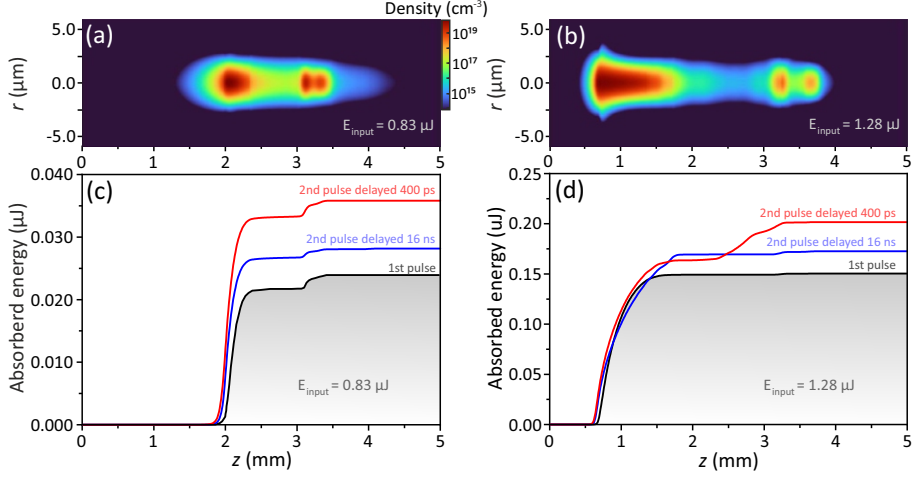


Fig. 5.4 (a), (b) r radial distributions of free electron plasma along the beam propagation path produced by nonlinear propagation of the first pulse with energies of $0.83 \mu\text{J}$ and $1.28 \mu\text{J}$, respectively. Nonlinear energy losses (absorbed energy in sapphire crystal) as a function of propagation distance z of first (1st) pulse, second (2nd) pulse delayed by 16 ns, 2nd pulse delayed by 400 ps with pulse energies of (c) $0.83 \mu\text{J}$ and (d) $1.28 \mu\text{J}$.

Figures 5.4 (a) and (b) compares the calculated radial distributions of free electron plasma densities along the beam propagation path induced by the propagation of the first laser pulse with energies of $0.83 \mu\text{J}$ and $1.28 \mu\text{J}$. The radial distributions of free electron plasma densities for the second pulse, which is delayed by 16 ns and 400 ps and energies of $0.83 \mu\text{J}$ and $1.28 \mu\text{J}$, are not shown since these distributions exhibit nearly identical trends. This is also expected for the radial distributions of STE densities. However, the main differences occur in the longitudinal (i.e. along the beam propagation path $r = 0 \mu\text{m}$) distributions of the free electron plasma, which drive the nonlinear propagation dynamics of the pulse.

The absolute values of absorbed energy as a function of propagation distance were calculated and are presented in Figs. 5.4 (c and d) revealing significant differences in nonlinear losses for the first and second pulses in the burst. In the case of $0.83 \mu\text{J}$ input pulse energy, absorbed energy and energy losses were 24 nJ (2.9%), 28 nJ (3.4%) and 36 nJ (4.3%) for the first pulse, the second pulse

delayed by 16 ns and 400 ps, respectively. For an input pulse energy of 1.28 μJ , the absorbed energy and energy losses increased to 150 nJ (12%), 173 nJ (13.5%) and 202 nJ (15.5%), respectively. These numbers illustrate that the second pulse delayed by 400 ps always experiences the largest nonlinear losses, however the nonlinear dynamics of the second pulse in the burst is affected not only by the energy losses due to nonlinear absorption but also by plasma defocusing, which does not introduce energy losses, but affects the propagation dynamics in spatial and temporal domains via spatiotemporal reshaping of the pulse. This is especially true for longer (several 100s of fs) input pulses.

5.4 Numerical simulations of temporal and spectral dynamics

To start with, the nonlinear propagation of the first laser pulse, with an energy of 0.83 μJ in an unaltered sapphire crystal was numerically simulated. The axial (at the center of the beam $r = 0 \mu\text{m}$) distribution of free electron plasma and the maximum achievable intensity across the beam profile are plotted as functions of the propagation distance through the sapphire crystal [Fig. 5.5 (a)]. Temporal and spectral dynamics at the center of the beam versus the propagation distance z are shown in Figs. 5.5 (d and g), respectively. Free electron plasma produced by the leading front of the driving pulse (see the plasma density peak and the first sharp increase in peak intensity at $z \approx 2.1 \text{ mm}$ in Fig. 5.5 (a), which denotes the nonlinear focus of the beam, efficiently absorbs and defocuses the rear part (the descending front) of the pulse [Fig. 5.5 (d)]. As a result, the pulse at the beam center experiences a considerable reduction of its temporal width and its intensity peak shifts toward the forefront of the pulse. Such plasma-induced pulse shortening does not produce SC and results only in moderate spectral broadening beyond the nonlinear focus, as illustrated in Fig. 5.5 (g). Meanwhile, with further propagation, the pulse at the beam center replenishes [67]. The replenishment position along the propagation axis z is defined by the peak density and geometry (width and length) of the plasma channel. A short replenished pulse self-focuses at $z \approx 3.1 \text{ mm}$, where a sharp increase in intensity and corresponding plasma peaks are visible in Fig. 5.5 (a). This replenished pulse experiences pulse splitting and dramatic self-steepening of the trailing sub-pulse at $z \approx 3.3 \text{ mm}$, as illustrated in Fig. 5.6 (a), that results in

SC generation in accordance to general SC generation scenario [3], as justified by the corresponding spectral dynamics shown in Fig. 5.5 (g). For further clarity, the SC spectrum at $z \approx 3.3$ mm is also presented in Fig. 5.6 (b). The regular spectral fringes, which are particularly distinct on the long wavelength side, appear due to the interference between plasma-shortened and spectrally broadened pulse at the forefront and SC-producing split sub-pulses.

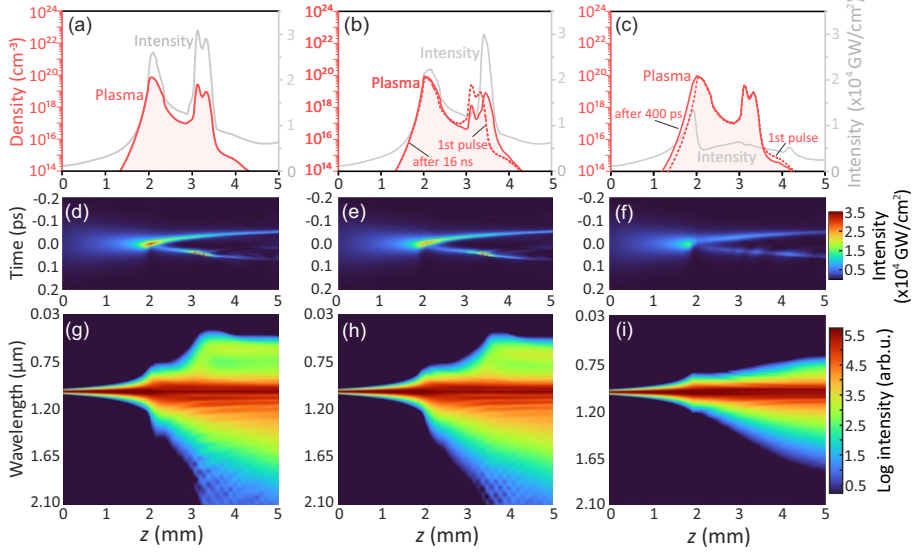


Fig. 5.5 Axial (at the center of the beam) distributions of free electron plasma (red curve) and the maximum achieved intensity (grey curve) along the beam propagation path produced by nonlinear propagation of the (a) first laser pulse in an unaltered sapphire crystal and identical second pulse which is delayed by (b) 16 ns and (c) 400 ps with energies of 0.83 μJ . (d-f) display the corresponding temporal dynamics, where negative time represents the leading front of the pulse. (g-i) display the corresponding spectral dynamics and z denotes the propagation distance.

Figure 5.5 (e) shows the temporal dynamics of the second laser pulse delayed by 16 ns, which finds slightly altered nonlinear material featuring a notable density of STEs generated by the propagation of the first pulse, see Fig. 5.3 (b). In this case, the second pulse exhibits a similar maximum intensity and free electron plasma distribution as the first pulse [Fig. 5.5 (b)] and has only a minor effect on the second pulse propagation, which undergoes almost identical spatio-temporal transformations. However, at $z \approx 3.3$ mm, the rear part of the pulse has a lower intensity and a narrower pulse spectrum compared to the first pulse in the unaltered material [Fig. 5.6 (a, b)]. Splitting of the replenished pulse and SC generation occurs at a slightly longer ($z \approx 3.5$ mm)

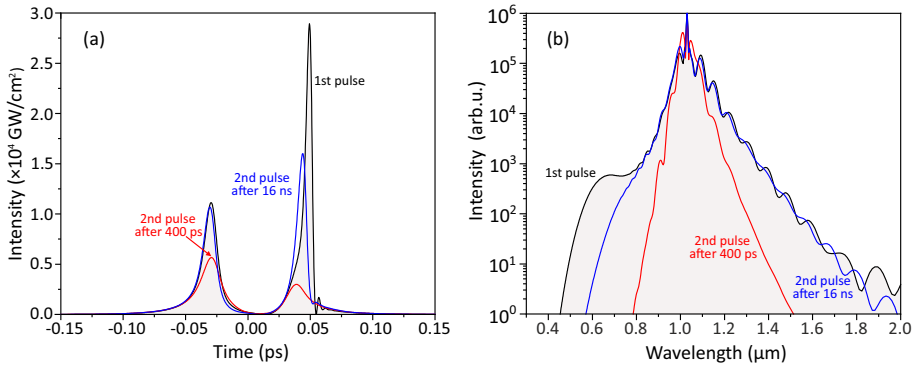


Fig. 5.6 (a) Intensities of the first and second pulses which are delayed by 16 ns and 400 ps with energies of 0.83 μ J and (b) corresponding spectra at the center of the beam at $z = 3.3$ mm.

propagation distance, see Fig. 5.5 (e, h). This may explain the experimental evidence [Fig. 5.1 (b)] why a slightly higher energy of the second pulse, delayed by 16 ns, is required for SC generation to occur.

A different picture emerges when the second laser pulse is delayed by 400 ps. In this case, the second pulse encounters a material with still considerable densities of both free electron plasma and STEs, as shown in Fig. 5.3 (c). As a result, the pulse experiences additional energy losses due to plasma and STE absorption [see Fig. 5.4 (c)] and stronger plasma defocusing due to its larger density. Although its temporal dynamics visually follow the initial stage of plasma-induced pulse reshaping as described above, the replenished pulse never acquires enough power to self-focus, as illustrated in Fig. 5.5 (f). Additionally, no significant increase in maximum intensity was observed, as shown in Fig. 5.5 (c). Consequently, no self-focusing and splitting of the replenished pulse occurs and no SC is produced at $z \approx 3.3$ mm or with further propagation [Fig. 5.6 (a, b)]. Only gradual spectral broadening that is limited to the near-infrared range takes place due to continuous plasma-induced pulse reshaping, as shown in Fig. 5.5 (i).

Numerical simulations of the temporal and spectral dynamics for higher energy (1.28 μ J) input pulses were also performed. The axial distribution of free electron plasma and the maximum intensity along the beam propagation path is presented in Fig. 5.7 (a-c). It should be noted that the difference of maximum achievable free electron plasma densities with lower and higher input energy pulses is small due to the intensity clamping effect. The temporal

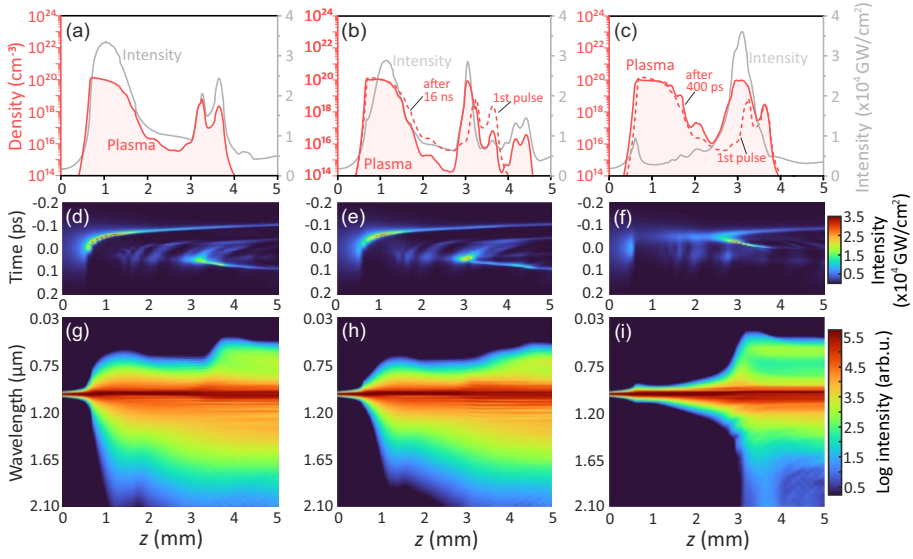


Fig. 5.7 Axial (at the center of the beam) distributions of free electron plasma (red curve) and the maximum achieved intensity (grey curve) along the beam propagation path produced by nonlinear propagation of the (a) first laser pulse in an unaltered sapphire crystal and identical second pulse which is delayed by (b) 16 ns and (c) 400 ps with energies of 1.28 μJ . (d-f) display the corresponding temporal dynamics, where negative time represents the leading front of the pulse. (g-i) display the corresponding spectral dynamics and z denotes the propagation distance.

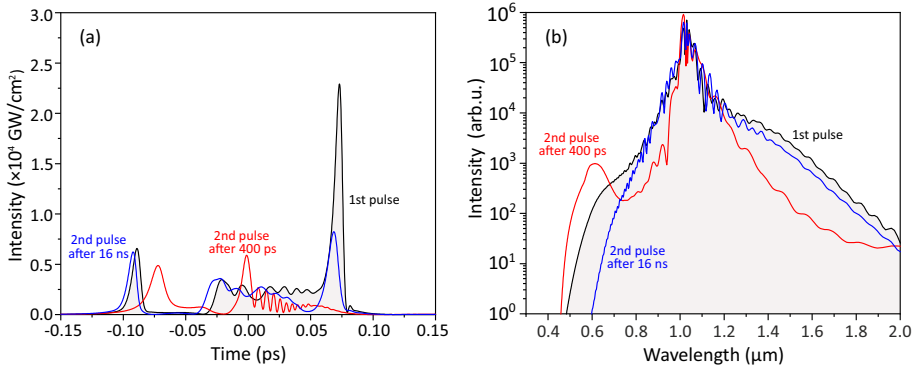


Fig. 5.8 (a) Intensities of first and second pulses which are delayed by 16 ns and 400 ps with energies of 1.28 μJ and (b) corresponding spectra at the center of the beam at $z = 3.7$ mm.

dynamics of the first pulse is depicted in Fig. 5.7 (d). Compared to the lower input pulse energy case [Fig. 5.5 (d)], here the nonlinear focus is located much closer to the entrance face of the nonlinear material (at $z \approx 0.5$ mm), and the pulse experiences a dramatic plasma-induced reduction of its width that

results in significant spectral broadening, which is especially pronounced on the long wavelength side, see Fig. 5.7 (g). At the same time, an extended plasma channel (~ 1 mm-long, with almost uniform free electron density of $\sim 10^{20} \text{ cm}^{-3}$, see Fig. 5.4 (b) and Fig. 5.7 (a) is produced in the pulse wake, so the replenished pulse at the beam center emerges only after $z \approx 2.8$ mm of propagation. The replenished pulse thereafter self-focuses and undergoes pulse splitting $z \approx 3.1$ mm, while explosive broadening of the spectrum towards the short wavelength side induced by self-steepening of the trailing sub-pulse takes place at $z \approx 3.7$ mm, see Fig. 5.7 (g) and Fig. 5.8 (a, b). In the present case, the overall nonlinear dynamics resembles complex temporal evolution of a picosecond laser pulse undergoing filamentation to a great extent [67].

The temporal dynamics of the second laser pulse that is delayed by 16 ns is depicted in Fig. 5.7 (e). Although the general temporal dynamics of the second pulse is similar to that of the first pulse in the burst, after splitting of the replenished pulse, the trailing sub-pulse experiences slower self-steepening, and so produces rather gradual than explosive spectral broadenings towards short wavelength side, see Fig. 5.7 (h). This drop in intensity of the trailing portion of the pulse, along with corresponding narrowing of its spectrum compared to the first pulse, is also visible in Figs. 5.8 (a, b).

The free electron plasma distribution of the second laser pulse that is delayed by 400 ps shifts slightly toward the front face of the sapphire crystal [Fig. 5.7 (c)]. The temporal dynamics of this pulse is illustrated in Fig. 5.7 (f), demonstrating its completely different temporal behavior. In this case, residual free electrons and STEs facilitate the generation of higher density free electron plasma via faster onset of avalanche ionization and optically-induced dissociation of STEs, whose radial distribution mimics the distribution of free electrons shown in Fig. 5.4 (b). As a result, the pulse experiences strong defocusing as a whole, without producing a characteristic plasma-shortened fragment. The replenished pulse gradually emerges at the temporal position that is shifted to the forefront, in the time frame of the input pulse, until self-focuses and splits at $z \sim 2.5$ mm, yielding very broad SC spectrum, whose evolution versus the propagation distance is shown in Fig. 5.7 (i). This temporal and spectral behavior is even more pronounced at $z \approx 3.7$ mm, as illustrated in Figs. 5.8 (a, b).

5.5 Summary and outlook

In conclusion, burst-mode filamentation and SC generation in a solid-state material (sapphire crystal) were investigated both experimentally and numerically. The study focused on bursts containing two identical femtosecond pulses, with a time delay between adjacent pulses of 16 ns and 400 ps, corresponding to intra-burst repetition rates of 62.5 MHz and 2.5 GHz, respectively. The measured spectral dynamics versus pulse energy demonstrated an increase of SC generation threshold for the second pulse in the burst, and this increase was found significant when the second pulse was delayed by 400 ps. The numerical simulations showed good agreement with the experimental findings, providing insights into temporal and spectral dynamics of individual pulses in the burst. It is demonstrated that residual free electron plasma and STEs from the first pulse contribute to elevated densities of free electron plasma generated by the successive pulse, thus substantially altering the dynamics of its nonlinear propagation and spectral broadening. More specifically, the residual free electron plasma provides initial population for faster onset of avalanche ionization, while optically-induced dissociation of STEs contributes to an increase of electron density in the conduction band, resulting in stronger plasma defocusing experienced by the second pulse in the burst. The investigated example of sapphire as the nonlinear material suggests that, in the case of the second pulse delayed by 400 ps, the nonlinear dynamics of the successive pulse is affected by both effects, whereas in the case of a 16 ns delay, the nonlinear dynamics of the successive pulse is affected mainly by optically-induced dissociation of residual STEs. The numerical simulations also unveiled how the temporal dynamics of the pulse, and the second pulse in the burst, in particular, change when the pulse energy increases, which could not be retrieved by simple means experimentally.

This study also suggests that the lifetimes of transient excitations and carrier dynamics are of utmost importance regarding robust and durable operation of the nonlinear material in adverse pumping conditions. Similar considerations may apply for what concerns other slow processes, such as local heating, heat diffusion and pressure wave propagation, which would certainly play a role in the case of many pulses in the burst, as well as in the case of continuous irradiation of nonlinear material by single laser pulses at high repetition rate.

Appendix. The numerical model

The laser pulse propagation through the nonlinear material was modeled with the use of the modified nonlinear Schroedinger equation e.i. by solving the unidirectional nonlinear propagation equation for the pulse envelope in the spectral domain [187]:

$$\frac{\partial S(\Omega, k_{\perp})}{\partial z} + iD(\Omega, k_{\perp}) = S_N(\Omega, k_{\perp}), \quad (5.1)$$

where z is the propagation coordinate, $\Omega = \omega - \omega_0$ is the frequency shift from the carrier frequency, ω_0 and k_{\perp} is the transverse wave number. The function $D(\Omega, k_{\perp})$ describes the linear propagation of light and accounts for diffraction and dispersion of the wave packet (ultrashort-pulsed laser beam) in nonparaxial approximation:

$$D(\Omega, k_{\perp}) = \sqrt{k(\omega_0 + \Omega)^2 - k_{\perp}^2} - k_0 - \frac{\Omega}{v_g}, \quad (5.2)$$

where $v_g = \frac{\partial \omega}{\partial k} |_{\omega_0}$ is the group velocity, $k(\omega) = \frac{n(\omega)\omega}{c}$ describes the dispersion relation and $k_0 = k(\omega_0)$. The complex pulse envelope $A(t, r)$, where t and r are the time and radial coordinates, respectively, was calculated by applying Hankel-Fourier transform:

$$A(t, r) = \int_{-\infty}^{+\infty} \int_0^{+\infty} S(\Omega, k_{\perp}) e^{i\Omega t} J_0(k_{\perp} r) k_{\perp} dk_{\perp} \frac{d\Omega}{2\pi}, \quad (5.3)$$

where J_0 is the zeroth-order Bessel function. The term on the right-hand side of Eq. (5.1) accounts for nonlinear pulse propagation and is expressed as:

$$S_N(\Omega, k_{\perp}) = \int_{-\infty}^{+\infty} \int_0^{+\infty} N(t, r) e^{-i\Omega t} J_0(k_{\perp} r) r dr dt. \quad (5.4)$$

The nonlinear term $N(t, r)$ is defined as:

$$\begin{aligned} N(t, r) = & \frac{i\omega_0 n_2}{c} |A|^2 A - \frac{\beta_e^{K_e}}{2} |A|^{2K_e-2} A - \frac{\beta_{STE}^{K_{STE}}}{2} |A|^{2K_{STE}-2} A - \\ & - \frac{\sigma_e}{2} (1 + i\omega_0 \tau_c) \rho_e A - i \frac{\sigma_{STE}}{2} \sigma_{STE} A. \end{aligned} \quad (5.5)$$

The first term in Eq. (5.5) refers to the optical Kerr effect, where n_2 is the nonlinear refractive index of sapphire crystal (see Table 2.1). The second and

third terms refer to the multi-photon absorption from the contributing states where β stands for the absorption cross section, K denotes the multiphoton absorption order, and ρ is the population density, while subscripts e and STE stand for electrons and STEs, respectively. The fourth term describes the contribution from the avalanche ionization estimated using Drude model, with the coefficient σ_e given by:

$$\sigma_e = \frac{e^2 \tau_c}{cn_0 \epsilon_0 m (1 + \omega_0^2 \tau_c^2)}, \quad (5.6)$$

where $\tau_c = 1.5$ fs is the electron collision time, ϵ_0 is the vacuum permittivity, and e and m denote the electron charge and reduced mass, respectively. The fifth term describes the phase retardation induced by STEs via Lorentz model according to [192]:

$$\sigma_{STE} = \frac{\omega_0 n(\omega_0) \omega_{STE, crit}^2 (\omega_{STE}^2 - \omega_0^2)}{c((\omega_{STE}^2 - \omega_0^2) + (\frac{\omega_0}{\tau_c})^2)}, \quad (5.7)$$

where ω_{STE} is the resonant frequency of STEs and $\omega_{STE, crit} = \sqrt{e^2/(m\epsilon_0)}$.

The material excitation was calculated using rate equations for both electron and STE populations, taking into account the three characteristic relaxation times of the latter. The rate equation for electrons reads as

$$\frac{\partial \rho_e}{\partial t} = (\rho_n - \rho_e) W_{Mp_e} + \rho_e W_{Av} + \rho_{STE} W_{Mp_{STE}} - \rho_e W_{r_e} \quad (5.8)$$

where $\rho_n = 2.1 \times 10^{22} \text{ cm}^{-3}$ is the density of bound electrons,

$$W_{Mp_e} = \frac{\beta_e}{K_e \hbar \omega_0} |A|^{2K_e} \quad (5.9)$$

and

$$W_{Mp_{STE}} = \frac{\beta_{STE}}{K_{STE} \hbar \omega_0} |A|^{2K_{STE}} \quad (5.10)$$

are the multiphoton ionization rates obtained using Keldysh formulation for electrons and STEs respectively, $W_{Av} = \sigma_e |A|^2 / U_e$ is the avalanche ionization rate, and $W_{r_e} = 1/\tau_{r_e}$ is the electron recombination rate. The simplified rate equation for STEs reads as

$$\frac{\partial \rho_{STE}}{\partial t} = -\rho_{STE} W_{Mp_{STE}} - \rho_{STE} W_{r_{STE}} + \rho_e W_{r_e} \eta_{STE}, \quad (5.11)$$

where η_{STE} is the exciton trapping efficiency, which was assumed to be 20%, i.e. 20% of electrons in the conduction band form STEs upon relaxation. The rate equations were solved simultaneously using sixth order Runge-Kutta method.

The simulation procedure for the excited state populations was performed as follows. First, the excited state populations were calculated simultaneously with the propagation of the first pulse, within a time frame equal to five times the pulse duration ($\sim 200 \text{ fs} \times 5 = 1000 \text{ fs}$). Thereafter, the relatively slow relaxation processes in the 0.1 – 100 ns timescale (relaxation of electron population in the conduction band, formation and decay of STEs) within the time interval between adjacent pulses were simulated separately with a much greater time step. The residual spatial distributions of the electron and STE densities at the moment of the second pulse arrival influence the nonlinear absorption and linear pulse propagation properties due to refractive index change, which was accounted via Drude-Lorentz model formalism.

Conclusions

- Owing to high nonlinearity, narrow and medium bandgap dielectric materials possess low filamentation and SC generation thresholds, low absolute values of nonlinear losses and consequently, significantly reduced bulk heating. The measured cut-off wavelengths at the short-wavelength side are in line with the general trend of blue-shifted spectral broadening on the bandgap of nonlinear material. All investigated nonlinear materials produced reasonable red-shifted spectral broadenings under conditions of optimal pump pulse energies. Out of these, KGW and YVO₄ demonstrated durable, optical damage-free performance at 2 MHz pulse repetition rate, while such performance in GGG and BGO is achieved at 200 kHz, suggesting that these materials are good alternatives to sapphire and YAG for low threshold, high average power supercontinuum generation in the near- and short-wave infrared spectral ranges.
- High average power, low threshold, stable octave-spanning SC generation in undoped KGW crystal, pumped with a total average power of 6.4 W from a commercial Kerr-lens mode-locked Yb:KGW oscillator with pulse repetition rate of 76 MHz was demonstrated for the first time. The SHG-FROG characterization of the SC pulses revealed pulse splitting, which is a universal feature of filamentation and SC generation in the range of normal GVD of the nonlinear material. The retrieved sub-pulses were shown possessing well-behaved spectral phases, suggesting their compressibility close to the transform limit. SC generation in highly nonlinear bulk material represents a robust and reliable broadband oscillator-driven all-solid-state platform, which could readily serve as an attractive alternative to alignment-sensitive SC generation schemes based on structured materials and optical fibers.

- A proof of principle of a simple all-solid-state post-compression setup for low-energy laser pulses is demonstrated, where 75 fs, 210 nJ pulses from pre-chirp-managed (PCMA) rod-type single-pass 76 MHz, 15.7 W Yb-fiber amplifier were sequentially spectrally broadened in ZnS and YAG samples of 2 mm and 15 mm thickness, respectively, and compressed to 37 fs using Gires-Tournois interferometric mirrors. The spatial-spectral characterization of post-compressed pulses with an average power of 11.47 W attested to the almost uniform spectral distribution across the beam (the spectral overlap parameter $V > 83\%$) and good beam quality ($M^2 = 1.28 \times 1.14$). These results suggest that spectral broadening of low energy pulses in highly nonlinear bulk materials could be a potentially attractive alternative to fiber-based spectral broadening, offering a virtually alignment-insensitive, low-complexity and low-cost all-solid-state arrangement for post-compression of low-energy pulses at high laser pulse repetition rates.
- Burst-mode SC generation in sapphire using bursts consisting of two 190 fs, 1030 nm pulses with time delays between adjacent pulses of 16 ns and 400 ps, corresponding to intra-burst repetition rates of 62.5 MHz and 2.5 GHz respectively, revealed higher filamentation and SC generation threshold for the second pulse in the burst, which increases with increasing intra-burst repetition rate. The experimental results were quantitatively reproduced numerically, showing that residual free electron plasma and self-trapped excitons contribute to elevated densities of free electron plasma generated by the second pulse in the burst and so stronger plasma defocusing, significantly affecting its nonlinear propagation. The presented results identify the fundamental and practical issues for supercontinuum generation in solid-state materials using femtosecond pulse bursts with high intra-burst repetition rates, which may also apply to the case of single pulses at high repetition rate, where residual material excitations become relevant and should be accounted for.

Santrauka lietuvių kalba

Įvadas

Atradus superkontinuumo (SK) generacijos reiškinį 1970 m. [1, 2], dėka išpūdingo kietakūnių lazerinių šaltinių technologijos progreso, SK generacija kietakūnėse terpėse tapo gerai išvystyta ir plačiai taikoma technologija. Jos dėka gaunama labai plataus spektro spinduliuotė, pasižyminti aukštu erdvinio bei laikiniu koherentiškumu, kuris ekvivalentus baltos šviesos lazerinei spinduliuotei [3, 4]. SK generacija skaidriose tūrinėse kietakūnėse terpėse vyksta dėl specifinio netiesinio sklidimo režimo, kurio metu šviesos pluoštas suformuoja femtosekundinę šviesos giją - labai mažų matmenų šviesos pluoštą su labai plačiu laikinių dažnių spektru [5, 6]. Šviesos gija susidaro dėka dinaminio balanso tarp fokusavimosi dėl Kerro reiškinio, pluošto difrakcijos ir defokusavimo dėl laisvųjų elektronų plazmos, kurią sukuria daugiafotonė sugertis ir smūginė jonizacija, o jos laikinį poveikslą normalios grupinių greičių dispersijos medžiagoje lemia impulso skilimas ir sub-impulsų frontų statėjimas, kas savo ruožtu sąlygoja staigų ir smarkų spektro išplitimą [7, 8].

SK spektro išplitimo diapazonas yra labai svarbus praktiniams taikymams, o jį lemia žadinimo bangos ilgis ir medžiagos savybės, tokios kaip tiesinis ir netiesinis lūžio rodikliai bei draustinės juostos plotis. Šie medžiagos parametrai apibrėžia kritinę fokusavimosi galią (kuri turi būti viršyta, kad formuotųsi šviesos gija) bei soties intensyvumą (kuris yra proporcingas daugiafotonės sugerties eilei), ir gerai paaiškina eksperimentinius duomenis daugeliui skaidrių medžiagų [9, 10], taip pat žr. [11], kur apibendrinti naujausi rezultatai. Eksperimentiniai tyrimai atskleidė, kad mėlynasis (trumpabangis) SK spektro poslinkis yra proporcingas santykiui $U_g/\hbar\omega_0$, čia U_g yra medžiagos draustinės juostos plotis, o $\hbar\omega_0$ yra žadinimo spinduliuotės fotono energija. Tuo tarpu raudonasis (ilgabangis) SK spektro poslinkis nėra griežtai apibrėžtas ir smarkiai pri-

klauso nuo žadinimo pluošto fokusavimo sąlygų (skaitinės apertūros) ir gali smarkiai skirtis netgi toje pačioje netiesinėje medžiagoje. Eksperimentiniai ir skaitmeninio modeliavimo rezultatai parodė, kad švelnus fokusavimas leidžia pasiekti didžiausią ilgabangį SK spektro poslinkį ir optimizuoti SK spektro raudonąją dalį [12, 13].

Nuo seno femtosekundinio SK spinduliuotė plačiai taikoma kaip plataus spektro užkrato signalas parametriniams šviesos stiprintuvams (PŠS): regimoji (trumpabangė) SK spektro dalis naudojama kaip užkratas antrąja ir trečiąja lazerio harmonikomis kaupinamiems PŠS, o infraraudonoji (ilgabangė) SK spektro dalis naudojama kaip užkratas pagrindine lazerio harmonika kaupinamiems PŠS [14]. Femtosekundinio SK generacijos tūrinėse medžiagose metodai buvo ištobulinti žadinimui naudojant Ti:safyro lazerius, o safyro ir YAG kristalai buvo identifikuoti kaip efektyviausios ir patikimiausios šiam tikslui naudojamos netiesinės medžiagos [12]. Šios patirtys buvo pritaikytos ir Yb lazeriams, kurie nepaisant ilgesnės impulso trukmės, nukonkuravo Ti:safyro lazerius impulsų pasikartojimo dažniu ir pasiekia vidutine galia. Kaupinant pažangiais femtosekundiniais Yb lazeriais, buvo sukurti SK spinduliuotę stiprinantys PŠS, kurie veikia MHz impulsų pasikartojimo dažniu ir generuoja derinamo bangos ilgio, keleto optinių ciklų trukmės impulsus įvariose spektro srityse, nuo ultravioletinės iki vidurinės infraraudonosios [15–22]. Taipogi buvo pademonstruoti MHz impulsų pasikartojimo dažniu veikiantys optiniai parametriniai čirpuotų impulsų stiprintuvai (OPCPA), kurie SK spinduliuotę naudoja pradinėse plačiajuosčio signalo formavimo pakopose [23, 24]. Tūrinėse medžiagose generuojamas MHz pasikartojimo dažnio SK matomas kaip labai patraukli alternatyva SK generacijai fotoninių kristalų šviesolaidžiuose, tokiems taikymams kaip impulsų post-spūda iki keleto optinių ciklų trukmės [25], laiko skyros žadinimo-zondavimo spektroskopija [26], didelės spartos koherentinė anti-Stokso Ramano sklaida (CARS) ir vaizdinimas [27, 28], netiesinė mikroskopija [29] ir kt.

Plati praktinių taikymų įvairovė reikalauja optimizuoti visą eilę svarbių SK spinduliuotės parametų, tokių kaip pluošto kokybė [30], poliarizacinės savybės [31], erdvinis-laikinis bei erdvinis-spektrinis koherentiškumas [32], bangos ilgio stabilumas ir laikinis tirtėjimas [33] bei nešančiojo dažnio fazinis triukšmas [34]. Per pastarąjį dešimtmetį atlikti išsamūs tyrimai ieškant naujų ir efektyvių netiesinių medžiagų SK generacijai, žadinant pagrindinėmis Ti:safyro ir Yb lazerių harmonikomis [35–44], o pastaruoju metu ir naudojant naujai

sukurtus femtosekundinius lazerius, tokius kaip Cr:ZnSe [45, 46]. Reikšmingos pastangos buvo nukreiptos siekiant generuoti SK spinduliuotę su dideliu spektriniu energijos tankiu norimose bangos ilgio intervaluose žadinimui naudojant kelis pluoštus [47, 48] arba naudojant netiesines medžiagas su specialiai modifikuota struktūra: tūryje įrašytus bangolaidžius [38, 49], monokristalinius šviesolaidžius [50], skysčių čiurkšles [51], kompozitines medžiagas [52] ir polikristalines keramikas [53, 54].

Kita vertus, šiuolaikiniai praktiniai SK taikymai reikalauja patikimos SK generacijos veikos esant dideliam (šimtų kHz ir didesniai) impulsų pasikartojimo dažniui, koku veikia pažangios Yb lazerinės sistemos. Tokiomis veikos sąlygomis daugelio impulsų poveikyje gali atsirasti liekamieji reiškiniai medžiagoje (defektų kūrimas, šilumos kaupimasis), kurių rezultate gali būti modifikuojamos medžiagos optinės savybės, dėl ko savo ruožtu gali smarkiai siaurėti SK spektro plotis, o medžiagoje ilgai išsivystyti katastrofinis optinis pažeidimas. Tačiau kol kas tokios tematikos tyrimų nėra atlikta daug [55, 56], ypač turint omenyje šiuolaikinių Yb lazerių galimybes veikti impulsų papliūpų režime, generuojant impulsus su pasikartojimo dažniais nuo multi MHz iki keleto GHz, o taip pat stiprinant femtosekundinius impulsus strypo tipo Yb šviesolaidiniuose stiprintuvuose, veikiančiuose osciliatoriaus pasikartojimo dažniu, žr. pvz. [57, 58].

Darbo tikslas

Šis disertacinis darbas skirtas eksperimentiškai ištirti superkontinuumo generaciją turinėse siauros ir vidutinės draustinės juostos dielektrinėse medžiagose esant dideliui impulsų pasikartojimo dažniui, o jo tikslas yra identifikuoti tinkamiausias netiesines medžiagas, pasižyminčias žemu superkontinuumo generacijos slenksčiu, efektyvia spektro plėtra ir patikima ilgalaikė veikla, žadinant šiuolaikiniais ultrasparčiais didelės vidutinės galios Yb lazeriais.

Mokslinis darbo naujumas

Šiame darbe ištirta visa eilė siauros ir vidutinės draustinės juostos medžiagų ir atskleisti fizikiniai reiškiniai, kurie vaidina svarbų vaidmenį formuojant femtosekundines šviesos gijas ir generuojant superkontinuumo spinduliuotę esant dideliui impulsų pasikartojimo dažniui:

- Pademonstruota, kad siauros ir vidutinės draustinės juostos netiesinės medžiagos dėka didelio netiesiškumo pasižymi žemu SK generacijos slenksčiu, kas sąlygoja mažesnę medžiagos sugertą absoliučios energijos kiekį ir savo ruožtu mažesnę medžiagos tūrio kaitimą, kuo galima iš dalies paaiškinti stabilų ilgalaikį šių medžiagų veikimą esant dideliame impulsų pasikartojimo dažniui.
- Pirmą kartą pademonstruota stabili, žemo slenksčio ir optinės oktavos spektro pločio SK generacija vienalytėje didelio netiesiškumo tūrinėje medžiagoje (nelegiruotame KGW kristale) tiesiogiai žadinant Kerro lęšiu sinchronizuotą modų 76 MHz Yb:KGW osciliatoriaus impulsais.
- Pademonstruota, kad femtosekundinių lazerio impulsų spektro plėtra didelio netiesiškumo tūrinėse medžiagose gali būti patraukli alternatyva spektro plėtrai šviesolaidžiuose, realizuojant paprastas ir derinimui nejautrias post-spūdos schemas, tinkamas mažos energijos (~200 nJ) ir didelio pasikartojimo dažnio impulsams spausti.
- Pirmą kartą ištirta SK generacija tūrinėje kietakūnėje terpėje (safyro kristale) žadinant didelio pasikartojimo dažnio (laiko intervalai tarp gretimų impulsų 16 ns ir 400 ps) femtosekundinių impulsų papliūpomis. Atskleista, kad dėl pirmojo impulso sukurtos liekamosios laisvųjų elektronų plazmos ir autolokaliuotų eksitonų, padidėja antrojo impulso kuriamos plazmos tankis, sąlygojantis stipresnę pluošto defokusamą, kas savo ruožtu esmingai pakeičia antrojo impulso netiesinį sklidimą ir spektro plėtrą. Šie liekamieji medžiagos sužadainimai gali tapti svarbūs ir pavieniams didelio pasikartojimo dažnio impulsams.

Praktinė darbo vertė

Šiame darbe identifikuotos naujos efektyvios netiesinės tūrinės medžiagos ir atskleisti praktiniai aspektai, kurie svarbūs optimizuojant didelio pasikartojimo dažnio SK generacijos bei impulsų spūdos schemas, kurios gali būti tiesiogiai integruotos į didelės vidutinės galios parametriniu šviesos stiprinimu paremtus derinamo bangos ilgio šviesos šaltinius bei didelės spartos spektroskopines ir vaizdinimo sistemas:

- Nelegiruoti KGW ir YVO₄ kristalai pasižymi žemu SK generacijos slenksčiu, stabilia ir ilgalaikė veikia, juose stebimas tik nežymus tūrio kaitimas esant 2 MHz impulsų pasikartojimo dažniui (GGG ir BGO esant 200 kHz), o generuojama SK spinduliuotė pasižymi daugiau nei optinės oktavos spektro pločiu ir dideliu raudonuoju dažnio poslinkiu. Šių savybių visuma užtikrina tinkamą kaupinimo energijos proporciją tarp užkrato signalo generavimo ir stiprinimo kanalų, kas yra svarbu vystant didelės vidutinės galios parametrinius šviesos stiprintuvus, veikiančius artimojoje ir vidurinėje infraraudonojoje spektro srityje.
- Pademonstruota, kad žadinant santykinai ilgais (~200 fs) femtosekundiniais impulsais, maksimalus spektro plitimas į trumpabangę ir ilgabangę puses pasiekiamas esant labai skirtingoms žadinimo energijoms, kas svarbu optimizuojant didelio pasikartojimo dažnio SK generacijos schemas.
- Pademonstruota didelės vidutinės galios, žemo slenksčio, stabilaus optinės oktavos spektro pločio SK generacija nelegiruotame KGW kristale, žadinant 6.4 W vidutinės galios, 76 MHz pasikartojimo dažnio komercinio Yb:KGW osciliatoriaus impulsais. Ši netiesinė medžiaga galėtų būti patraukli alternatyva struktūrinėms tūrinėms medžiagoms ir šviesolaidžiams, taip smarkiai supaprastinant užkrato signalo generacijos pakopą didelio pasikartojimo dažnio ir didelės vidutinės galios parametriniuose šviesos stiprintuvuose.
- Pademonstruota principinė mažos energijos (210 nJ) ir didelio pasikartojimo dažnio (76 MHz) pastiprintų Yb:KGW osciliatoriaus impulsų kietakūnė spūdos schema, naudojant pakopinę spektro plėtrą ZnS ir YAG kristaluose ir čirpo kompensavimą Gires-Tournois interferometriniais (GTI) veidrodžiais.
- Atskleisti praktiniai SK generacijos impulsų papliūpomis kietakūnėse terpėse apribojimai, susiję su SK generacijos slenksčio padidėjimu antrajam (ir kiekvienam po to sekančiam) impulsui, kuris ir toliau didėja didinant impulsų pasikartojimo dažnį papliūpoje.
- Pademonstruota, kad spektriniai šviesos gijų indukuotos liuminescencijos matavimai gali būti pritaikyti medžiagų scintiliacinių savybių tyri-

mams, žadinimui naudojant šviesos gijas, kurios daugiafotoniškai sužadina medžiagą, kas įgalina lengvai atskirti žadinimo ir spinduliavimo spektrus bei nesukelia optinio medžiagos pažeidimo rizikos.

Sprendžiami uždaviniai

- Išsamus šviesos gijų susidarymo ir SK generacijos tyrimas (spektro plėtros dinamika, šviesos gijos liuminescencija, netiesiniai nuostoliai ir medžiagos tūrinis kaitimas) nelegiruotuose siauros (KGW, YVO₄, BGO, LT) ir vidutinės (GGG, YSO, LSO, LYSO) draustinės juostos dielektriniuose kristaluose žadinant keičiamo iki 2 MHz pasikartojimo dažnio Yb:KGW lazerio impulsais ir šių medžiagų veikos palyginimas su įprastiniais safyro ir YAG kristalais esant identiškoms eksperimento sąlygoms.
- Didelio pasikartojimo dažnio (76 MHz) superkontinuumo generacijos tyrimas tūrinėse netiesinėse terpėse žadinant sub-100 nJ energijos Yb:KGW osciliatoriaus impulsais.
- Mažos energijos (210 nJ), didelio pasikartojimo dažnio (76 MHz) pastiprintų Yb:KGW osciliatoriaus impulsų spūdos tyrimas taikant pakopinę spektro plėtrą didelio netiesiškumo tūrinėse medžiagose (ZnS, KGW ir YAG) ir čirpo kompensavimą Gires-Tournois interferometriniais (GTI) veidrodžiais.
- Eksperimentinis ir skaitmeninis SK generacijos tyrimas safyro kristale, žadinant 190 fs trukmės, 1030 nm bangos ilgio dviejų impulsų papliūpomis esant laiko intervalams tarp gretimų impulsų 16 ns ir 400 ps.

Ginamieji teiginiai

- Dėka didelio netiesiškumo, žemo šviesos gijų formavimo bei SK generacijos slenksčio ir mažo absoliučaus dėl daugiafotonės sugerties medžiagai perduodamo energijos kiekio, siauros ir vidutinės draustinės juostos dielektrikai yra tinkamos medžiagos didelio pasikartojimo dažnio SK generacijai, žadinant femtosekundiniais pažangių Yb lazerių impulsais.

- Nelegiruotas KGW kristalas yra patvari vienvalytė tūrinė netiesinė medžiaga stabilaus optinės oktavos spektro pločio SK generacijai, žadinant 76 MHz Yb:KGW osciliatoriaus impulsais.
- Pakopinė spektro plėtra didelio netiesiškumo tūrinėse medžiagose įgalina pasiekti vienvalytį spektro skirstinį skersai pluošto ir tokiu būdu leidžia įgyvendinti paprastą ir derinimui nejautrią kietakūnę konfigūraciją mažos energijos (~ 200 nJ) ir didelio pasikartojimo dažnio impulsų post-spūdai.
- Liekamieji medžiagos sužadainimai (laisvųjų elektronų plazma ir autokalizuoti eksitonai) laikinai pakeičia medžiagos savybes ir reikšmingai įtakoja kiekvieno sekančio impulso netiesinį sklidimą ir spektro plėtrą SK žadinant impulsų papliūpomis.

Trumpa pagrindinių rezultatų apžvalga

Pirmame skyriuje aprašomi svarbiausi SK generaciją lemiantys, vienu metu pasireiškiantys ir tarpusavyje sąveikaujantys, netiesinės optikos reiškiniai: pluoštų fokusavimasis, impulso fazės moduliavimasis, laisvųjų elektronų plazmos formavimasis ir jos sukelti efektai, laikinis impulsų sustatėjimas ir skilimas. Literatūros apžvalgoje išskiriami du šviesos gijos formavimosi ir SK generacijos scenarijai: žadinant 100 fs ir trumpesniais impulsais, žadinant ilgais, 200 fs, sub-pikosekundiniais ir pikosekundiniais impulsais. Taip pat aptariamos problemos SK žadinant didelio pasikartojimo dažnio impulsais, tokios kaip šiluminiai efektai, optinis medžiagos pažeidimas ir naujų atsparių kietakūnių medžiagų poreikis.

Antrame skyriuje pristatomi lyginamojo tyrimo rezultatai generuojant SK nelegiruotuose safyro, itrio aliuminio granato (YAG), kalio gadolinio volframato (KGW), itrio vanadato (YVO_4) bismuto germanato (BGO), gadolinio galio granato (GGG), liutecio oksidortosilikato LSO, liutecio ir itrio oksidortosilikato (LSYO), itrio ortosilikato (YSO) ir ličio tantalato (LT) kristaluose, žadinant 1030 nm bangos ilgio, ~ 200 fs trukmės, derinamo, nuo 10 kHz iki 2 MHz, pasikartojimo dažnio Yb:KGW lazerio impulsais. Šis tyrimas atskleidė, kad lyginant su etaloniniais safyro ir YAG kristalais, BGO, KGW, YVO_4 , LT ir GGG kristalai dėl didelio netiesiškumo pasižymi apie 2-4 kartus žemesniais SK generacijos slenksčiais. Nors spektro plėtra į regimąją spektro pusę šiuose kristaluose yra nedidelė (iki ~ 600 nm), tačiau jie pasižymi efektyvia spektro

plėtra į infraraudonąją spektro sritį (iki 1700 nm, iki 1900 nm, iki 1970 nm ir iki 2030 nm YVO₄, LYSO, KGW ir GGG kristaluose atitinkamai) bei dideliu spektriniu SK spinduliuotės energijos tankiu. Išmatavus netiesinius energijos nuostolius dėl daugiafotonės ir laisvųjų elektronų plazmos sugerties, nustatyta, kad esant optimaliai žadinimo energijai (kuomet generuojami stabilūs ir tolydūs SK spektrai), absoliučios sugertos energijos vertės KGW ir YVO₄ kristaluose yra bent 3 kartus mažesnės nei safyre ir YAG. Dėl šios priežasties KGW ir YVO₄ kristalai žymiai mažiau kaista (iki 10-20 °C ir iki 5-7 °C virš kambario temperatūros, be ir su papildomu šilumos nuvedimu atitinkamai). Parodyta, kad tokiais žadinimo sąlygomis šie kristalai optiškai nedegraduoja, ir juose galima realizuoti ilgalaikę stabilią SK generaciją. Šio tyrimo rezultatai atskleidė, kad YVO₄ ir KGW turi didelį potencialą SK generacijai IR spektro srityje, kur ši plataus spektro spinduliuotė toliau gali būti naudojama kaip užkrato signalas didelės vidutinės galios OPA ir OPCPA sistemose, kuriose impulsų pasikartojimo dažnis yra didelis, bet pavienio kaupinimo impulso energija yra palyginti maža, tad yra labai svarbus turimos energijos paskirstymas tarp užkrato generacijos ir stiprinimo kanalų. Taip pat šis tyrimas pademonstravo, kad anksčiau SK generacijai beveik arba visiškai nenaudoti BGO, GGG, LSO, LYSO ir YSO, tačiau plačiai taikomi kaip labai efektyvios scintiliacinės medžiagos, yra tinkamos medžiagos generuoti 2 oktavų SK spektrą, kuris palyginamas su YAG kristale žadinamu SK. Parodyta, kad LSO, LYSO ir YSO kristalai pasižymi ilgalaikiu stabilumu tik SK generacijai naudojant 10 kHz ir mažesnio pasikartojimo dažnio impulsus, tačiau BGO ir GGG kristaluose stabilaus SK generacija pademonstruota žadinant 200 kHz pasikartojimo dažnio impulsais.

Trečiame skyriuje pirmą kartą pademonstruota didelio (76 MHz) pasikartojimo dažnio, didelės vidutinės galios (6.4 W) superkontinuumo generacija vienalytėje didelio netiesiškumo terpėje – KGW kristale, žadinant ~100 fs trukmės, sub-100 nJ energijos komercinio Yb:KGW osciliatoriaus (FLINT, Light Conversion Ltd.) tiek papildomai strypo tipo stiprintuve sustiprintais, tiek nesustiprintais impulsais. Esant optimalioms žadinimo sąlygoms (impulso energija 84 nJ, vidutinė galia 6.4 W) sugeneruota daugiau nei optinės oktavos pločio (705-1460 nm) superkontinuumo spinduliuotė, kuri buvo išsamiai charakterizuota pasitelkiant kampinės skyros spektrinius matavimus bei antrosios harmonikos generacijos optinės sklendės su dažnine skyra (AHG-FROG) metodą. Pastarieji matavimų rezultatai atskleidė, kad superkontinuumo generacijos metu pradinis impulsas suskyla į du sub-impulsus, ko ir galima tikėtis vykstant sa-

viveikai kristalo normalios grupinių greičių dispersijos srityje. Laikinės ir spektrinės fazių rekonstrukcija iš AHG-FROG pėsakų parodė, kad kiekvienas sub-impulsas turi gerai apibrėžtus fazinius sąryšius tarp spektro komponentų (parabolinį fazės kitimo dėsnį), kas patvirtino aukštą tokios spinduliuotės koherentiškumo laipsnį, kuris savo ruožtu leidžia tikėtis sub-impulsų spūdumo iki spektro ribotos trukmės. Ilgalaikiai spektriniai matavimai pademonstravo stabilią superkontinuumo generacijos veiką daugiau nei 4 val. laikotarpyje, kuomet nebuvo pastebėti jokie spektriniai pokyčiai netgi visai netransliuojant kristalo žadinimo pluošto atžvilgiu. Šie rezultatai atveria visiškai naujas superkontinuumo generacijos galimybes turinėse terpėse, žadinimui naudojant femtosekundinius lazerinius osciliatorius, kas galėtų būti labai patraukli alternatyva derinimui (pluošto kryptčiai) jautrioms schemoms, kurios iki šiol rėmėsi superkontinuumo generacija fotoninių kristalų šviesolaidžiuose.

Ketvirtame skyriuje pademonstruota principinė sustiprintų Yb:KGW oscilatoriaus impulsų (impulsų trukmė 75 fs, energija 210 nJ, vidutinė galia 15.7 W) spūdos galimybė, spektro plėtrai naudojant įvairias dideliu netiesiškumu pasižyminčių plačios apertūros kietakūnių medžiagų: ZnS, KGW ir YAG kombinacijas. Efektyviausia spektro plėtra, kuomet dar nepasireiškia pluošto iškraipymai dėl saviveikos, gauta impulsams sklindant 2 mm storio ZnS ir po to 15 mm storio YAG kristaluose. Taip išplėsto spektro impulsai buvo suspausti iki 37 fs trukmės naudojant Gires-Tournois interferometrinius veidrodžius, o AHG-FROG metodu išmatuota impulsų trukmė buvo labai artima spektriškai riboto impulso trukmei (32 fs). Erdvinis-spektrinis suspaustų impulsų charakterizavimas parodė aukštą spektrinį homogeniškumą (spektro persiklojimo parametras $>83\%$) bei gerą pluošto kokybę ($M^2 = 1.28$ x ašies kryptimi ir $M^2 = 1.14$ y ašies kryptimi). Vidutinė išmatuota suspaustų impulsų galia siekė 11.47 W, o visos spūdos schemos energinis efektyvumas buvo 73%. Tačiau pažymėtina, kad visi energijos nuostoliai susidarė vien dėl Frenelio atspindžių nuo neskaidrintų netiesinių kristalų paviršių (9.5% ZnS, 16.5% YAG) ir 1.5% trijų atspindžių nuostolių interferenciniuose veidrodžiuose, tad optimizavus schemą naudojant skaidrintus elementus, energinį efektyvumą galima ženkliai padidinti. Apibendrinant šį rezultatą, galima teigti, kad mažos energijos impulsų spektro plėtra turinėse didelio netiesiškumo kietakūnėse terpėse pasižymi paprastumu ir leidžia sumažinti spūdos schemų jautrumą pluošto kryptčiai, ir tinkamai optimizavus, galėtų būti gera alternatyva šiuo metu naudojamai spektro plėtrai fotoninių kristalų šviesolaidžiuose.

Penktame skyriuje ištirti superkontinuumo generacijos safyro kristale ypatumai žadinant 190 fs trukmės impulsų papliūpomis, esant laiko intervalams tarp gretimų impulsų 16 ns ir 400 ps (atitinkamai 62.5 MHz ir 2.5 GHz pasikartojimo dažniai), naudojant 1 MHz dažniu veikiančią lazerinę sistemą (Carbide, Light Conversion Ltd.). Impulsų skaičių papliūpoje buvo galima varijuoti nuo 2 iki 10, tačiau dėl nevienodų impulsų amplitudžių buvo pasirinkta tik dviejų impulsų papliūpa, kuomet buvo galima impulsų amplitudes suvienodinti. Atliktas eksperimentinis tyrimas žadinant superkontinuumo spinduliuotę pavieniais 1 MHz pasikartojimo dažnio impulsais ir impulsų papliūpomis esant 16 ns ir 400 ps laiko intervalams tarp gretimų impulsų parodė, kad papliūpų režime reikalinga didesnė žadinimo energija, kad superkontinuumą generuotų abu impulsai. Žadinimo energijos padidėjimas buvo nežymus 16 ns laiko intervalais tarp gretimų impulsų papliūpoje, tačiau tapo ženklus esant 400 ps laiko intervalams papliūpoje. Siekiant paaiškinti šiuos eksperimento rezultatus, buvo sukurtas skaitmeninis modelis, kuris be saviveikos ir netiesinės sugerties reiškinių taipogi įskaitė laisvųjų elektronų plazmos relaksaciją bei autolokalizuočių eksitonų būsenų susidarymą bei jų netiesinę sugertį ir disociaciją. Modeliavimo rezultatai vienu ir kitu atveju gerai atkartojo eksperimento rezultatus ir atskleidė, kaip iš paskos atėjusio impulso netiesinis sklidimas stipriai paveikiamas liekamosios laisvųjų elektronų plazmos bei tarpinių būsenų (autolokalizuočių eksitonų) sugerties. Šie efektai pasireiškia generuojant didesnio tankio laisvųjų elektronų plazmą, kurios defokusuojantis poveikis savo ruožtu stipriai pakeičia netiesinį impulso sklidimą erdvinėje ir laikinėje plotmėse. Apibendrinus gautus rezultatus, galima teigti, kad praktinei superkontinuumo generacijai papliūpų režime būtinos arba lazerinės sistemos, kuriose norimu būdu galima reguliuoti atskirų papliūpos impulsų amplitudes arba naujos efektyvios netiesinės medžiagos, kuriose kiekvieno impulso sukelti pokyčiai relaksuoja sparčiau nei laikinis intervalas tarp impulsų papliūpoje.

Išvados

- Siauros ir vidutinės draustinės juostos dielektrikai dėka didelio netiesiškumo pasižymi žemais šviesos gijų formavimo ir SK generacijos slenksčiais, kas sąlygoja mažas absoliutines netiesinių nuostolių vertes ir reikšmingai sumažina medžiagos tūrinį kaitimą. Pademonstruota, kad šiose medžiagose SK spektro plėtra į trumpabangę pusę gerai atitinka bendrąją SK mėlynojo krašto priklausomybę nuo draustinės energijos tarpo, o esant optimaliai žadinimo energijai pasiekama ženkli SK spektro plėtra į ilgabangę pusę. Pademonstruota, kad KGW ir YVO_4 kristalai pasižymi žemu SK generacijos slenksčiu ir stabilia ilgalaikė SK generacijos veika esant 2 MHz, o GGG ir BGO kristalai – esant 200 kHz impulsų pasikartojimo dažniui, tad šios medžiagos yra puiki alternatyva safyro ir YAG kristalams didelės galios SK generacijai artimojoje ir vidurinėje infraraudonojoje spektro srityje.
- Pirmą kartą pademonstruota didelės vidutinės galios, žemo slenksčio, stabilios optinės oktavos spektro pločio SK generacija nelegiruotame KGW kristale, žadinant 6.4 W vidutinės galios, 76 MHz pasikartojimo dažnio komercinio Yb:KGW osciliatoriaus impulsais. SK impulsų charakterizavimas AHG-FROG metodu parodė impulsų laikinį skilimą, kuris yra universali laikinė šviesos gijų ir SK spinduliuotės savybė normalios dispersijos netiesinėje medžiagoje, o sub-impulsai pasižymi kvadratine laikine faze, kas leidžia juos efektyviai suspausti iki spektru ribotos trukmės. Tokia pilnai kietakūnė osciliatoriumi žadinamos plataus spektro spinduliuotės generacijos platforma galėtų būti labai patraukli alternatyva spektro plėtros sudėtingose struktūrinėse medžiagose ir šviesolaidžiuose schemoms.
- Pademonstruota principinė kietakūnė mažos energijos impulsų spūdos schema, kuomet 75 fs trukmės, 210 nJ energijos impulsų iš 76 MHz, 15.7 W Yb strypo tipo stiprintuvo spektras pakopiškai išplečiamas 2 mm ZnS ir 15 mm YAG kristaluose ir impulsas suspaudžiamas iki 37 fs naudojant Gires-Tournois interferometrinius veidrodžius. Parodyta, kad 11.47 W vidutinės galios suspausti impulsai pasižymi beveik vienalyčiu erdvinio-spektriniu skirstiniu (spektrinio persiklojimo parametras $V > 83\%$) ir gera pluošto kokybe ($M^2 = 1.28 \times 1.14$). Šie rezultatai rodo,

kad spektro plėtra didelio netiesiškumo medžiagose gali būti potencialiai patraukli alternatyva spektro plėtrai šviesolaidžiuose, įgalinanti realizuoti derinimui nejautrią, nesudėtingą ir pigią kietakūnę konfigūraciją didelio pasikartojimo dažnio ir mažos energijos impulsų spūdai.

- SK generacijos rezultatai safyro kristale impulsų papliūpomis, esant laiko intervalams tarp gretimų impulsų 16 ns ir 400 ps, sudarytomis iš dviejų 190 fs trukmės, 1030 nm bangos ilgio impulsų, parodė, kad antrajam impulsui padidėja SK generacijos slenkstis. Skaitmeninio modeliavimo rezultatai parodė, kad šį padidėjimą lemia pirmojo impulso sukurta liekamoji laisvųjų elektronų plazma ir autolokalizuoti eksitonai, dėl kurių padidėja antrojo impulso kuriamos plazmos tankis ir defokusavimas, kas savo ruožtu smarkiai įtakoja jo paties netiesinį sklidimą. Šie rezultatai atskleidžia fundamentines ir praktines SK generacijos impulsų papliūpomis problemas, kurios taip pat gali būti svarbios ir pavienių didelio pasikartojimo dažnio impulsų netiesiniam sklidimui.

BIBLIOGRAPHY

- [1] R. R. Alfano, S. L. Shapiro, Emission in the region 4000 to 7000 Å via four-photon coupling in glass, *Phys. Rev. Lett.* **24**, 584–587 (1970).
- [2] R. R. Alfano, S. L. Shapiro, Observation of self-phase modulation and small-scale filaments in crystals and glasses, *Phys. Rev. Lett.* **24**, 592–594 (1970).
- [3] A. Dubietis, G. Tamošauskas, R. Šuminas, V. Jukna, A. Couairon, Ultrafast supercontinuum generation in bulk condensed media, *Lith. J. Phys.* **57**, 113–157 (2017).
- [4] A. Dubietis, A. Couairon, *Ultrafast supercontinuum generation in transparent solid state media* (Springer Nature, Cham, 2019).
- [5] A. Couairon, A. Mysyrowicz, Femtosecond filamentation in transparent media, *Phys. Rep.* **441**, 47–189 (2007).
- [6] L. Bergé, S. Skupin, R. Nuter, J. Kasparian, J.-P. Wolf, Ultrashort filaments of light in weakly ionized, optically transparent media, *Rep. Prog. Phys.* **70**, 1633 (2007).
- [7] L. Gaeta, Catastrophic collapse of ultrashort pulses, *Phys. Rev. Lett.* **84**, 3582–3585 (2000).
- [8] L. Gaeta, Spatial and temporal dynamics of collapsing ultrashort laser pulses, *Top. Appl. Phys.* **114**, 399–411 (2009).
- [9] A. Brodeur, S. L. Chin, Band-gap dependence of the ultrafast white-light continuum, *Phys. Rev. Lett.* **80**, 4406–4409 (1998).
- [10] A. Brodeur, S. L. Chin, Ultrafast white-light continuum generation and self-focusing in transparent condensed media, *J. Opt. Soc. Am. B* **16**, 637–650 (1999).
- [11] A. Dubietis, V. Jukna, A. Couairon, *Supercontinuum in IR-MIR from narrow bandgap bulk solid-state materials* (Springer International Publishing, Cham, 2022), 457–477, edited by R. R. Alfano.
- [12] M. Bradler, P. Baum, E. Riedle, Femtosecond continuum generation in bulk laser host materials with sub-μJ pump pulses, *Appl. Phys. B* **97**, 561–574 (2009).
- [13] V. Jukna, J. Galinis, G. Tamosauskas, D. Majus, A. Dubietis, Infrared extension of femtosecond supercontinuum generated by filamentation in solid-state media, *Appl. Phys. B* **116**, 477–483 (2014).

- [14] C. Manzoni, G. Cerullo, Design criteria for ultrafast optical parametric amplifiers, *J. Opt.* **18**, 103501 (2016).
- [15] C. Schrieffer, S. Lochbrunner, P. Krok, E. Riedle, Tunable pulses from below 300 to 970 nm with durations down to 14 fs based on a 2 MHz ytterbium-doped fiber system, *Opt. Lett.* **33**, 192–194 (2008).
- [16] C. Homann, C. Schrieffer, P. Baum, E. Riedle, Octave wide tunable UV-pumped NOPA: pulses down to 20 fs at 0.5 MHz repetition rate, *Opt. Express* **16**, 5746–5756 (2008).
- [17] M. Emons, A. Steinmann, T. Binhammer, G. Palmer, M. Schultze, U. Morgner, Sub-10-fs pulses from a MHz-NOPA with pulse energies of 0.4 μ J, *Opt. Express* **18**, 1191–1196 (2010).
- [18] M. Bradler, C. Homann, E. Riedle, Mid-IR femtosecond pulse generation on the microjoule level up to 5 μ m at high repetition rates, *Opt. Lett.* **36**, 4212–4214 (2011).
- [19] M. Bradler, E. Riedle, Sub-20 fs μ J-energy pulses tunable down to the near-UV from a 1 MHz Yb-fiber laser system, *Opt. Lett.* **39**, 2588–2591 (2014).
- [20] J. Nillon, O. Crégut, C. Bressler, S. Haacke, Two MHz tunable non collinear optical parametric amplifiers with pulse durations down to 6 fs, *Opt. Express* **22**, 14964–14974 (2014).
- [21] S. Penwell, L. Whaley-Mayda, A. Tokmakoff, Single-stage MHz mid-IR OPA using LiGaS₂ and a fiber laser pump source, *Opt. Lett.* **43**, 1363–1366 (2018).
- [22] Y. Liu, P. Krogen, K.-H. Hong, Q. Cao, P. Keathley, F. X. Kärtner, Fiber-amplifier-pumped, 1-MHz, 1- μ J, 2.1- μ m, femtosecond OPA with chirped-pulse DFG front-end, *Opt. Express* **27**, 9144–9154 (2019).
- [23] R. Riedel, A. Stephanides, M. J. Prandolini, B. Gronloh, B. Jungbluth, T. Mans, F. Tavella, Power scaling of supercontinuum seeded megahertz-repetition rate optical parametric chirped pulse amplifiers, *Opt. Lett.* **39**, 1422–1424 (2014).
- [24] M. Puppín, Y. Deng, O. Prochnow, J. Ahrens, T. Binhammer, U. Morgner, M. Krenz, M. Wolf, R. Ernstorfer, 500 kHz OPCPA delivering tunable sub-20 fs pulses with 15 W average power based on an all-ytterbium laser, *Opt. Express* **23**, 1491–1497 (2015).
- [25] S. Goncharov, K. Fritsch, O. Pronin, Few-cycle pulse compression and white light generation in cascaded multipass cells, *Opt. Lett.* **48**, 147–150 (2023).
- [26] A. Grupp, A. Budweg, M. Fischer, J. Allerbeck, G. Soavi, A. Leitenstorfer, D. Brida, Broadly tunable ultrafast pump-probe system operating at multi-kHz repetition rate, *J. Opt.* **20**, 014005 (2018).
- [27] F. Vernuccio, A. Bresci, B. Talone, A. de la Cadena, C. Ceconello, S. Mantero, C. Sobacchi, R. Vanna, G. Cerullo, D. Polli, Fingerprint multiplex CARS at high speed based on supercontinuum generation in bulk media and deep learning spectral denoising, *Opt. Express* **30**, 30135–30148 (2022).

- [28] F. Vernuccio, R. Vanna, C. Ceconello, A. Bresci, F. Manetti, S. Sorrentino, S. Ghislanzoni, F. Lambertucci, O. Motiño, I. Martins, G. Kroemer, I. Bongarzone, G. Cerullo, D. Polli, Full-Spectrum CARS Microscopy of Cells and Tissues with Ultrashort White-Light Continuum Pulses, *J. Phys. Chem. B* **127**, 4733–4745 (2023).
- [29] A. De la Cadena, J. Park, K. F. Tehrani, C. A. Renteria, G. L. Monroy, S. A. Boppart, Simultaneous label-free autofluorescence multi-harmonic microscopy driven by the supercontinuum generated from a bulk nonlinear crystal, *Biomed. Opt. Express* **15**, 491–505 (2024).
- [30] E. Kueny, J. Meier, X. Levecq, N. Varkentina, F. X. Kärtner, A.-L. Calendron, Wavefront analysis of a white-light supercontinuum, *Opt. Express* **26**, 31299–31306 (2018).
- [31] A. Choudhuri, G. Chatterjee, J. Zheng, I. Hartl, A. Ruehl, R. J. Dwayne Miller, A spatio-spectral polarization analysis of 1 μm -pumped bulk supercontinuum in a cubic crystal (YAG), *Appl. Phys. B* **124**, 103 (2018).
- [32] A. Halder, V. Jukna, M. Koivurova, A. Dubietis, J. Turunen, Coherence of bulk-generated supercontinuum, *Photon. Res.* **7**, 1345–1353 (2019).
- [33] T. Hülsenbusch, L. Winkelmann, T. Eichner, T. Lang, G. Palmer, A. R. Maier, Reducing wavelength jitter in white-light seeded femtosecond optical parametric chirped-pulse amplifiers, *Opt. Express* **32**, 23416–23431 (2024).
- [34] B. Maingot, N. Forget, A. Jullien, Spatial-to-spectral phase coupling mechanisms in bulk continuum generation, *J. Phys. Photonics* **6**, 035002 (2024).
- [35] J. Kohl-Landgraf, J.-E. Nimsch, J. Wachtveitl, LiF, an underestimated supercontinuum source in femtosecond transient absorption spectroscopy, *Opt. Express* **21**, 17060–17065 (2013).
- [36] T. M. Kardaś, B. Ratajska-Gadomska, W. Gadomski, A. Lapini, R. Righini, The role of stimulated Raman scattering in supercontinuum generation in bulk diamond, *Opt. Express* **21**, 24201–24209 (2013).
- [37] W. Ryba-Romanowski, B. Macalik, A. Strzęp, R. Lisiecki, P. Solarz, R. M. Kowalski, Spectral transformation of infrared ultrashort pulses in laser crystals, *Opt. Mater.* **36**, 1745–1748 (2014).
- [38] B. Xiang, X. Ren, S. Ruan, L. Wang, P. Yan, H. Han, M. Wang, J. Yin, Visible to near-infrared supercontinuum generation in yttrium orthosilicate bulk crystal and ion implanted planar waveguide, *Sci. Rep.* **6**, 31612 (2016).
- [39] B. Macalik, R. M. Kowalski, W. Ryba-Romanowski, Spectral features of the Stokes part of supercontinuum generated by femtosecond light pulses in selected oxide crystals: A comparative study, *Opt. Mater.* **78**, 396–401 (2018).
- [40] Y. Yang, W. Bia, X. Li, M. Liao, W. Gao, Y. Ohishi, Y. Fang, Y. Li, Ultrabroad-band supercontinuum generation through filamentation in a lead fluoride crystal, *J. Opt. Soc. Am. B* **36**, A1–A7 (2019).
- [41] A. Šuminienė, V. Jukna, R. Šuminas, G. Tamošauskas, M. Vengris, A. Dubietis, LiSAF: An efficient and durable nonlinear material for supercontinuum generation in the ultraviolet, *Lith. J. Phys.* **60**, 217–224 (2020).

- [42] M. M. Neethish, V. V. Ravi Kanth Kumar, S. Nalam, S. Sree Harsha, P. Prem Kiran, Supercontinuum generation from zinc borate glasses: bandgap versus rare-earth doping, *Opt. Lett.* **46**, 1201–1204 (2021).
- [43] K. Madeikis, P.-M. Dansette, T. Bartulevicius, L. Veselis, R. Jutas, M. Eremchev, R. Danilevičius, V. Girdauskas, A. Michailovas, Investigation of materials for supercontinuum generation for subsequent nonlinear parametrical and Raman amplification at 1 MHz repetition rate, *Opt. Laser Technol.* **143**, 107373 (2021).
- [44] M. M. Neethish, J. N. Acharyya, P. P. Kiran, G. V. Prakash, A. Sharan, V. V. Ravi Kanth Kumar, Broad white light supercontinuum generation in Barium Zinc Borate glasses, *J. Lumin.* **251**, 119190 (2022).
- [45] S.-H. Nam, G. C. Nagar, D. Dempsey, O. Novák, B. Shim, K.-H. Hong, Multi-octave-spanning supercontinuum generation through high-energy laser filaments in YAG and ZnSe pumped by a 2.4 μm femtosecond Cr:ZnSe laser, *High Power Laser Sci. Eng.* **9**, e12 (2021).
- [46] R. Danilin, S. Vasilyev, D. Danilin, D. Martyshkin, V. Fedorov, J. Pigeon, S. Mirov, Supercontinuum generation in oxide and semiconductor materials (InP, Si, GaN, GaAs, PbMoO₄, YVO₄, ZGP, TiO₂, diamond) pumped by radiation of the Cr:ZnS fs-MOPA system, *J. Opt. Soc. Am. B* **42**, 1315–1322 (2025).
- [47] M. Vengris, N. Garejev, G. Tamošauskas, A. Čepėnas, L. Rimkus, A. Varanavičius, V. Jukna, A. Dubietis, Supercontinuum generation by co-filamentation of two color femtosecond laser pulses, *Sci. Rep.* **9**, 9011 (2019).
- [48] D. Li, L. Zhang, T. Xi, Z. Hao, High spectral energy density supercontinuum generation in fused silica by interfering two femtosecond laser beams, *J. Opt.* **21**, 065501 (2019).
- [49] Y. Li, J. Wu, H. Zhou, G. Deng, S. Zhou, Comparison of supercontinuum generation in bulk sapphire and femtosecond-laser-inscribed waveguides, *Opt. Laser Technol.* **158**, 108908 (2023).
- [50] M. Tripepi, A. Barrette, M. Ferdinandus, B. Eshel, K. L. Averett, E. A. Chowdhury, C. M. Liebig, Supercontinuum generation in single-crystal YAG fibers pumped around the zero-dispersion wavelength, *Appl. Opt.* **60**, G126–G131 (2021).
- [51] K. R. Keller, R. Rojas-Aedo, A. Vanderhaegen, M. Ludwig, D. Brida, High stability white light generation in water at multi-kilohertz repetition rates, *Opt. Express* **31**, 38400–38408 (2023).
- [52] A. B. Samuel, V. V. R. K. Kumar, S. S. Harsha, S. A. Nalam, P. P. Kiran, Structural and optical studies of sodium zinc borate glasses: effect of antimony in supercontinuum generation, *Appl. Phys. B* **130**, 66 (2024).
- [53] X. Wu, W. Zhou, Y. Koder, J. E. Garay, Nonlinear optical effects in polycrystalline transparent Al₂O₃ ceramics using femtosecond laser pulses-supercontinuum generation and laser damage, *Appl. Phys. Lett.* **124**, 101904 (2024).
- [54] N. Bagley, S. Wehbi, T. Mansuryan, R. Boulesteix, A. Maître, Y. Arosa Lobato, M. Ferraro, F. Mangini, Y. Sun, K. Krupa, B. Wetzels, V. Couderc, S. Wabnitz, A. Aceves, A. Tonello, Concatenation of Kerr solitary waves in ceramic YAG: application to coherent Raman imaging, *Opt. Lett.* **50**, 427–430 (2025).

- [55] R. Grigutis, G. Tamošauskas, V. Jukna, A. Risos, A. Dubietis, Supercontinuum generation and optical damage of sapphire and YAG at high repetition rates, *Opt. Lett.* **45**, 4507–4510 (2020).
- [56] Y. Li, G. Fu, R. Chen, G. Deng, H. Zhou, S. Zhou, Time evolution and degradation of a supercontinuum in sapphire, *Opt. Lett.* **50**, 2934–2937 (2025).
- [57] W. Liu, D. N. Schimpf, T. Eidam, J. Limpert, A. Tünnermann, F. X. Kärtner, G. Chang, Pre-chirp managed nonlinear amplification in fibers delivering 100 W, 60 fs pulses, *Opt. Lett.* **40**, 151–154 (2015).
- [58] J. Pimpè, J. Banys, S. Armalytė, J. Jakutis Neto, V. Jarutis, A. Dubietis, J. Ven gelis, Highly stable, 72 W average power, 76 MHz repetition rate femtosecond hybrid PCMA-FCPA Yb-fiber amplifier, *Opt. Laser Technol.* **190**, 113261 (2025).
- [59] R. W. Boyd, *Nonlinear Optics, Third ed.* (Academic Press, 2008).
- [60] J. H. Marburger, Self-focusing: Theory, *Prog. Quantum Electron* **4**, 35–110 (1975).
- [61] J. E. Rothenberg, Pulse splitting during self-focusing in normally dispersive median, *Phys. Rev. Lett.* **17**, 583–585 (1992).
- [62] A. Vogel, V. Venugopalan, Mechanisms of Pulsed Laser Ablation of Biological Tissues, *Chem. Rev.* **103**, 577–644 (2003).
- [63] V. Jukna, N. Garejev, G. Tamošauskas, A. Dubietis, Role of external focusing geometry in supercontinuum generation in bulk solid-state media, *J. Opt. Soc. Am. B* **36**, A54–A60 (2019).
- [64] J. E. Rothenberg, Space–time focusing: breakdown of the slowly varying envelope approximation in the self-focusing of femtosecond pulses, *Opt. Lett.* **17**, 1340–1342 (1992).
- [65] T. Nagy, P. Simon, L. Veisz, High-energy few-cycle pulses: Post-compression techniques, *Adv. Phys. X* **6**, 1845795 (2021).
- [66] A. Jarnac, G. Tamošauskas, D. Majus, A. Houard, A. Mysyrowicz, A. Couairon, A. Dubietis, Whole life cycle of femtosecond ultraviolet filaments in water, *Phys. Rev. A* **89**, 033809 (2014).
- [67] J. Galinis, G. Tamošauskas, I. Gražulevičiūtė, E. Keblytė, V. Jukna, A. Dubietis, Filamentation and supercontinuum generation in solid-state dielectric media with picosecond laser pulses, *Phys. Rev. A* **92**, 033857 (2015).
- [68] M. Mlejnek, E. M. Wright, J. V. Moloney, Dynamic spatial replenishment of femtosecond pulses propagating in air, *Opt. Lett.* **23**, 382–384 (1998).
- [69] T. B. Norris, Femtosecond pulse amplification at 250 kHz with a Ti:sapphire regenerative amplifier and application to continuum generation, *Opt. Lett.* **17**, 1009–1011 (1992).
- [70] M. Reed, M. Steiner-Shepard, D. Negus, Widely tunable femtosecond optical parametric amplifier at 250 kHz with a Ti:sapphire regenerative amplifier, *Opt. Lett.* **19**, 1855–1857 (1994).

- [71] B. J. Nagy, L. Gallais, L. Vámos, D. Oszetzky, P. Rácz, P. Dombi, Direct comparison of kilohertz- and megahertz-repetition-rate femtosecond damage threshold, *Opt. Lett.* **40**, 2525–2528 (2015).
- [72] P. Tzankov, I. Buchvarov, T. Fiebig, Broadband optical parametric amplification in the near UV–VIS, *Opt. Commun.* **203**, 107–113 (2002).
- [73] U. Megerle, I. Pugliesi, C. Schrieffer, E. Riedle, Sub-50 fs broadband absorption spectroscopy with tunable excitation: putting the analysis of ultrafast molecular dynamics on solid ground, *Appl. Phys. B* **96**, 215–231 (2009).
- [74] V. Marčiulionytė, V. Jukna, G. Tamošauskas, A. Dubietis, High repetition rate green-pumped supercontinuum generation in calcium fluoride, *Sci. Rep.* **11**, 15019 (2021).
- [75] H. Y. Tan, G. L. Ong, C. H. Nee, S. L. Yap, H. S. Poh, T. Y. Tou, B. L. Lan, S. F. Lee, S. S. Yap, Thermal-induced effects on ultrafast laser filamentation in ethanol, *Opt. Laser Technol.* **163**, 109350 (2023).
- [76] M. Kolesik, G. Katona, J. V. Moloney, E. M. Wright, Physical factors limiting the spectral extent and band gap dependence of supercontinuum generation, *Phys. Rev. Lett.* **91**, 043905 (2003).
- [77] R. Adair, L. L. Chase, S. A. Payne, Nonlinear refractive index of optical crystals, *Phys. Rev. B* **39**, 3337–3350 (1989).
- [78] A. Dubietis, A. Matijošius, Table-top optical parametric chirped pulse amplifiers: Past and present, *Opto-Electron. Adv.* **6**, 220046 (2023).
- [79] P. He, Y. Liu, K. Zhao, H. Teng, X. He, P. Huang, H. Huang, S. Zhong, Y. Jiang, S. Fang, X. Hou, Z. Wei, High-efficiency supercontinuum generation in solid thin plates at 0.1 TW level, *Opt. Lett.* **42**, 474–477 (2017).
- [80] G. Cirimi, R. E. Mainz, M. A. Silva-Toledo, F. Scheiba, H. Çankaya, M. Kubulek, G. M. Rossi, F. X. Kärtner, Optical Waveform Synthesis and Its Applications, *Laser Photonics Rev.* **17**, 2200588 (2023).
- [81] N. Krebs, I. Pugliesi, J. Hauer, E. Riedle, Two-dimensional Fourier transform spectroscopy in the ultraviolet with sub-20 fs pump pulses and 250–720 nm supercontinuum probe, *New J. Phys.* **15**, 085016 (2013).
- [82] E. Riedle, M. Bradler, M. Wenninger, C. F. Sailer, I. Pugliesi, Electronic transient spectroscopy from the deep UV to the NIR: unambiguous disentanglement of complex processes, *Faraday Discuss.* **163**, 139–158 (2013).
- [83] A. Dorrism, A. Umar, C. Grieco, Ultrabroadband Near-Infrared Transient Absorption Spectrometer with Simultaneous 900–2350 nm Detection, *Appl. Spectrosc.* **78**, 1043–1050 (2024).
- [84] G. Auböck, C. Consani, R. Monni, A. Cannizzo, F. van Mourik, M. Chergui, Femtosecond pump/supercontinuum-probe setup with 20 kHz repetition rate, *Rev. Sci. Instrum.* **83**, 093105 (2012).
- [85] R. Mao, L. Zhang, R.-Y. Zhu, Optical and scintillation properties of inorganic scintillators in high energy physics, *IEEE Trans. Nucl. Sci.* **55**, 2425–2431 (2008).

- [86] F. Träger (ed.), *Handbook of Lasers and Optics* (Springer, 2007).
- [87] R. DeSalvo, A. A. Said, D. J. Hagan, E. W. Van Stryland, M. Sheik-Bahae, Infrared to ultraviolet measurements of two-absorption and n_2 in wide bandgap solids, *IEEE J. Quantum. Electron.* **32**, 1324–1333 (1996).
- [88] D. W. Cooke, K. J. McClellan, B. L. Bennett, J. M. Roper, M. T. Whittaker, R. E. Muenchausen, R. C. Sze, Crystal growth and optical characterization of cerium-doped $\text{Lu}_{1.8}\text{Y}_{0.2}\text{SiO}_5$, *J. Appl. Phys.* **88**, 7360–7362 (2000).
- [89] M. J. Weber, *Handbook of optical materials* (CRC press, 2003).
- [90] B. Momgaudis, S. Guizard, A. Bilde, A. Melninkaitis, Nonlinear refractive index measurements using time-resolved digital holography, *Opt. Lett.* **43**, 304–307 (2018).
- [91] Y. Xu, W. Ching, Electronic structure of yttrium aluminum garnet ($\text{Y}_3\text{Al}_5\text{O}_{12}$), *Phys. Rev. B* **59**, 10530–10535 (1999).
- [92] P. Kabaciński, T. Kardaś, Y. Stepanenko, C. Radzewicz, Nonlinear refractive index measurement by SPM-induced phase regression, *Opt. Express* **27**, 11018–11028 (2019).
- [93] M. Kobayashi, M. Ishii, C. L. Melcher, Radiation damage of a cerium-doped lutetium oxyorthosilicate single crystal, *Nucl. Instr. and Meth. A* **335**, 509–512 (1993).
- [94] G. E. Jellison, E. D. Specht, L. A. Boatner, D. J. Singh, C. L. Melcher, Spectroscopic refractive indices of monoclinic single crystal and ceramic lutetium oxyorthosilicate from 200 to 850 nm, *J. Appl. Phys.* **112**, 063524 (2012).
- [95] H. Pang, G. Zhao, M. Jie, J. Xu, X. He, Study on the growth, etch morphology and spectra of Y_2SiO_5 crystal, *Mater. Lett.* **59**, 3539–3542 (2005).
- [96] B. Xiang, Y. Ma, H. Han, M. Wang, H. Zhang, S. Ruan, Ultraviolet to near-infrared supercontinuum generation in a yttrium orthosilicate channel waveguide formed by ion implantation, *Opt. Mater. Express* **7**, 1794–1803 (2017).
- [97] K. Ghimire, H. F. Haneef, R. W. Collins, N. J. Podraza, Optical properties of single-crystal $\text{Gd}_3\text{Ga}_5\text{O}_{12}$ from the infrared to ultraviolet, *Phys. Status Solidi B* **252**, 2191–2198 (2015).
- [98] D. L. Wood, K. Nassau, Optical properties of gadolinium gallium garnet, *Appl. Opt.* **29**, 3704–3707 (1990).
- [99] A. Bruner, D. Eger, M. B. Oron, P. Blau, M. Katz, S. Ruschin, Temperature-dependent Sellmeier equation for the refractive index of stoichiometric lithium tantalate, *Opt. Lett.* **28**, 194–196 (2003).
- [100] S. Ashihara, J. Nishina, T. Shimura, K. Kuroda, T. Sugita, K. Mizuuchi, K. Yamamoto, Nonlinear refraction of femtosecond pulses due to quadratic and cubic nonlinearities in periodically poled lithium tantalate, *Opt. Commun.* **222**, 421–427 (2003).
- [101] A. G. Selivanov, I. A. Denisov, N. V. Kuleshov, K. V. Yumashev, Nonlinear refractive properties of Yb^{3+} -doped $\text{KY}(\text{WO}_4)_2$ and YVO_4 laser crystals, *Appl. Phys. B* **83**, 61–65 (2006).

- [102] A. I. Vodchits, V. P. Kozich, V. A. Orlovich, P. A. Apanasevich, Z-Scan studies of KYW, KYbW, KGW, and $\text{Ba}(\text{NO}_3)_2$ crystals, *Opt. Commun.* **263**, 304–308 (2006).
- [103] H. F. Haneef, N. J. Podraza, Optical properties of single crystal $\text{Bi}_4\text{Ge}_3\text{O}_{12}$ from the infrared to ultraviolet, *J. Appl. Phys.* **116**, 163507 (2014).
- [104] P. A. Williams, A. H. Rose, K. S. Lee, D. C. Conrad, G. W. Day, P. D. Hale, Optical, thermo-optic, electro-optic, and photoelastic properties of bismuth germanate ($\text{Bi}_4\text{Ge}_3\text{O}_{12}$), *Appl. Opt.* **35**, 3562–3569 (1996).
- [105] D. Kudarauskas, G. Tamošauskas, M. Vengris, A. Dubietis, Filament-induced luminescence and supercontinuum generation in undoped, Yb-doped, and Nd-doped YAG crystals, *Appl. Phys. Lett.* **112**, 041103 (2018).
- [106] M. Itoh, T. Katagiri, Intrinsic luminescence from self-trapped excitons in $\text{Bi}_4\text{Ge}_3\text{O}_{12}$ and $\text{Bi}_{12}\text{GeO}_{20}$: decay kinetics and multiplication of electronic excitations, *J. Phys. Soc. Jpn.* **79**, 1–9 (2010).
- [107] A. Yamaji, T. Yanagida, Y. Yokota, Y. Fujimoto, M. Sugiyama, A. Yoshikawa, Comparative study on scintillation properties of LGG, YGG and GGG, in *IEEE Nuclear Science Symposium & Medical Imaging Conference, Knoxville, TN, USA* (2010), 179–181.
- [108] Y. Zorenko, A. Voloshinovskii, V. Savchyn, T. Voznyak, M. Nikl, K. Nejezchleb, V. Mikhailin, V. Kolobanov, D. Spassky, Exciton and antisite defect-related luminescence in $\text{Lu}_3\text{Al}_5\text{O}_{12}$ and $\text{Y}_3\text{Al}_5\text{O}_{12}$ garnets, *phys. stat. sol. (b)* **244**, 2180–2189 (2007).
- [109] W. Ryba-Romanowski, S. Gołąb, P. Solarz, G. Dominiak-Dzik, T. Łukasiewicz, Anti-Stokes emission in undoped YVO_4 , *Appl. Phys. Lett.* **80**, 1183–1185 (2002).
- [110] R. Mao, L. Zhang, R.-Y. Zhu, Emission spectra of LSO and LYSO crystals excited by UV light, X-Ray and γ -ray, *IEEE Trans. Nucl. Sci.* **55**, 1759–1766 (2008).
- [111] T. Wang, D. Ding, X. Chen, W. Hou, J. Shi, Exploring the energy transfer processes in $\text{Lu}_{2(1-x)}\text{Y}_{2x}\text{SiO}_5\text{:Ce}$ crystals, *J. Rare Earths* **36**, 685–689 (2018).
- [112] C. Pepin, P. Berard, A.-L. Perrot, C. Pepin, D. Houde, R. Lecomte, C. Melcher, H. Dautet, Properties of LYSO and recent LSO scintillators for phoswich PET detectors, *IEEE Trans. Nucl. Sci.* **51**, 789–795 (2004).
- [113] L. Qin, G. Ren, S. Lu, D. Ding, H. Li, Influence of RE doping on the scintillation properties of LSO crystals, *IEEE Trans. Nucl. Sci.* **55**, 1216–1220 (2008).
- [114] C. B. Schaffer, J. F. García, E. Mazur, Bulk heating of transparent materials using a high-repetition-rate femtosecond laser, *Appl. Phys. A* **76**, 351–354 (2003).
- [115] G. Genty, S. Coen, J. M. Dudley, Fiber supercontinuum sources, *J. Opt. Soc. Am. B* **24**, 1771–1785 (2007).
- [116] T. Sylvestre, E. Genier, A. N. Ghosh, P. Bowen, G. Genty, J. Troles, A. Mussot, A. C. Peacock, M. Klimczak, A. M. Heidt, J. C. Travers, O. Bang, J. M. Dudley, Recent advances in supercontinuum generation in specialty optical fibers, *J. Opt. Soc. Am. B* **38**, F90–F103 (2021).

- [117] Y. Ohishi, Supercontinuum generation and IR image transportation using soft glass optical fibers: a review, *Opt. Mater. Express* **12**, 3990–4046 (2022).
- [118] C. Langrock, M. M. Fejer, I. Hartl, M. E. Fermann, Generation of octave-spanning spectra inside reverse-proton-exchanged periodically poled lithium niobate waveguides, *Opt. Lett.* **32**, 2478–2480 (2007).
- [119] B. Kuyken, T. Ideguchi, S. Holzner, M. Yan, T. W. Hänsch, J. V. Campenhout, P. Verheyen, S. Coen, F. Leo, R. Baets, G. Roelkens, N. Picqué, An octave-spanning mid-infrared frequency comb generated in a silicon nanophotonic wire waveguide, *Nat. Commun.* **6**, 6310 (2015).
- [120] H. Guo, B. Zhou, M. Steinert, F. Setzpfandt, T. Pertsch, H.-P. Chung, Y.-H. Chen, M. Bache, Supercontinuum generation in quadratic nonlinear waveguides without quasi-phase matching, *Opt. Lett.* **40**, 629–632 (2015).
- [121] A. Sell, G. Krauss, R. Scheu, R. Huber, A. Leitenstorfer, 8-fs pulses from a compact Er: fiber system: quantitative modeling and experimental implementation, *Opt. Express* **17**, 1070–1077 (2009).
- [122] P. Dienstbier, F. Tani, T. Higuchi, J. Travers, P. S. J. Russell, P. Hommelhoff, Generation of 1.5 cycle pulses at 780 nm at oscillator repetition rates with stable carrier-envelope phase, *Opt. Express* **27**, 24105–24113 (2019).
- [123] M. Rutkauskas, A. Srivastava, D. T. Reid, Supercontinuum generation in orientation-patterned gallium phosphide, *Optica* **7**, 172–175 (2020).
- [124] S. Vasilyev, I. Moskalev, V. Smolski, J. Peppers, M. Mirov, V. Fedorov, D. Martyshkin, S. Mirov, V. Gapontsev, Octave-spanning Cr:ZnS femtosecond laser with intrinsic nonlinear interferometry, *Optica* **6**, 126–127 (2019).
- [125] S. Vasilyev, J. Gu, M. Mirov, Y. Barnakov, I. Moskalev, V. Smolski, J. Peppers, M. Kolesik, S. Mirov, V. Gapontsev, Low-threshold supercontinuum generation in polycrystalline media, *J. Opt. Soc. Am. B* **38**, 1625–1633 (2021).
- [126] A. Bartels, H. Kurz, Generation of a broadband continuum by a Ti:sapphire femtosecond oscillator with a 1 GHz repetition rate, *Opt. Lett.* **27**, 1839–1841 (2002).
- [127] T. M. Fortier, D. J. Jones, S. T. Cundiff, Phase stabilization of an octave-spanning Ti:sapphire laser, *Opt. Lett.* **28**, 2198–2200 (2003).
- [128] Z. Wang, C. Wang, Y. Han, S. Cao, Z. Zhang, L. Chai, Octave-spanning spectrum generation in Ti:sapphire oscillator, *Opt. Laser Technol.* **38**, 641–644 (2006).
- [129] M. Zukerstein, M. Kozák, F. Trojánek, P. Malý, Simple technique for the compression of nanojoule pulses from few-cycle laser oscillator to 1.7-cycle duration via nonlinear spectral broadening in diamond, *Opt. Lett.* **43**, 3654–3657 (2018).
- [130] J. Banyas, J. Vengelis, Efficient single-pass and double-pass pre-chirp managed Yb-doped rod-type fiber amplifiers using Gires-Tournois interferometric mirrors, *Optik* **249**, 168185 (2022).
- [131] A. Matijošius, J. Trull, P. D. Trapani, A. Dubietis, R. Piskarskas, A. Varanavičius, A. Piskarskas, Nonlinear space–time dynamics of ultrashort wave packets in water, *Opt. Lett.* **29**, 1123–1125 (2004).

- [132] M. C. Pujol, M. Rico, C. Zaldo, R. Solé, V. Nikolov, X. Solans, M. Aguiló, F. Díaz, Crystalline structure and optical spectroscopy of Er^{3+} -doped $\text{KGd}(\text{WO}_4)_2$ single crystals, *Appl. Phys. B* **68**, 187–197 (1999).
- [133] SNLO nonlinear optics code, available from A.V. Smith, AS Photonics, Albuquerque, NM, "<https://as-photonics.com>".
- [134] K. F. Lee, C. J. Hensley, P. G. Schunemann, M. E. Fermann, Midinfrared frequency comb by difference frequency of erbium and thulium fiber lasers in orientation-patterned gallium phosphide, *Opt. Express* **25**, 17411–17416 (2017).
- [135] Y. Liu, J. Zhao, Z. Wei, F. X. Kärtner, G. Chang, High-power, high-repetition-rate tunable longwave mid-IR sources based on DFG in the OPA regime, *Opt. Lett.* **48**, 1052–1055 (2023).
- [136] M. Pawłowska, F. Ozimek, P. Fita, C. Radzewicz, Collinear interferometer with variable delay for carrier-envelope offset frequency measurement, *Rev. Sci. Instrum.* **80**, 083101 (2009).
- [137] M. Rai, W. E. Deeg, B. Lu, K. Brandmier, A. M. Miller, D. H. Torchinsky, An oscillator-driven, time-resolved optical pump/NIR supercontinuum probe spectrometer, *Opt. Lett.* **48**, 570–573 (2023).
- [138] C. Rolland, P. Corkum, Compression of high-power optical pulses, *J. Opt. Soc. Am. B* **5**, 641–647 (1988).
- [139] E. Mével, O. Tcherbakoff, F. Salin, E. Constant, Extracavity compression technique for high-energy femtosecond pulses, *J. Opt. Soc. Am. B* **20**, 105–108 (2003).
- [140] J. Kim, Y. Kim, J. Yang, J. Yoon, J. Sung, S. Lee, C. Nam, Sub-10 fs pulse generation by post-compression for peak-power enhancement of a 100-TW Ti:Sapphire laser, *Opt. Express* **30**, 8734–8741 (2022).
- [141] S. Tóth, R. Nagymihály, I. Seres, L. Lehotai, J. Csontos, L. Tóth, P. Geetha, T. Somoskői, B. Kajla, D. Abt, V. Pajer, A. Farkas, A. Mohácsi, A. Börzsönyi, K. Osvay, Single thin-plate compression of multi-TW laser pulses to 3.9 fs, *Opt. Lett.* **48**, 57–60 (2023).
- [142] J. Schulte, T. Sartorius, J. Weitenberg, A. Vernaleken, P. Russbueldt, Nonlinear pulse compression in a multi-pass cell, *Opt. Lett.* **41**, 4511–4514 (2016).
- [143] J. Weitenberg, A. Vernaleken, J. Schulte, A. Ozawa, T. Sartorius, V. Pervak, H.-D. Hoffmann, T. Udem, P. Russbültdt, T. Hänsch, Multi-pass-cell-based nonlinear pulse compression to 115 fs at 7.5 μJ pulse energy and 300 W average power, *Opt. Express* **25**, 20502–20510 (2017).
- [144] C.-L. Tsai, F. Meyer, A. Omar, Y. Wang, A.-Y. Liang, C.-H. Lu, M. Hoffmann, S.-D. Yang, C. Saraceno, Efficient nonlinear compression of a mode-locked thin-disk oscillator to 27 fs at 98 W average power, *Opt. Lett.* **44**, 4115–4118 (2019).
- [145] A.-L. Viotti, C. Li, G. Arisholm, L. Winkelmann, I. Hartl, C. Heyl, M. Seidel, Few-cycle pulse generation by double-stage hybrid multi-pass multi-plate nonlinear pulse compression, *Opt. Lett.* **48**, 984–987 (2023).

- [146] J. Moses, F. Wise, Soliton compression in quadratic media: High-energy few-cycle pulses with a frequency-doubling crystal, *Opt. Lett.* **31**, 1881–1883 (2006).
- [147] M. Seidel, J. Brons, G. Arisholm, K. Fritsch, V. Pervak, O. Pronin, Efficient high-power ultrashort pulse compression in self-defocusing bulk media, *Sci. Rep.* **7**, 1410 (2017).
- [148] M. Seidel, G. Arisholm, J. Brons, V. Pervak, O. Pronin, All solid-state spectral broadening: an average and peak power scalable method for compression of ultrashort pulses, *Opt. Express* **24**, 9412–9428 (2016).
- [149] C.-H. Lu, W.-H. Wu, S.-H. Kuo, J.-Y. Guo, M.-C. Chen, S.-D. Yang, A. Kung, Greater than 50 times compression of 1030 nm Yb:KGW laser pulses to single-cycle duration, *Opt. Express* **27**, 15638–15648 (2019).
- [150] M. Seo, K. Tsendsuren, S. Mitra, M. Kling, D. Kim, High-contrast, intense single-cycle pulses from an all thin-solid-plate setup, *Opt. Lett.* **45**, 367–370 (2020).
- [151] M. Hanna, F. Guichard, N. Daher, Q. Bournet, X. Délen, P. Georges, Nonlinear optics in multipass cells, *Laser Photon. Rev.* **15**, 2100220 (2021).
- [152] A.-L. Viotti, M. Seidel, E. Escoto, S. Rajhans, W. Leemans, I. Hartl, C. Heyl, Multi-pass cells for post-compression of ultrashort laser pulses, *Optica* **9**, 197–216 (2022).
- [153] K. Fritsch, M. Poetzlberger, V. Pervak, J. Brons, O. Pronin, All-solid-state multipass spectral broadening to sub-20 fs, *Opt. Lett.* **43**, 4643–4646 (2018).
- [154] G. Barbiero, H. Wang, M. Graßl, S. Gröbmeyer, D. Kimbaras, M. Neuhaus, V. Pervak, T. Nubbemeyer, H. Fattahi, M. Kling, Efficient nonlinear compression of a thin-disk oscillator to 8.5 fs at 55 W average power, *Opt. Lett.* **46**, 5304–5307 (2021).
- [155] M. Seidel, P. Balla, C. Li, G. Arisholm, L. Winkelmann, I. Hartl, C. Heyl, Factor 30 pulse compression by hybrid multipass multiplate spectral broadening, *Ultrafast Sci.* **2022** (2022).
- [156] P. Carpeggiani, G. Fan, Z. Tao, G. Coccia, S. Zhang, Z. Fu, M. Chen, S. Liu, A. Kung, E. Kaksis, A. Pugzlys, A. Baltuška, Compact 6-mJ multi-plate pulse compression based on line focusing geometry, In Proceedings of the Laser Applications Conference, Vienna, Austria, 29 September–3 October 2019; Paper JTh3A.50.
- [157] O. Pronin, M. Seidel, F. Lücking, J. Brons, E. Fedulova, M. Trubetskov, V. Pervak, A. Apolonski, T. Udem, F. Krausz, High-power multi-megahertz source of waveform-stabilized few-cycle light, *Nat. Commun.* **6**, 6988 (2015).
- [158] T. Nakamura, V. Badarla, K. Hashimoto, P. Schunemann, T. Ideguchi, Simple approach to broadband mid-infrared pulse generation with a mode-locked Yb-doped fiber laser, *Opt. Lett.* **47**, 1790–1793 (2022).
- [159] D. Kang, T. Otsu, S. Tani, Y. Kobayashi, Sub-10-fs pulse generation from 10 nJ Yb-fiber laser with cascaded nonlinear pulse compression, *Opt. Express* **32**, 5214–5219 (2024).

- [160] A.-L. Viotti, B. Hessmo, S. Mikaelsson, C. Guo, C. Arnold, A. L'Huillier, B. Momgaudis, A. Melninkaitis, F. Laurell, V. Pasiskevicius, Soliton self-compression and spectral broadening of 1 μm femtosecond pulses in single-domain KTiOPO_4 , in *Proceedings of the Conference on Lasers and Electro-Optics Europe and European Quantum Electronics Conference*, Munich, Germany, 23–27 June 2019; Paper cf-4-5.
- [161] C. Krook, A.-L. Viotti, B. Hessmo, F. Laurell, V. Pasiskevicius, Self-compression in single-domain KTP at 1 micron in a normal dispersion regime, in *Proceedings of the Conference on Lasers and Electrooptics*, San Jose, CA, USA, 15–20 May 2022; Paper SM3O.2.
- [162] C. A. Klein, Room-temperature dispersion equations for cubic zinc sulfide, *Appl. Opt.* **25**, 1873–1875 (1986).
- [163] G. Janssonas, R. Budriūnas, M. Vengris, A. Varanavičius, Interferometric measurements of nonlinear refractive index in the infrared spectral range, *Opt. Express* **30**, 30507–30524 (2022).
- [164] F. Cornolti, M. Lucchesi, B. Zambon, Elliptic gaussian beam self-focusing in nonlinear media, *Opt. Commun.* **75**, 129–135 (1990).
- [165] G. Fibich, B. Ilan, Self-focusing of elliptic beams: An example of the failure of the aberrationless approximation, *J. Opt. Soc. Am. B* **17**, 1749–1758 (2000).
- [166] B. Zhu, Z. Fu, Y. Chen, S. Peng, C. Jin, G. Fan, S. Zhang, S. Wang, H. Ru, C. Tian, Y. Wang, H. Kapteyn, M. Murnane, Z. Tao, Spatially homogeneous few-cycle compression of Yb lasers via all-solid-state free-space soliton management, *Opt. Express* **30**, 2918–2932 (2022).
- [167] A. Žemaitis, P. Gecys, M. Barkauskas, G. Račiukaitis, M. Gedvilas, Highly-efficient laser ablation of copper by bursts of ultrashort tuneable (fs-ps) pulses, *Sci. Rep.* **9**, 12280 (2019).
- [168] S. Schwarz, S. Rung, C. Esen, R. Hellmann, Enhanced ablation efficiency using GHz bursts in micromachining fused silica, *Opt. Lett.* **46**, 282–285 (2021).
- [169] H. Sakurai, K. Konishi, Laser processing of silicon with GHz burst pumped third harmonics for precise microfabrication, *Opt. Express* **31**, 40748–40757 (2023).
- [170] E. Kažukauskas, S. Butkus, P. Tokarski, V. Jukna, M. Barkauskas, V. Sirutkaitis, Micromachining of transparent biocompatible polymers applied in medicine using bursts of femtosecond laser pulses, *Micromachines* **11**, 1093 (2020).
- [171] C. Kerse, H. Kalaycıoğlu, P. Elahi, B. Çetin, D. Kesim, O. Akçaalan, S. Yavaş, M. Aşık, B. Öktem, H. Hoogland, R. Holzwarth, F. Ilday, Ablation-cooled material removal with ultrafast bursts of pulses, *Nature* **537**, 84–88 (2016).
- [172] T. Baldacchini, S. Snider, R. Zadayan, Two-photon polymerization with variable repetition rate bursts of femtosecond laser pulses, *Opt. Express* **20**, 29890–29899 (2012).
- [173] L. Rimkus, I. Stasevičius, M. Barkauskas, L. Giniūnas, V. Barkauskas, S. Butkus, M. Vengris, Compact high-flux X-ray source based on irradiation of solid targets by gigahertz and megahertz bursts of femtosecond laser pulses, *Opt. Continuum* **1**, 1819–1836 (2022).

- [174] H. Ye, L. Pontagnier, C. Dixneuf, G. Santarelli, E. Cormier, Multi-GHz repetition rate, femtosecond deep ultraviolet source in burst mode derived from an electro-optic comb, *Opt. Express* **28**, 37209–37217 (2020).
- [175] S. Cai, M. Ruan, B. Wu, Y. Shen, P. Jiang, High conversion efficiency, mid-infrared pulses generated via burst-mode fiber laser pumped optical parametric oscillator, *IEEE Access* **8**, 64725–64729 (2020).
- [176] K. Nagashima, Y. Ochi, R. Itakura, Optical parametric oscillator pumped by a 100-kHz burst-mode Yb-doped fiber laser, *Opt. Lett.* **45**, 674–677 (2020).
- [177] M. Floess, T. Steinle, H. Giessen, Burst-mode femtosecond fiber-feedback optical parametric oscillator, *Opt. Lett.* **47**, 525–528 (2022).
- [178] M. Pergament, M. Kellert, K. Kruse, J. Wang, G. Palmer, L. Wissmann, U. Wegner, M. J. Lederer, High power burst-mode optical parametric amplifier with arbitrary pulse selection, *Opt. Express* **22**, 2202–22210 (2014).
- [179] M. Pergament, G. Palmer, M. Kellert, K. Kruse, J. Wang, L. Wissmann, U. Wegner, M. Emons, D. Kane, G. Priebe, S. Venkatesan, T. Jezynski, F. Pallas, M. J. Lederer, Versatile optical laser system for experiments at the European X-ray free-electron laser facility, *Opt. Express* **24**, 29349–29359 (2016).
- [180] R. Riedel, M. Schulz, M. J. Prandolini, A. Hage, H. Höppner, T. Gottschall, J. Limpert, M. Drescher, F. Tavella, Long-term stabilization of high power optical parametric chirped-pulse amplifiers, *Opt. Express* **21**, 28987–28999 (2013).
- [181] H. Höppner, A. Hage, T. Tanikawa, M. Schulz, R. Riedel, U. Teubner, M. J. Prandolini, B. Faatz, F. Tavella, An optical parametric chirped-pulse amplifier for seeding high repetition rate free-electron lasers, *New J. Phys.* **17**, 053020 (2015).
- [182] P. Balla, A. Bin Wahid, I. Sytceвич, C. Guo, A. Viotti, L. Silletti, A. Cartella, S. Alisauskas, H. Tavakol, U. Grosse-Wortmann, A. Schönberg, M. Seidel, A. Trabattoni, B. Manschwetus, T. Lang, F. Calegari, A. Couairon, A. L’Huillier, C. Arnold, I. Hartl, C. Heyl, Postcompression of picosecond pulses into the few-cycle regime, *Opt. Lett.* **45**, 2572–2575 (2020).
- [183] A. Viotti, S. Alisauskas, H. Tünnemann, E. Escoto, M. Seidel, K. Dudde, B. Manschwetus, I. Hartl, C. Heyl, Temporal pulse quality of a Yb:YAG burst-mode laser post-compressed in a multi-pass cell, *Opt. Lett.* **46**, 4686–4689 (2021).
- [184] P. Panagiotopoulos, M. Kolesik, S. Koch, E. Wright, S. Tochitsky, J. Moloney, Control of the filament dynamics of 10 μm pulses via designer pulse trains, *J. Opt. Soc. Am. B* **36**, G33–G39 (2019).
- [185] D. Reyes, H. Kerrigan, J. Peña, N. Bodnar, R. Bernath, M. Richardson, S. Fairchild, Temporal stitching in burst-mode filamentation, *J. Opt. Soc. Am. B* **36**, G52–G56 (2019).
- [186] D. Esser, S. Rezaei, J. Li, P. R. Herman, J. Gottmann, Time dynamics of burst-train filamentation assisted femtosecond laser machining in glasses, *Opt. Express* **19**, 25632–25642 (2011).

- [187] A. Couairon, E. Brambilla, T. Corti, D. Majus, O. Ramírez-Góngora, M. Kolesik, Practitioner's guide to laser pulse propagation models and simulation, *Eur. Phys. J. Spec. Top.* **199**, 5–76 (2011).
- [188] B. R. Namozov, M. E. Fominich, R. I. Zakharchenya, V. V. Myurk, Structure of the self-trapped exciton luminescence in α -Al₂O₃, *Phys. Solid State* **40**, 837–838 (1998).
- [189] M. Kirm, G. Zimmerer, E. Feldbach, A. Lushchik, C. Lushchik, F. Savikhin, Self-trapping and multiplication of electronic excitations in Al₂O₃ and Al₂O₃:Sc crystals, *Phys. Rev. B* **60**, 502–510 (1999).
- [190] A. Lushchik, E. Feldbach, M. Kirm, P. Liblik, C. Lushchik, I. Martinson, F. Savikhin, G. Zimmerer, Spectral-kinetic study of self-trapping and multiplication of electronic excitations in Al₂O₃ crystals, *J. Electron Spectrosc. Relat. Phenom.* **101–103**, 587–591 (1999).
- [191] A. Bildé, K. Redekas, A. Melninkaitis, M. Vengris, S. Guizard, Time resolved study of carrier relaxation dynamics in α -Al₂O₃, *J. Phys. Condens. Matter* **33**, 315402 (2021).
- [192] A. Mock, R. Korlacki, C. Briley, V. Darakchieva, B. Monemar, Y. Kumagai, K. Goto, M. Higashiwaki, M. Schubert, Band-to-band transitions, selection rules, effective mass, and excitonic contributions in monoclinic β -Ga₂O₃, *Phys. Rev. B* **96**, 245205 (2017).

Curriculum vitae

VAIDA MARČIULIONYTĖ

Vilnius, Lithuania

vaida.marciulionyte@ff.vu.lt

<https://www.webofscience.com/wos/author/record/NGR-9603-2025>

<https://www.researchgate.net/profile/Vaida-Marciulionyte>

Education Vilnius University

2021 – 2025 PhD in physics

2019 – 2021 Master's degree in Physics, Laser Physics and Optical Technologies
Magna cum laude

2015 – 2019 Bachelor's degree in Physics, Applied Physics
dr. Remis Gaška Scholarship awarded for the best bachelor's thesis of the year.

Research Vilnius University

Laser Research Center

2021 – present
Junior assistant

As PhD student, I

- Design experimental setups, perform experiments and analyze data.
- Supervised undergraduate students.
- Instruct undergraduate students in laser physics and laser technologies in teaching laboratories.

2022 – 2024 Junior researcher	Lithuanian Research Council funded research project (grant number S-MIP-22-40) <i>High repetition rate femtosecond filamentation-induced laser-matter interactions in transparent solids.</i>
2019 – 2020 Project specialist	European Regional Development Fund (project No. 1.2.2-LMT-K-718-02-0017) <i>Investigation of laser matter interaction with high frequency pulse burst which are generated by a controllable pulse burst generator.</i>

Institute of Photonics and Nanotechnology

2016 – 2019 Laboratory technician	As an undergraduate student, I joined Semiconductor Optoelectronics Group, where I characterized scintillating materials by photoluminescence spectroscopy with submicrometer spatial resolution enabled by confocal microscopy and photoluminescence spectroscopy.
--------------------------------------	---

Others

2023, 2024	Received two scholarships from the Lithuanian Research Council for PhD students in recognition of scientific contributions and other scientific activities.
2022, 2023	Supervised two undergraduate students during their professional practice.
2017 – 2021	Received three scholarships from the Lithuanian Research Council for bachelor's or master's students during the semester.
2018	Received a scholarship from the Lithuanian Research Council for bachelor's or master's students during the summer.
2017 – 2019	Jurgio Viščako scholarship

Notes

Notes

Notes

Vilnius University Press
Saulėtekio av. 9, Bld. III, LT-10222 Vilnius
e-mail: info@leidykla.vu.lt, www.leidykla.vu.lt
bookshop.vu.lt, journals.vu.lt
Print run copies 20